Study on High Temperature Superconducting Coil System for Magneto Plasma Sail Spacecraft

Yoh Nagasaki

Department of Electrical Engineering
Graduate School of Engineering
Kyoto University, Japan

September 2015

Abstract

Superconducting coils can revolutionize space propulsion systems. The performances, e.g., acceleration and thrust to power ratio, of a magneto plasma sail can be greatly improved with a superconducting coil by generating a larger magnetic field with less power consumption and weight. The magneto plasma sail is a space propulsion system with a higher fuel efficiency or specific impulse for future deep space explorations. The thrust of the magneto plasma sail is produced by the transfer of momentum from a solar wind plasma to a strong magnetic field generated by a High Temperature Superconducting (HTS) coil. The thrust of the sail is proportional to the magnetic moment of the coil (coil turn number × coil current × area enclosed by the coil). To obtain a large thrust to mass ratio, or acceleration, enough for space missions, our target is to increase the magnetic moment to mass ratio of the HTS coil system ten times larger than that obtained by a previous study. The HTS coil system is optimized to maximize its magnetic moment to mass ratio within the capacity of a launch vehicle.

To design an HTS coil for the magneto plasma sail, we first investigated a quantitative current transport performance and thermal behavior of an HTS coil, and the effect of the critical current inhomogeneity along the longitudinal direction of HTS tapes on the coil performances. We measured the current transport property and temperature rises during current applications of a scale-down model HTS coil using a Bi-2223/Ag tape in a conduction-cooled system, and analytically reproduced the results on the basis of the percolation depinning model and three-dimensional heat balance equation. a result, we estimated the critical currents of the HTS coil within 10% error for a wide range of the operational temperatures from 45 to 80 K, and temperature rises on the coil during current applications. These results showed that our analysis and conduction-cooled system were successfully realized. The analysis also suggested that the critical current inhomogeneity along the length of the HTS tape deteriorated the current transport performance and thermal stability of the HTS coil.

We also modeled screening currents I_s induced in HTS coils to investigate the effect of I_s on the coil magnetic field and a transport AC loss in an HTS coil for space applications of the HTS coil. compared analysis results with experimental data obtained from the Bi-2223/Ag scale-down model coil. The experimental residual magnetization due to I_s in the Bi-2223/Ag

coil can be effectively modeled assuming an equivalent loop length of approximate 9 mm for I_s in the coil. The values calculated from the method quantitatively agreed with the results for various experimental conditions as well as the hysteresis of the magnetization due to I_s. These results demonstrated the validity of our model for screening currents I_s, which considers the effects of flux creep and smaller I_s loops in the multi-filamentary Bi-2223/Ag tape. The transport AC loss in an HTS coil under AC ripple currents with DC offsets was also investigated to use a DC/DC converter for space applications of the HTS coil. Our analysis clarified that larger DC offsets greatly increase the effective AC loss even under a smaller AC current. In addition, we showed that the AC loss decreased the thermal stability of the conduction-cooled coil in case that HTS tapes in the coil are in the flux-flow state such as the load factor of 80%. These results suggested that, in order to apply the AC ripple current to HTS coils, the operational load factor must be properly selected.

To design an optimal HTS coil for use in space, we analyzed the characteristics of HTS coils using a Bi-2223/Ag tape or YBCO coated-conductors. The suitable configuration of the HTS coil was searched within a diameter of 4 m to obtain a larger magnetic moment and clarify the obtainable propulsive force from the magneto plasma sail. We analyzed the current transport properties, thermal behavior, and applied stresses of the HTS coils, and compared these characteristics for each coil configuration. As a result of a sensitivity study, we showed that a thin-walled racetrack coil or multi-pole coil with YBCO coated-conductors could achieve the larger magnetic moment with allowable stresses and high thermal stability for space missions.

The whole HTS coil system including the cooling system was also optimized to maximize the magnetic moment to mass ratio or acceleration, of the magneto plasma sail. The weight of the cooling system was considered for each coil configuration. We optimized the configuration of the coil using the genetic algorithm in the case of YBCO circular, multi-pole and racetrack coil at a variety of the operational temperatures from 10 K to 50 K on the condition of the perpendicular or parallel direction of the magnetic axis to the sun direction. For all kinds of the coils, the magnetic moment to mass ratio reaches the highest value at the operational temperature of around 20 K. On the other hand, in the case of using the HTS coil at less than 20 K, the magnetic moment to mass ratio rapidly decreases because a larger radiation cooling system is required. This study finally revealed that the racetrack coil system can maximize the magnetic moment to mass ratio of the system which is approximate three times larger than that of the minimum requirement for the magneto plasma sail.

The present study proved the possibility to increase the thrust to mass ratio of the sail system greatly, and leads to realizing a space propulsion system using an HTS coil.

Contents

List of Figures

List of Tables

Chapter 1

General Introduction

1.1 Introduction

Within the next decade or two, the National Aeronautics and Space Administration (NASA) plans to make human beings set foot on Mars where no man has ever gone before (Fig. 1.1 [1]). In order to broaden the sphere of our activity in space [2], space propulsion systems have been developed and advanced. At the present, chemical propulsion and electrical propulsion have been widely used as a propulsion system for spacecraft. The chemical propulsion is a propulsion system which obtains the propulsive force as a reaction force of a propellant injection utilizing thermal energy of fuel burning as represented by a launch vehicle “rocket”. Although the chemical propulsion can provide a large thrust in a short amount of time, it can be hardly used for a long term flight because the fuel efficiency is extremely lower and too much amount of fuel is required for long term missions. On the other hand, the electrical propulsion is a propulsion system which obtains the propulsive force as a reaction force of a propellant injection utilizing an electric energy. Although the obtainable force is smaller than that obtained by the chemical propulsion, it can be used for a longer term thanks to a higher fuel efficiency. Thus, the electrical propulsion is now mainly used for solar system explorations such as “HAYABUSA” mission by Japan Aerospace Exploration Agency (JAXA) which successfully achieved a sample return mission from an asteroid. However, the electrical propulsion requires a large amount of electric power to inject a propellant. Since the spacecraft generally uses solar panels to generate electricity, which create less electrical energy in deep space due to the distance from the sun, using the electrical propulsion for deep space explorations poses many difficulties. As just described, to explore and expand the sphere of human’s activity to deep space by using the existing chemical or electrical propulsion is difficult to realize.

Based on such backgrounds, a propulsion system which is so-called Sail propulsion such as

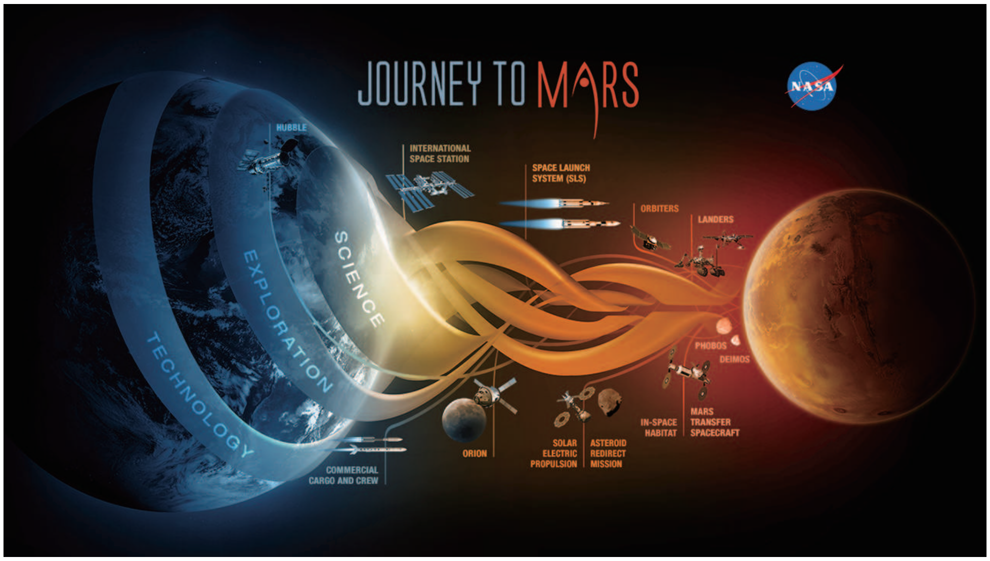

Figure 1.1: NASA's Journey to Mars [1].

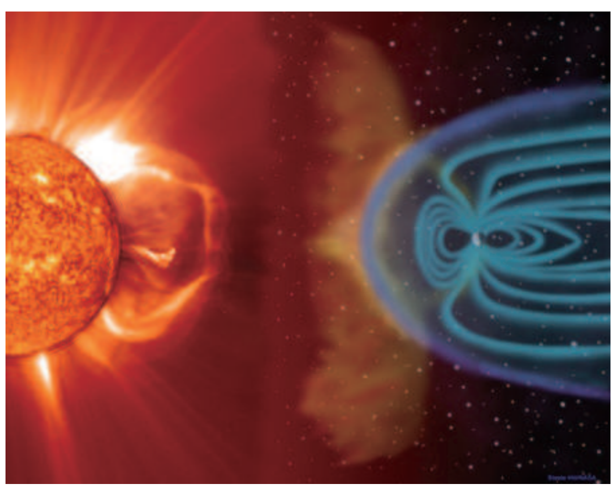

Figure 1.2: Environments of the interplanetary space [1].

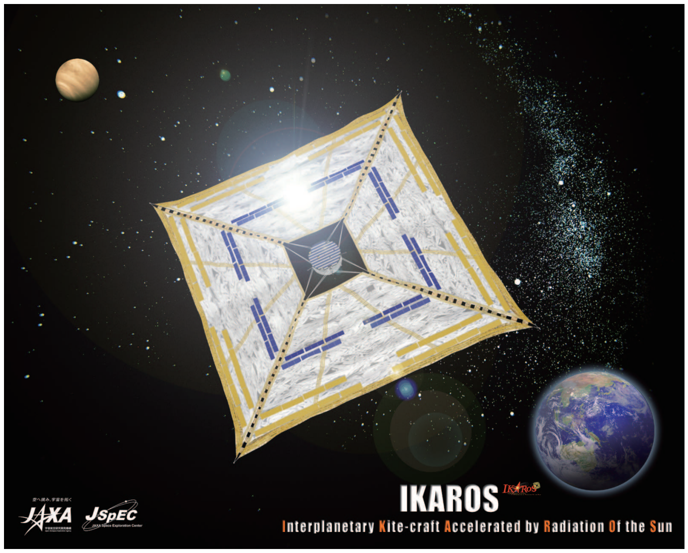

Figure 1.3: Solar sail demonstrator "IKAROS" [4].

Solar sail, Electric solar wind sail and Magnetic sail have been proposed. The sail propulsion can efficiently generates a propulsive force using the environment of an interplanetary space as shown in Fig. 1.2. The solar sail is a space propulsion system which obtains the propulsive force by reflecting a sunlight using a large thin mirror. The validity of the solar sail has been already demonstrated by "IKAROS" mission [3] by JAXA (Fig. 1.3 [4]). The electric solar wind sail [5] is a space propulsion system which uses charged long wires and generates the propulsive force by reflecting a solar wind, which is a plasma flow or charged particles from the sun, through the use of coulomb force (Fig. 1.4 [6]). The electric solar wind sail has been already demonstrated with a cubesat "ESTCube-1" [7]. Although the propulsive force of the sail propulsion is smaller than that of the chemical or electrical propulsion, the sail propulsion has the advantage of being able to generate the thrust without any propellant and realize an efficient long term flight to explore the deep space.

1.2 Magnetic Sail and Magneto Plasma Sail

Magnetic sail is one of the sail propulsion systems that has never been realized and demonstrated in space (Fig. 1.5). The concept of the magnetic sail was first invented by Zubrin and Andrews in 1991 [8]. The thrust of the magnetic sail is produced by the interaction between a solar wind, which is a plasma flow from the sun, and a strong magnetic field generated by an on-board superconducting coil in the spacecraft. A transfer of momentum from the solar wind to the magnetic field results in a propulsive force for the sail in the direction apart from the sun as shown in Fig. 1.6. The magnetic sail can theoretically achieve a higher fuel

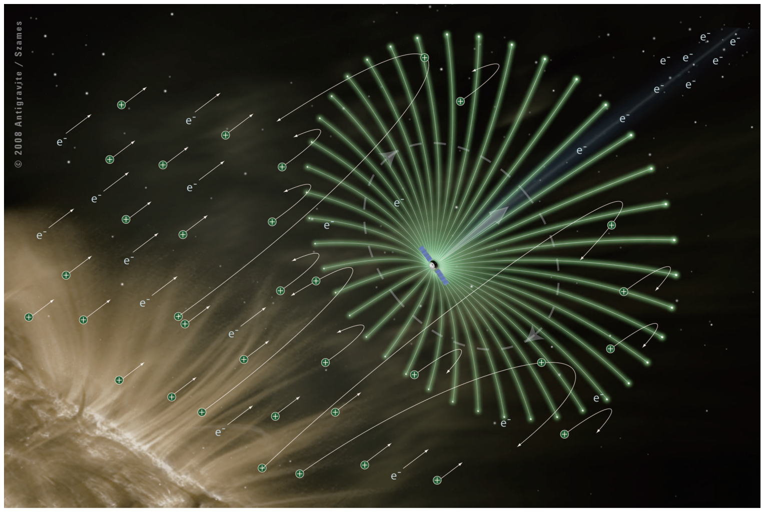

Figure 1.4: Concept of the electric solar wind sail [6].

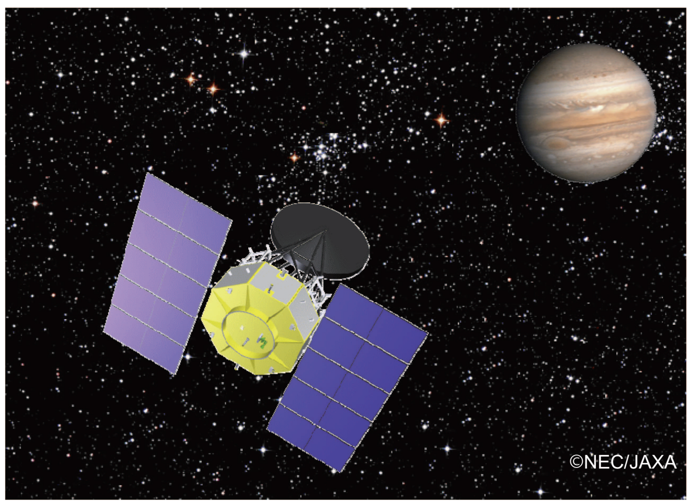

Figure 1.5: Illustration of the magnetic sail spacecraft.

efficiency and higher thrust to power ratio than the electric propulsion, as the magnetic sail directly converts the sun energy or momentum of the solar wind into the propulsive force without any fuel and also superconducting coil consumes less power. Such propellant less sail propulsion system has been expected to realize future deep space explorations [9]-[12]. Zubrin et al. reported that the magnetic sail will be able to generate a thrust of 19.8 N with a coil mass of 5000 kg and a magnetosphere with a diameter of 100 km [8]. However, a superconducting coil with a huge diameter of more than 10 km is required to generate such a huge magnetosphere. It has been impossible to launch or deploy a superconducting coil with such a huge diameter in order to generate a huge magnetosphere.

Winglee et al. proposed the concept of Magneto Plasma Sail (MPS) in 2000 which can

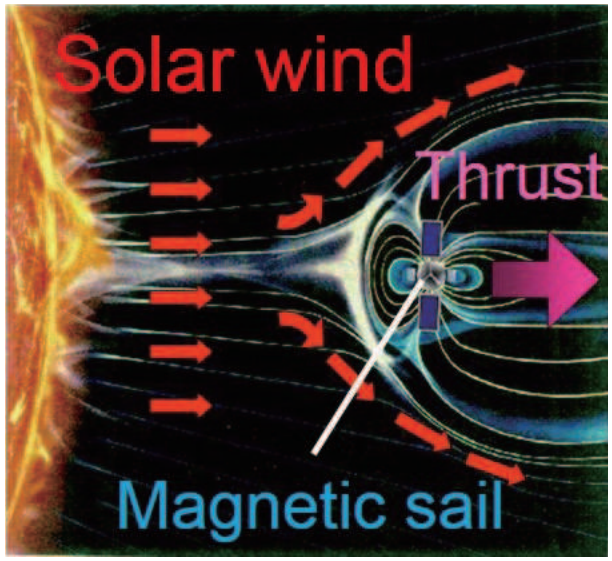

Figure 1.6: Thrust generation mechanism of the magnetic sail spacecraft.

produce a larger magnetosphere than that of the magnetic sail using a plasma injection from the spacecraft instead of using a huge size coil [13, 14]. Fig. 1.7 shows the illustration of the concept of the magneto plasma sail. The original magnetosphere produced by a superconducting coil with a diameter of a few meter is expanded to a larger magnetosphere by the plasma injection from the spacecraft through the effect of the frozen-in magnetic field. Although the magneto plasma sail requires some propellant to inflate the magnetosphere, there is no need for using a superconducting coil with a huge diameter such as 10 km to generate an enough thrust for space missions. Table 1.1 shows expected specifications of the magneto plasma sail as well as the ion engine, which is one of the electric propulsion used for "HAYABUSA" probe, and solar sail by way of comparison. As shown in Table 1.1, magneto plasma sail can theoretically realize a higher fuel efficiency (specific impulse $I_{\rm sp}$) and higher thrust to power ratio than those of the ion engine, and a higher thrust than that of the solar sail.

1.3 High Temperature Superconducting Coil

1.3.1 Electromagnetic Characteristics of Superconductors

The present section describes the electromagnetic characteristics of superconductors, which will be used for the magnetic sail or magneto plasma sail. Figure 1.8 describes the state diagram of superconductors. The state of the superconductors depends on the magnetic field, temperature and current applied to the superconductors. Superconductors turn into

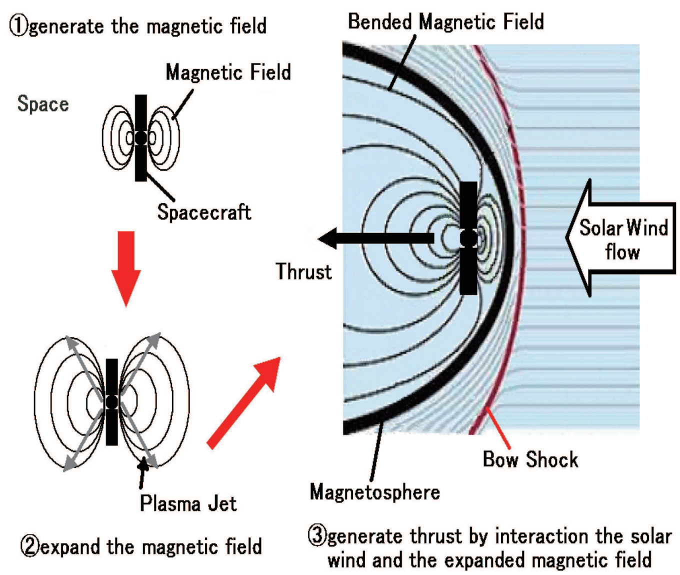

Figure 1.7: Concept of the magneto plasma sail.

Table 1.1: Specifications of magneto plasma sail, ion engine and solar sail [10]

	Ion engine	Solar sail	Magneto plasma sail
Spec	Propellant required (Xe etc.) I_{sp} = 3000-4500 s Thrust = several mN-200 mN Proportional to $1/\left(\text{Sun distance}\right)^2$ Efficiency=20-30 mN/kW Life = 8000-18000 h	No propellant required I_{sp} = infinity Thrust = 10 mN (14 m×14 m) Proportional to $1/\left(\text{Sun distance}\right)^2$ Life = to be verified	Propellant required (Xe etc.) I_{sp} = around 5000 s Thrust = 1 N at 4 kW Proportional to $1/\left(\text{Sun distance}\right)^{2/3}$ Efficiency=250 mN/kW Life = TBD
Operation	Extension mechanism not required Switch on/off possible	Extension mechanism required Thrust vector control by attitude control	TBD Switch on/off possible
Mission	Near-Earth asteroid rendezvous Mainbelt asteroid rendezvous Comet rendezvous	Fast outer planet flyby (Jupiter flyby in about 4-5 years with planetary gravity assists or with inner heliosphere visit)	Fast outer planet flyby (Jupiter flyby in about 2 years with direct Earth-Jupiter transfer)

Table 1.2: Critical temperature and magnetic field for superconductors.

	Materials	Critical Temperature (K)	Critical Magnetic Field (mT)
LTS	Pb	7.2	80
	Nb	9.3	40 - 300
	NbTi	9.5	199 - 11500
	MgB2	39	50 - 14000
HTS	YBCO	93	100 - 160000
	BSCCO	110	20 - 200000

a normal conducting state over the critical value of the current, magnetic field, and temperature. Superconductors can be separated into two groups based on their electromagnetic characteristics, which are called as type-I superconductor and type-II superconductor, respectively. A type-I superconductor is a material which cannot be penetrated at all by a weak magnetic field (below a critical magnetic field), a phenomenon known as the Meissner effect. Once the strength of the applied magnetic field rises above a critical magnetic field, however, superconductivity abruptly breaks down via a first order phase transition. The type-I superconductivity is typically exhibited by pure metals such as aluminum, lead, and titanium. On the other hand, a type-II superconductor is a material which has two stages of critical magnetic field. The magnetic field below a lower critical value, B_{c1}, cannot penetrate into type-II superconductors. Above a lower critical magnetic field strength B_{c1}, however, the magnetic field penetrates into type-II superconductors, although the superconductivity of the material is kept, which are called as mixed state. At a higher critical magnetic field B_{c2}, the superconductivity is destroyed. The type-II superconductors are usually made of metal alloys or complex oxide ceramics. Since the higher critical magnetic field B_{c2} for type-II superconductors is much larger than the critical field for type-I superconductors, type-II superconductors in a mixed state are mainly used for practical applications of the superconductivity. Table 1.2 shows the critical temperature and magnetic field for the variety of the superconductors. Only Pb in the table belongs to type-I superconductors and the other materials belong to type-II superconductors. All High Temperature Superconductors (HTS), which can be in a superconducting state at a higher temperature compared to Low Temperature Superconductors (LTS), such as above liquid nitrogen temperature 77 K, belong to type-II superconductors.

In a mixed state, magnetic fluxes, which are quantized, penetrates into a superconductor. Figure 1.9 shows the schematic diagram of the penetration of the flux. The equivalent Lorentz force acts on the quantized magnetic flux when the current is applied to the superconductor. If the quantized flux moves, the electric field is induced according to the Faraday's law, and

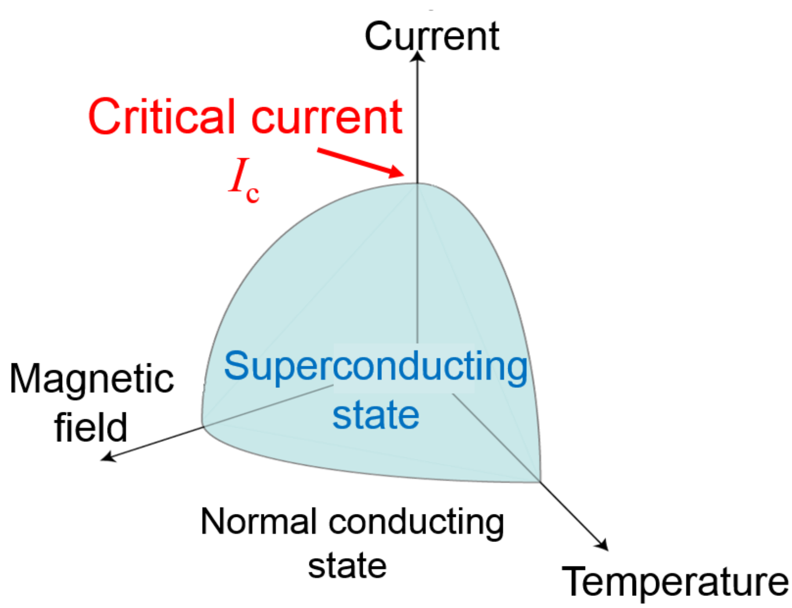

Figure 1.8: State diagram of superconductors.

a heat loss is caused by the inner product of the current density and electric field. However, type-II superconducting materials contain normal conducting precipitates and crystal interfaces that prevent the movement of the fluxes, and the loss is not generated with under a specific current. Such encumbered mechanism is called as the flux pinning, and acting force is called as the pinning force. In the case of a high temperature superconductor (HTS), the strength of the local pinning force shows a wide distribution due to the complex crystal geometry of the HTS, different from the case of Low Temperature Superconductors (LTS). Also, due to the relatively higher temperature operation than the LTS and layered crystal structure, the pinning force has a larger thermal disturbance. This fact suggests that, even if the same force acts on each quantized magnetic flux, some flux stochastically unlink from the pinning and move, but others do not. As a result, the electric field is gradually generated with the increasing applied current density for HTS materials as shown in Fig. 1.10, and such nonlinear characteristics depend on the strength and the angle of the applied field as well as operational temperature. Since HTS have such nonlinear current density and electric field ($J-E$) characteristics, the critical value for the applied current, critical current shown in Fig. 1.8, cannot be easily defined, and the nonlinear $J-E$ characteristics must be taken into account to understand the electromagnetic characteristics of HTS coils and design the optimal HTS coil for the magneto plasma sail.

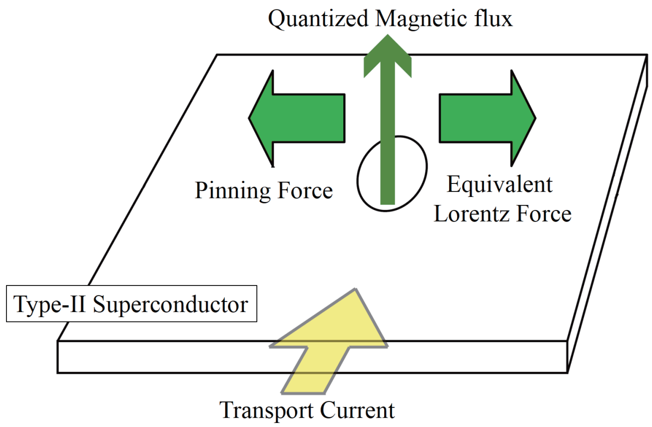

Figure 1.9: Schematic diagram of the penetration of the flux.

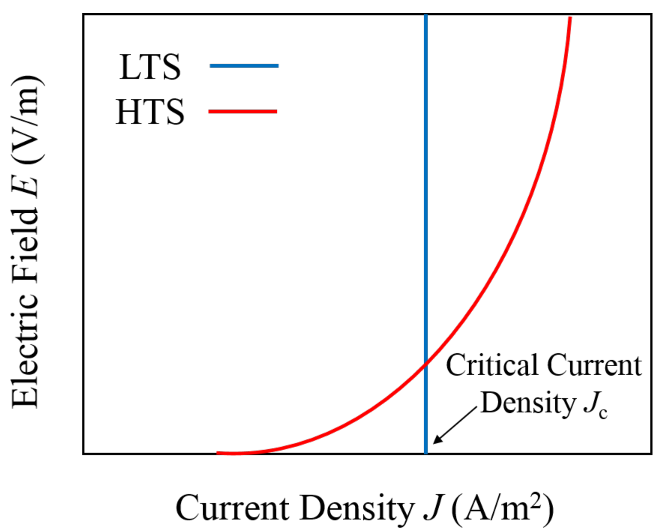

Figure 1.10: Comparison of the $J-E$ characteristics between LTS and HTS.

1.3.2 HTS Coil System for Magneto Plasma Sail

There is much interest in developing HTS coil systems for space applications such as for the magneto plasma sail and electric propulsion. Space propulsion systems with HTS coils can have larger thrust since HTS coils weigh less, use less power and produce larger magnetic fields than non-HTS coils [15]-[19]. The present section describes the outline of a magneto plasma sail system for the exploration to the planet Jupiter. Figure 1.11 shows the whole system configuration of the magneto plasma sail. The system is mainly composed of five elements, i.e., Solar paddles, Sun shields, Bus module, Radiation panels and HTS coil. The left side of the configuration in Fig. 1.11 corresponds to the solar paddles and the sun shields. The solar paddles produce the electric power from the sun light and the sun shields prevent the heat invasion from the sun to the other components. The spacecraft bus module contains the power supply system as well as the spacecraft control and telecommunication system. As a coil power supply, light-weight DC/DC converters will be used due to the strict limit of mass and power consumption for the spacecraft. Plasma sources are also installed to inject a plasma and expand the coil magnetic field. The right side of the configuration in Fig. 1.11 consists of the radiation panels and the HTS coil installed in the coil case. Due to the mass limitation, any refrigerants will not be used for the magneto plasma sail. The radiation panels and the coil case prevent the heat invasion which cannot be blocked only by the sun shield. In addition, a cryocooler can be installed in order to improve the stability of the coil temperature.

1.4 Overview of Previous Studies

There have been many previous studies about the magnetic sail and magneto plasma sail in terms of laboratory experiments, analytical and numerical considerations.

1.4.1 Laboratory Experiments

A research group at Institute of Space and Astronautical Science (ISAS)/JAXA reported that the thrust of 1 mN can be obtained based on a superconducting coil with the weight of 200 kg and, using the magnetic inflation, the thrust of 100 mN can be realized. Based on this estimation, experimental studies for the magneto plasma sail were conducted at ISAS/JAXA. These experiments verified that the artificial magnetosphere was formed with a normal conducting coil (scale-down magnetic sail) and plasma thruster (solar wind) [49] This scale-down magnetic sail demonstrator also confirmed by using the pendulum stand that the thrust was generated by the interaction between the magnetosphere and plasma flow

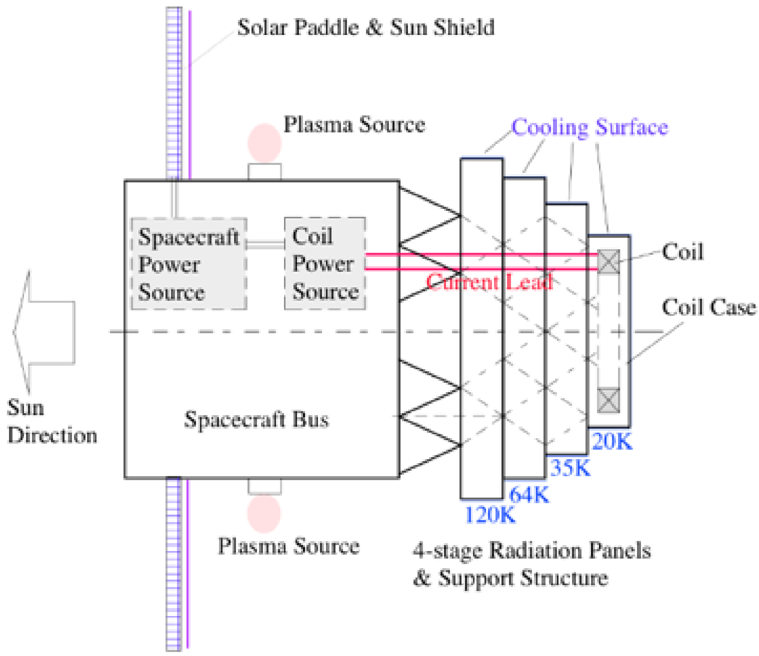

Figure 1.11: HTS coil system of the magneto plasma sail [20].

[22, 23]. The validity of the magnetic inflation was also verified and a larger magnetosphere was measured as shown in Fig. 1.12 [24]. However, the parameters which can be tested by the experiments were limited due to the size of the experimental system and, as a result, the actual phenomena of the full-scale magnetic sail cannot be reproduced in the experiment. A scale-down model of the HTS coil system for the magnetic sail has been also established in Kyoto University [25].

1.4.2 Numerical Simulations

The thrust characteristics of the magnetic sail and magneto plasma sail have been analytically investigated [26, 27]. Based on the analytical study, a superconducting coil with the weight of 3000 kg is required to obtain the thrust of 700 mN on the basis of the study of the magnetic flux conservation [27]. An orbital analysis using the magneto plasma sail was also conducted [28]-[30] and, to realize the magneto plasma sail, some new methods to increase the thrust of the magneto plasma sail were proposed [31]-[33], although these new methods have not been verified by numerical simulations as well as laboratory experiments. The numerical simulations must be first conducted to clarify the thrust characteristics of the magneto plasma sail.

Following Zubrin's [8] and Winglee's [13] study, there have been many studies to evaluate the thrust of the magnetic sail and magneto plasma sail. To evaluate the thrust of the sail

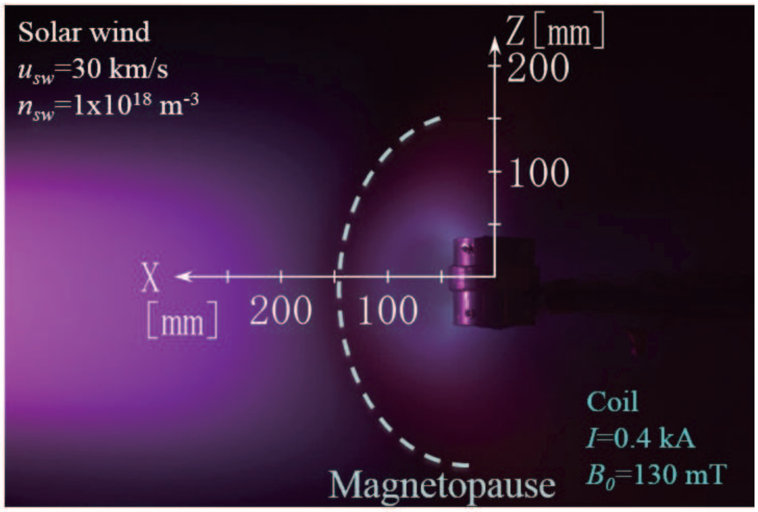

(a) Magnetic sail

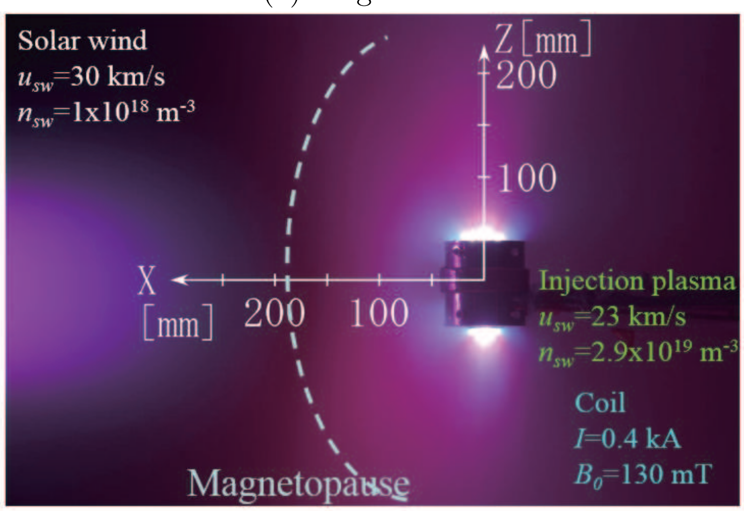

(b) Magneto plasma sail with plasma inflation

Figure 1.12: Experimental result of the photograph of the interaction between solar wind plasma and magnetic field [24].

accurately, the interaction of the plasma and magnetosphere has to be simulated with taking into account the relationship between the scale of the plasma and magnetosphere [34, 35], and the appropriate analytical model depends on the scale of the interaction. Winglee et al. simulated the thrust characteristics on the basis of the magnetohydrodynamic model and obtained a higher thrust from the magneto plasma sail, which can greatly shorten the mission time for deep space explorations [13]. However, later studies proved that the magnetohydrodynamic model is not suitable and full kinetic simulations are required to evaluate the thrust of the magneto plasma sail due to the scale of the interaction between the plasma (solar wind) and magnetosphere of the magneto plasma sail [35]-[38]. In the research group of ISAS/JAXA, the thrust as well as attitude stability of the magnetic sail and magneto plasma sail have been numerically investigated with assuming a variety of the scale of the plasma and magnetic field interaction [39]-[53]. These simulation results have showed that the magneto plasma sail is more promising with small scale magnetosphere, but the thrust improvement from the magnetic sail was limited to almost ten times smaller than expected in earlier investigations. It was also shown that the thrust of the magneto plasma sail with a small scale magnetosphere is proportional to the magnetic moment (coil turn number $\times$ coil current $\times$ area enclosed by the coil) of the on-board superconducting coil [53].

1.5 Objectives

The purpose of this study is to design the optimal high temperature superconducting (HTS) coil system for the magneto plasma sail to increase the thrust of the sail and compensate the shortfall of the thrust improvement by the plasma inflation. For the optimal design of an HTS coil for the magneto plasma sail, some problems must be solved; As mentioned in section 1.3, the nonlinear current transport characteristics, i.e., the electric field, E, versus current density, J, characteristics, of the HTS depend on the strength and angle of the applied magnetic field, operational temperature and, therefore, depend on the configuration and size of the coil and cooling condition. Although understanding the electromagnetic characteristics of the HTS is important to design HTS coils, an analysis model to accurately estimate such characteristics has not been developed. Also, space missions attach great importance to the reliability of on-board instruments in spacecraft. On the other hand, radiation and/or conduction cooling will be used to cool down the on-board HTS coil as the spacecraft has the limitation of the HTS cooling system due to the mass limit. A larger current must be applied to the HTS coil to generate a larger magnetic field for space missions, and the heat generation, $J \cdot E$, can easily transform the HTS coil into the normal conduction state in such cooling condition, and burn out the coil in space. A great care or precise estimation of the thermal stability of the conduction-cooled HTS coil are required to avoid damaging the coil in space, and, therefore, the thermal stability of the HTS coil is an important constraint for the optimal coil design for the magneto plasma sail. Moreover, due to the mass limitation of the spacecraft, a light-weight DC/DC converters, which contain AC ripples in output DC currents, will be used as the regulation of the power supply in the spacecraft as mentioned in section 1.3.2. The effect of using such a brute supply for HTS coils, such as AC loss, on the thermal stability of the HTS coils must be also investigated. Therefore, we first develop a thermo-electromagnetic field analysis method that can evaluate the nonlinear characteristics of the conduction-cooled HTS coil, i.e., current transport characteristics and thermal stability as well as AC loss of the HTS coils.

In order to obtain an adequate driving force and realize the magneto plasma sail, a magnetic moment, $\mu = NIS$, of the coil, to which the thrust of the magneto plasma sail is proportional, must be improved as large as possible. S denotes the area enclosed by the coil and NI (N: total turn number of the coil, I: operational transport current) is the magnetomotive force of the coil. One method to increase the magnetic moment is to enlarge S. Spacecraft size, however, is typically limited to be less than 4 m due to the installation size limit in the rocket for launch. Another way to increase μ is to enlarge NI. HTS coils have a big advantage for increasing I, and this is one of the major motivations to utilize the HTS coil for the magneto plasma sail. In order to obtain a large thrust to mass ratio, or acceleration, enough for space missions, our target is to increase the magnetic moment to mass ratio of the HTS coil system ten times larger than that obtained by a previous study. The HTS coil system including its cooling system with considering the thermal invasion due to the sun light is optimized to increase the magnetomotive force and maximize its magnetic moment to mass ratio and the thrust as well as acceleration of the magneto plasma sail within the capacity of a launch vehicle to realize the space propulsion system using an HTS coil.

1.6 Outline of This Thesis

This thesis consists of seven chapters as follows:

Background and objectives of this study as well as summary of previous studies for the magnetic sail and magneto plasma sail are described in chapter 1.

In chapter 2, heat transfer characteristics of Bi-2223/Ag tape and YBCO coated conductor are investigated to develop an analysis method to develop the thermal model for HTS coils. We measure temperature traces of the bundled conductors for the heater disturbance at conduction cooling conditions. Obtained results are modeled and analyzed using heat balance equations. On the basis of the modeled results, we obtain the thermal diffusivity, in the perpendicular direction to the tape surface, of the Bi-2223/Ag tape and YBCO coated conductor.

In chapter 3, an analysis method is developed to evaluate the current transport performance and thermal stabilities of HTS coils, in order to design a coil system for the magneto plasma sail. This method uses the percolation depinning model as the electric field and current density characteristics model for HTS. The analysis for thermal stability can estimate the current which causes an HTS coil to be quenched by solving the heat balance equation. Longitudinal inhomogeneities of the critical current of the HTS tape is considered for a precise analysis. We also fabricate a Bi-2223/Ag scale-down model coil and establish a conduction-cooled experimental system for the magneto plasma sail to verify the validity of the analysis method.

In chapter 4, the developed analysis method is extended to consider screening currents induced in HTS coils based on the percolation depinning and flux creep models. Screening currents induced in the Bi-2223/Ag scale-down model coil is modeled. The decay behavior as well as hysteresis curves of the magnetic field due to the screening currents under varying conditions is measured, and modeled assuming an equivalent loop length for the screening currents in the coil. Moreover, to use DC/DC converters as a regulation of the power supply for space missions, the effects of the transport AC losses under various ripple currents with DC offsets on the conduction-cooled coil performance is investigated by the developed analysis model.

In chapter 5, an HTS coil with a larger magnetic moment using YBCO coated conductors or Bi-2223/Ag tape are searched for a magneto plasma sail. For the coil design, we analyze the current transport properties, thermal stability, and applied stresses of the HTS coils, and compared these characteristics for each coil configuration, including the circular, racetrack, and multi-pole coil. The present study also investigate the required weight of the coil to obtain the minimum requirement of the magnetic moment at a variety of operational temperature, and clarify the suitable operational temperature of the HTS coil for the magneto plasma sail.

In chapter 6, the HTS coil system for the magneto plasma sail is optimized to maximize its magnetic moment to mass ratio using the genetic algorithm. The weight of the cooling system is calculated for each coil configuration. The configuration of the coil as well as the cooling structure is optimized using the genetic algorithm in the case of circular, multi-pole and racetrack coil at the operational temperature from 10 K to 50 K. Also, the direction of the magnetic axis of the coil is set to the perpendicular as well as parallel direction to the sun direction in this optimization.

In Chapter 7, we summarize this thesis and give conclusions obtained in the present study.

Chapter 2

Heat Transfer Characteristics of HTS tapes

2.1 Introduction

To reduce the weight of the spacecraft is important for space missions. A light-weight HTS coil system is required and radiation and/or conduction cooling which utilizes 3 K background temperature in space will be used for the magneto plasma sail. In such a cryogenics environment, Low Temperature Superconductors (LTS), which are more matured technology than High Temperature Superconductors (HTS), can be used. The temperature of the on-board coil, however, goes higher than the background temperature 3 K due to the heat invasion from the sun light which is not prevented by a sun-shield. Such heat invasion will evaporate the liquid helium which cools down an LTS coil to 4 K. Thus, to use the LTS coil in space for a long term, a huge helium tank is required such as like an ASTROMAG satellite [54]. For this reason, LTS coils are difficult to use for a space propulsion system for a deep space exploration, and an HTS coil will be used.

To design an HTS coil for use in space, cooling characteristics of the coil is an important constraint. Especially, for a YBCO coil which has a low level of heat transfer characteristics, a great care is required to avoid local heat generations and temperature rises (Hot spot). To realize an HTS coil system with a high reliability without any refrigerant, the heat transfer characteristics of HTS tapes in a longitudinal direction as well as perpendicular direction to the tape surface must be precisely investigated to design an reliable HTS coil used in space. Although those characteristics of a YBCO coil were measured under Adiabatic condition, the heat transfer characteristics taking into account cooling effects under the conduction cooling, and the difference of the thermal diffusivities of each HTS tape have not been investigated.

This chapter investigated thermal diffusivities of Bi-2223/Ag and YBCO tape conductors,

Table 2.1: Specifications of the tapes and bundles.

	Width (mm)	Tape thickness (mm)	Bundle thickness (mm)
Bi-2223/Ag	2.6	0.18	1.6
YBCO	3.0	0.11	1.2
Cu	2.9	0.11	1.2

which are candidates of the HTS to be used for the magneto plasma sail, as a preliminary consideration to design the HTS coil. Thermal input was applied to short length of bundled conductors with two kinds of setup of conduction cooling conditions. Experimental results were modeled solving heat balance equations, and heat transfer characteristics in a longitudinal direction and perpendicular direction to the tape surface were investigated.

2.2 Experiment

2.2.1 Experimental Setup

Figure 2.1 shows a conduction-cooled experimental system used in experiments. The inside of the chamber can be cooled down to around 10 K using a GM cryocooler.

To obtain the thermal diffusivities of HTS tapes, we fabricated bundled conductors using short length of five-conductors. In this experiment, thermal input was applied using a nichrome heater from the top surface of the bundle. By measuring the temperature change on top and bottom surface of the bundle, the heat transfer in the bundle was measured. The specifications of the tapes and bundles used in this experiment are shown in Table 2.1. To fabricate an HTS coil, the conductor is insulated using polyimide tapes, which worsen the heat transfer characteristics in the perpendicular direction to the tape surface. The bundles were also made with polyimide tapes assuming a coil geometry.

2.2.2 Measurement Procedure

The experiment was conducted with two kinds of setup in the conduction-cooled system as shown in Fig. 2.2. First, only 5 mm from the both-ends of the bottom of the bundle was cooled down to investigate the heat transfer in both of the longitudinal direction and perpendicular direction to the tape surface as shown in Fig. 2.2(a). We measured the heat transfer using three kinds of the tapes shown in Table 2.1 in the both-ends cooling system. In addition, with the YBCO coated-conductor, the heat transfer was measured under the condition that the whole area of the bottom of the bundle was uniformly cooled down as shown in Fig. 2.2(b). In the case of the uniform cooling system, the temperature gradient

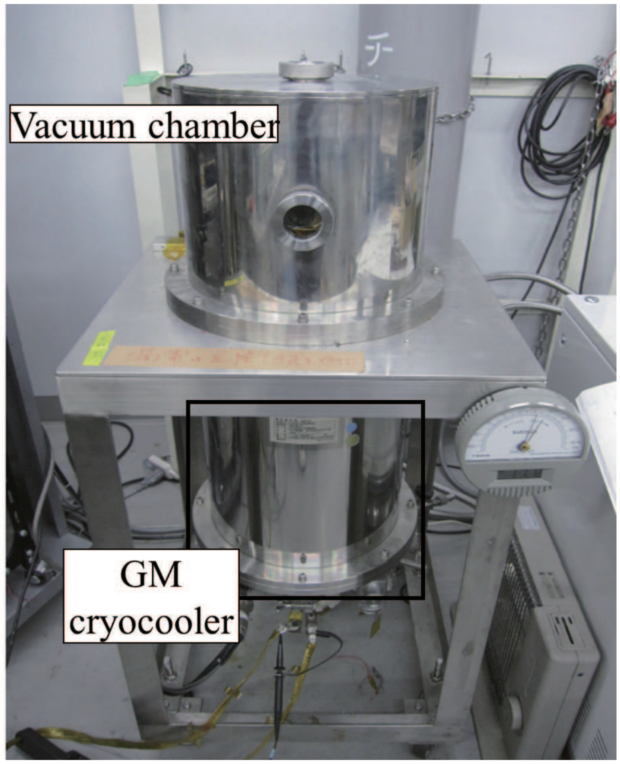

Figure 2.1: Conduction-cooled experimental system.

in the longitudinal direction was not generated. Thus, the heat transfer in the longitudinal direction can be ignored, and only in the perpendicular direction to the tape surface can be measured with this setup.

After the temperature of the bundle was stable, thermal input was applied for 60 s and then turned off. We measured temperature traces using Cernox® thermo-sensors at the center of the top and bottom surface of the bundled conductors as shown in Fig. 2.2, and investigated the heat transfer in the perpendicular direction to the tape surface of the bundle, i.e., from the heater to the bottom of the bundle. Thermal input of 290 mW was applied to the both-ends cooling system, and 10 W was applied to the uniform cooling system, using a nichrome heater, respectively. The initial temperature of the bundle in the experiment was set from 20 K to 77 K.

2.3 Analysis Model

2.3.1 Heat Transfer Analysis

Experimental results are modeled and analyzed using one-dimensional as well as two-dimensional heat balance equations, and the heat capacity, thermal conductivity and thermal diffusivity

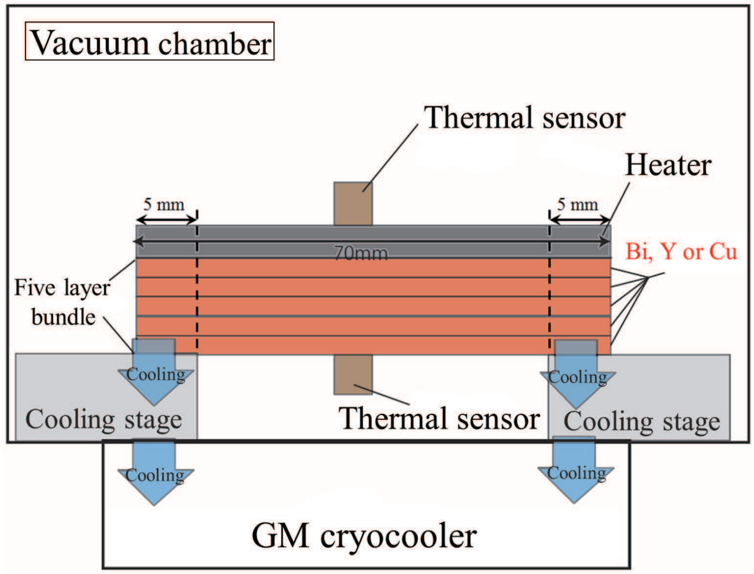

(a) Both-ends cooling system

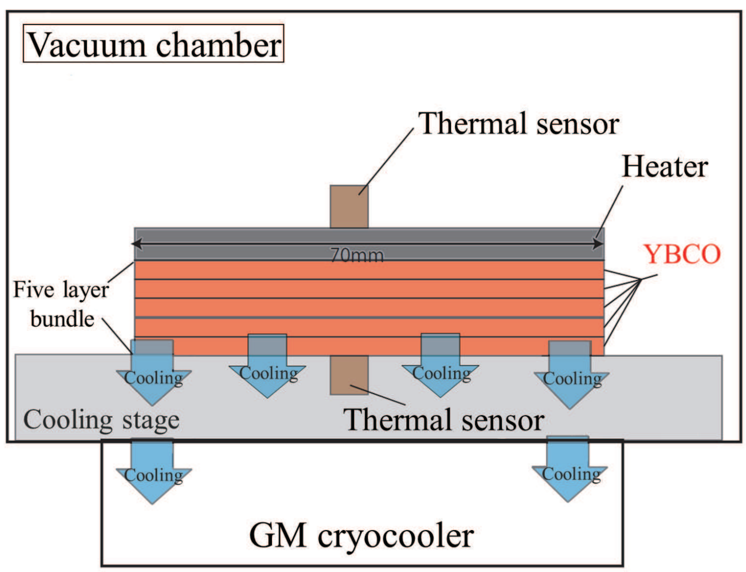

(b) Uniform cooling system

Figure 2.2: Schematic configuration of the experimental set-up to measure the thermal diffusivities of the HTS tapes.

of the HTS tapes were obtained. The heat balance equation for the bundle can be expressed as,

$$C\frac{\partial T}{\partial t} = \kappa \nabla^2 T + W \tag{2.3.1}$$

where T is temperature, κ is thermal conductivity, C and W are heat capacity and heat value for a unit volume. The thermal diffusivity can be obtained by κ/C. In addition, the amount of the heat transfer q between two different materials can be calculated as,

$$q = h\left(T_1 - T_2\right) \tag{2.3.2}$$

where T_1 is the temperature of material 1, T_2 is the temperature of material 2, respectively, and h is the heat transfer coefficient. The heat capacity C, thermal conductivity κ, heat transfer coefficient h were measured at 90, 64, 50, 37, 10 K. Those parameters at other temperatures were estimated with the linear interpolation. The heat balance equation was solved using Crank -Nicolson method, and the heat transfer during the heater disturbance was simulated.

2.3.2 Simulation Model

Figures 2.3(a) and 2.3(b) show the simulation model of the cross section of the bundles for the both-ends cooling system and uniform cooling system, respectively. As shown in these figures, the heater, each conductor and polyimide tapes make up a layer structure. In the both-ends cooling system, the dotted line at the center of the bundle in Fig. 2.3(a) shows symmetrical boundary. The heat transfer in the bundles was analyzed solving the two-dimensional heat balance equation in a half area of the bundle. On the other hand, in the uniform cooling system, the temperature gradient in the longitudinal direction was not generated and the heat was transferred only in the perpendicular direction to the tape surface. Thus, the heat transfer in the bundle was analyzed solving the one-dimensional heat balance equation for this setup as shown in Fig. 2.3(b). As the bundle was set in a vacuum, the Adiabatic condition was set as the boundary condition except the boundary with the cooling stages was set as the Dirichlet condition (see Fig. 2.2 and Fig. 2.3). For the Bi-2223/Ag tape, the inner structure was ignored, and treated as just one material. For the YBCO coated-conductor which has a layer structure, the inner structure which consists of Ag, YBCO, Buffer, and Hastelloy® layer was considered as shown in Fig. 2.3(c). However, the thickness of the YBCO and buffer layer was quite thin and ignored in this study, and it was assumed that the heat between

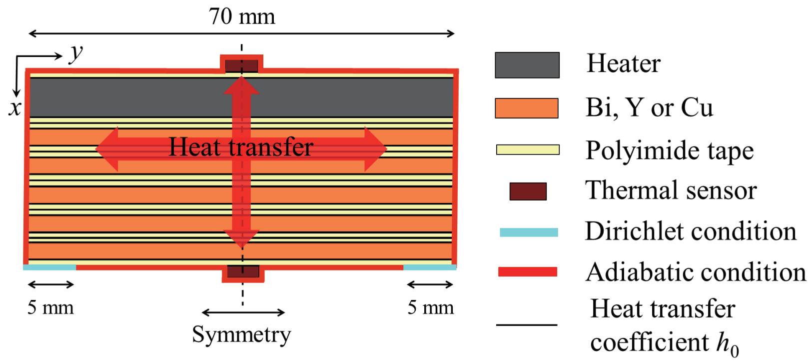

(a) Two-dimensional thermal analysis model of the both-ends cooling system

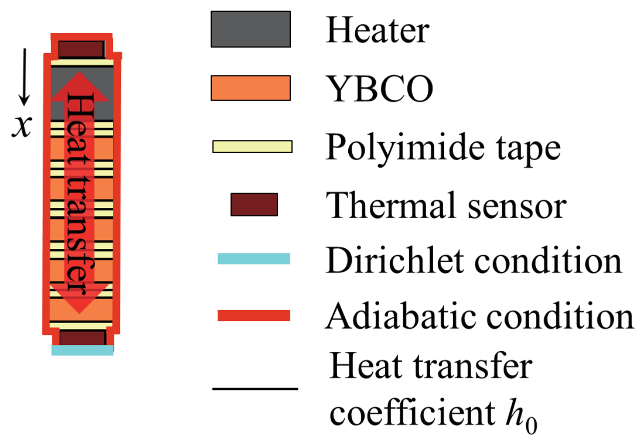

(b) One-dimensional thermal analysis model of the uniform cooling system

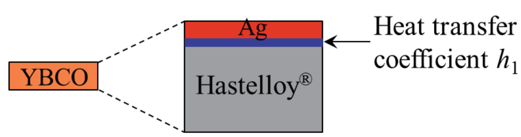

(c) Analysis model of the inside structure of the YBCO tape

Figure 2.3: Thermal analysis model of the cross-sectional surface of the bundles.

Ag and Hastelloy® layer was exchanged by the heat transfer coefficient h_1. We also assumed that the thermal diffusivity in a longitudinal direction and perpendicular direction to the tape surface is isotropic in the same material.

Although the thermal parameters, C, κ, of the nichrome heater, Cu, and Hastelloy® have been already known, the heat transfer coefficient, h_0, h_1, and the thermal parameters of the Bi-2223/Ag and polyimide tape have not known. By modeling the experimental results, these unknown parameters were obtained as fitting parameters. The analysis results were fitted with the experimental ones according to the following procedure.

1. The heat transfer coefficient, h_0, thermal conductivity, κ, and heat capacity, C, of the polyimide tape were first obtained by modeling the heat transfer in the Cu bundle whose thermal parameters have been already known.

2. The heat transfer coefficient, h_1, in the YBCO, and thermal conductivity, κ, and heat capacity, C, of the Bi-2223/Ag tape were obtained by modeling the heat transfer in the Bi-2223/Ag and YBCO bundle, using the thermal parameter obtained in the procedure 1.

The thermal diffusivities of the Bi-2223/Ag and YBCO tape conductor were estimated by the obtained thermal parameters.

2.4 Results and Discussion

2.4.1 Both-ends Cooling System

Figure 2.4 shows the experimental results of the temperature difference, ΔT, between the top and bottom surface of the bundle after the thermal input for the both-ends cooling system. Bi in the figures denotes the Bi-2223/Ag tape and Y denotes YBCO coated-conductor. The initial temperature was set at $T_0 = 20, 40, 60, 77$ K, respectively. The heat input was applied at $t = 0$ s and turned off at $t = 60$ s. As shown in the figures, the temperature difference, ΔT, becomes larger as the initial temperature, T_0, decreases. This is because the heat capacity of the heater and each conductor decreases with the temperature. As can also be seen in the figures, the temperature differences, ΔT, are the largest in the case of the YBCO bundle for all initial temperature condition. When the Bi-2223/Ag bundle is compared to the Cu bundle, ΔT makes little difference (at a lower temperature, ΔT is slightly higher in the Bi-2223/Ag bundle than in the Cu bundle). As larger ΔT shows lower thermal diffusivity, this result suggests that the thermal diffusivity of the YBCO coated-conductor is smallest and those of the Bi-2223/Ag and Cu tape is relatively the same value.

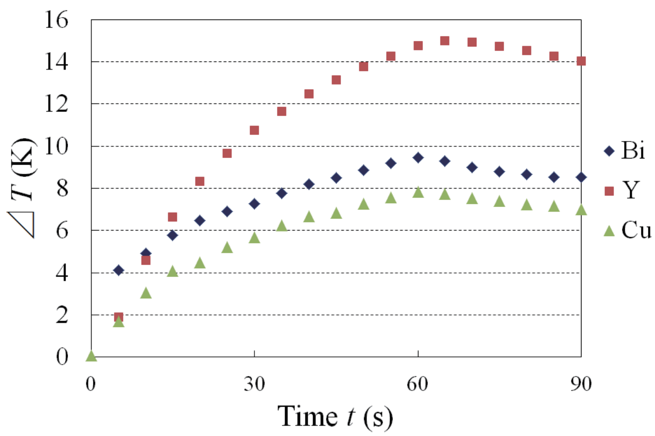

(a) $T_0 = 20$ K

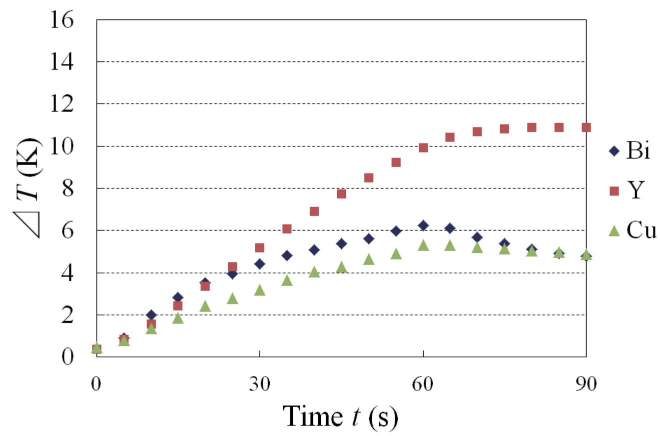

(b) $T_0 = 40$ K

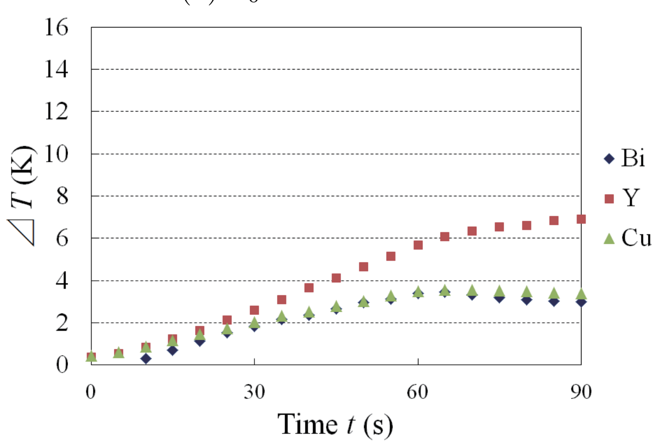

(c) $T_0 = 60$ K

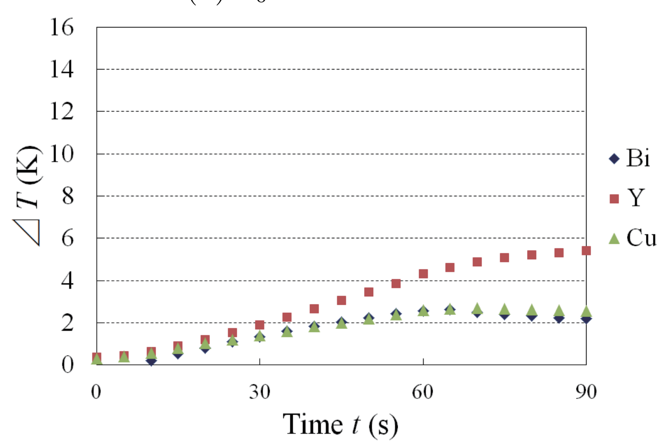

(d) $T_0 = 77$ K

Figure 2.4: Temperature difference between the upper and lower surface of the bundles during the heater disturbance (290 mW) for the both-ends cooling system (experimental results).

To quantify the thermal parameters of the HTS tapes, the experimental results were reproduced solving the two-dimensional heat balance equation. Figure 2.5 shows the fitting results of the temperature traces during the heater disturbance. The experimental results were shown as the symbols and analysis results as the lines. As shown in these figures, the analysis results successfully reproduced the experimental results. The thermal parameters estimated by the fitting results are shown in Fig. 2.6. The thermal conductivity and diffusivity of Ag and Hastelloy® are also described in Figs. 2.6(b) and (c) for references because Ag is used in the Bi-2223/Ag tape as a base material, and YBCO coated-conductor mainly consists of Ag and Hastelloy®. As shown in Fig. 2.6(c), although the value of the thermal diffusivity of the Bi-2223/Ag tape is similar to that of the base material, Ag, the thermal diffusivity, in the perpendicular direction to the tape surface, of the YBCO coated-conductor is five orders of magnitude lower than that of the Bi-2223/Ag, Ag, and Hastelloy®. Such a lower thermal diffusivity is caused by the thermal resistance between the layers in the YBCO coated-conductor which has a layer structure, i.e., the lower heat transfer coefficient, h_1, in the YBCO coated-conductor as shown in Fig. 2.6(a).

Figure 2.7 indicates the simulation result of the longitudinal temperature distribution of the bottom surface of the Bi-2223/Ag and YBCO bundle at t = 60 s (T_0 = 20 K). y = 0 mm denotes the measurement point of the temperature in the experiments (center of the bundle). To investigate the cooling effect of the conduction cooling, the analysis results with assuming the Adiabatic condition without any cooling path are also shown in Fig. 2.7 by way of comparison. As can be seen in Fig. 2.7, in the case of the Bi-2223/Ag bundle, the center of the bundle is cooled down thanks to the conduction cooling. On the other hand, in the case of the YBCO bundle, the area cooled down by the conduction cooling is confined to the immediate vicinity of the cooling stage (30 mm $< y <$ 35 mm) and the center of the bundle is not cooled down. One of the causes of this result is that, because the Hastelloy® covers the most part of the YBCO coated-conductor, the thermal diffusivity in the longitudinal direction is lower than that of the Bi-2223/Ag tape. In addition, the small thermal diffusivity of the YBCO in the perpendicular direction to the tape surface also affects the cooling characteristics as only the bottom part of the bundle is cooled down.

From these results, it was revealed that the thermal diffusivity of the YBCO coated-conductor is much lower than that of the Bi-2223/Ag tape not only in the longitudinal direction but also in the perpendicular direction to the tape surface. Due to such a low thermal diffusivity, when the YBCO coil is not uniformly cooled down, the heat generated in the coil cannot be easily drew away and the hot spot will be generated.

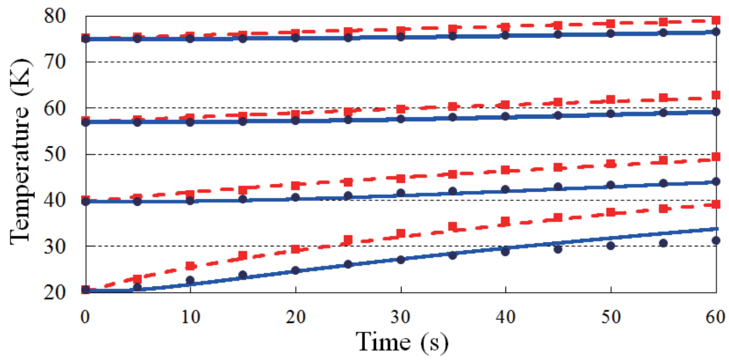

(a) Cu bundle

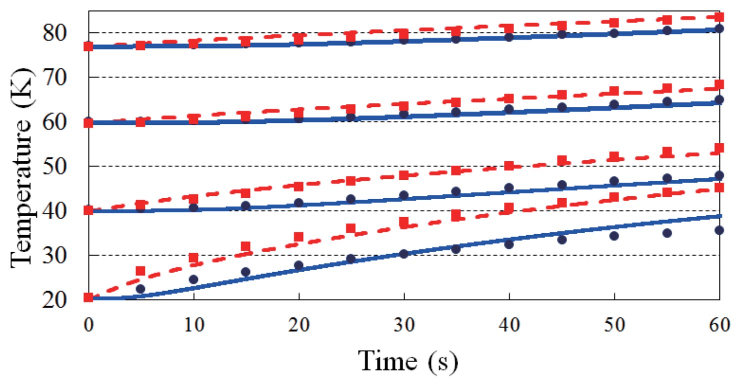

(b) Bi-system bundle

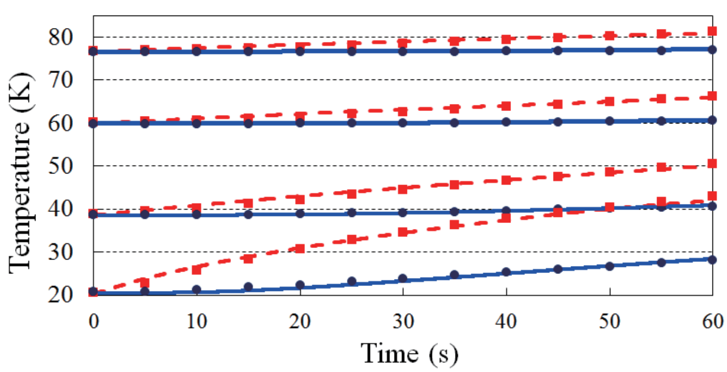

(c) Y-system bundle

Figure 2.5: Experimental results (symbols) and two-dimensional analysis results (curve) for the both-ends cooling system. Each figure indicates the results at T_0 = 20, 40, 60 and 77 K (square symbol and broken curve: upper surface; circle symbol and solid curve: lower surface).

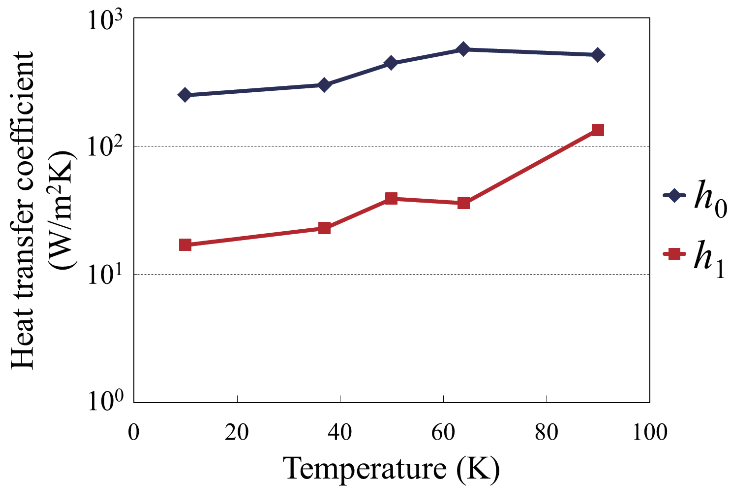

(a) Heat transfer coefficient h_0 and h_1

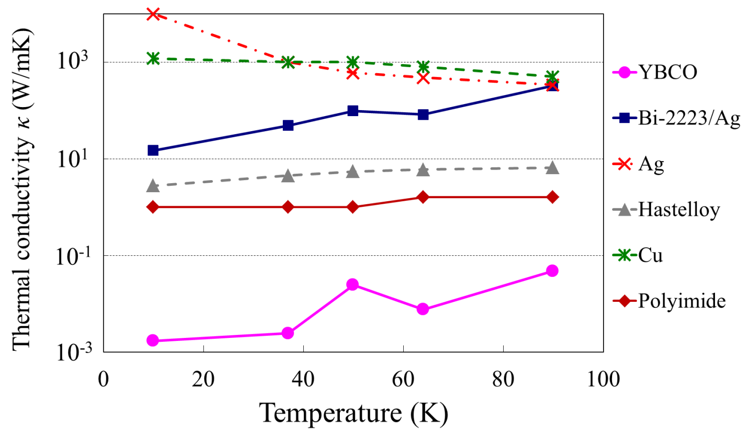

(b) Thermal conductivity κ

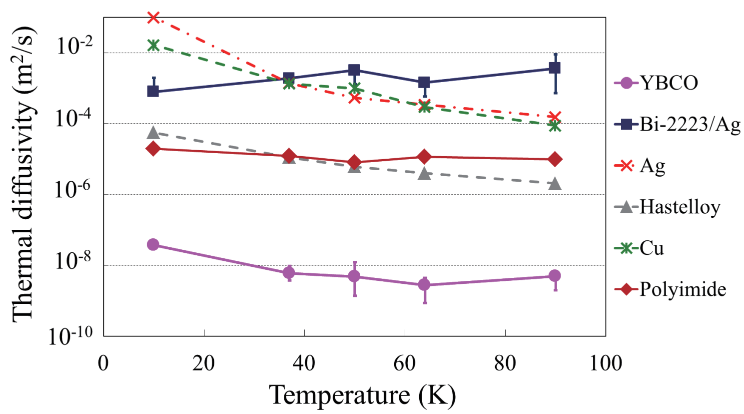

(c) Thermal diffusivity κ/C

Figure 2.6: Estimated (a) heat transfer coefficient, (b) thermal conductivity and (c) thermal diffusivity, in the perpendicular direction to the tape surface, from the fitting results for the both-ends cooling system.

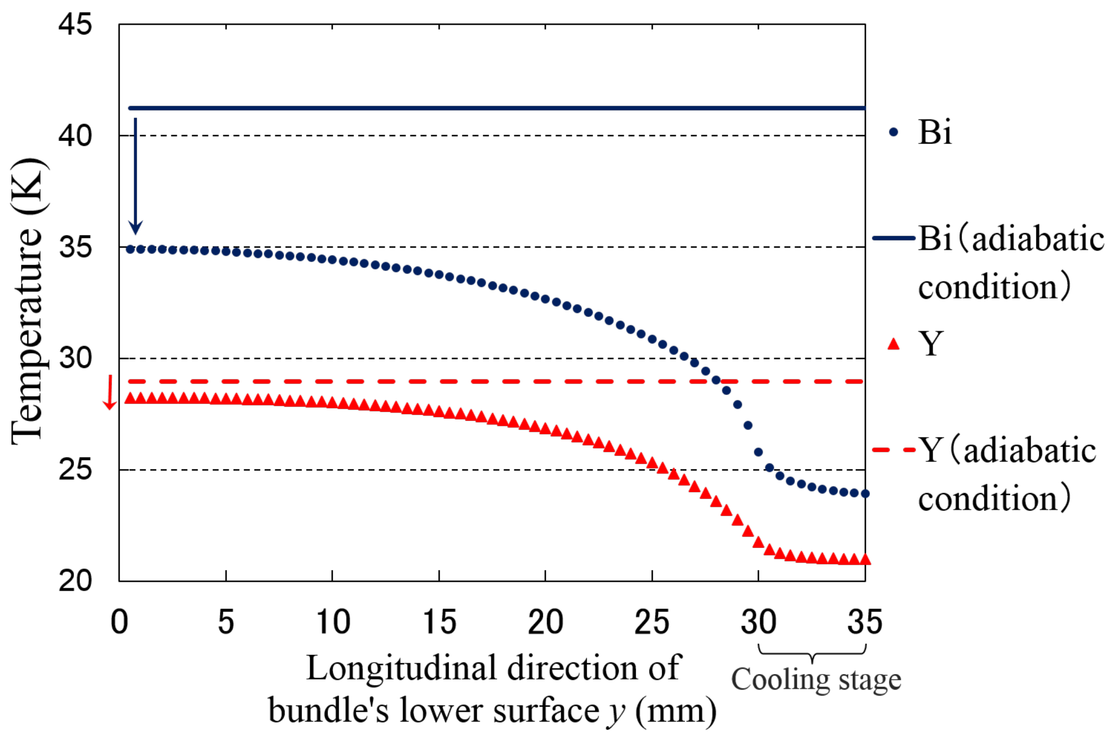

Figure 2.7: Temperature distribution of the lower surface of the bundles at $t = 60$ s (two-dimensional analysis results, initial temperature $T_0 = 20$ K). Temperature was measured at $y = 0$ mm in the experiments. The arrows in this figure indicate the cooling effect via the both-ends cooling system.

2.4.2 Uniform Cooling System

The shape of HTS coils is axial symmetry, and the heat generated in the coils must be transferred in the radial direction (the perpendicular direction to the tape surface) or axial direction of the coil. As obtained in the previous section, the fact that the thermal diffusivity, in the perpendicular direction to the tape surface, of the YBCO coated-conductor is approximate five orders of magnitude smaller than that of the Bi-2223/At tape is a serious constraint to design a coil using the YBCO coated-conductor. In this section, the thermal diffusivity in the perpendicular direction of the YBCO coated-conductor was precisely investigated by the experiment and analysis with the setup of the uniform cooling system (Fig. 2.2 (b) and Fig. 2.3(b)), which can be analyzed with only one-dimensional heat transfer.

Figure 2.8 shows the fitting results between the analysis (shown as line) and experimental results (shown as symbol). The heat transfer coefficient, h_1, and thermal diffusivity of the YBCO coated-conductor were again obtained by these fittings. The estimated thermal diffusivity of the YBCO coated-conductor in the perpendicular direction to the tape surface is shown in Fig. 2.9 as YBCO (uniform cooling system). The error bars in the figures show the estimation error of the thermal diffusivity due to the variation of the measurement data. As shown in Fig. 2.9, the difference between the thermal diffusivity, in the perpendicular direction to the tape surface, of the YBCO coated-conductor estimated with the uniform cooling condition and that estimated with the both-ends cooling condition is within the error bars except T_0 at around 10 K. These results obtained by the one-dimensional as well as two-dimensional analysis proved that the thermal diffusivity, in the perpendicular direction to the tape surface, of the YBCO coated-conductor is much lower than that of the Bi-2223/Ag tape. Such a terrible thermal diffusivity of the conductor is one of the reason why a hot spot is easily generated in the YBCO coil which causes the coil quench. In addition, since the thermal diffusivity of the YBCO coated-conductor is much lower in the longitudinal direction as well as the perpendicular direction, the YBCO coil must be uniformly cooled down to avoid a temperature gradient in the coil.

On the other hand, the thermal diffusivity of the Bi-2223/Ag tape, which is higher than that of the YBCO coated-conductor, is two orders of magnitudes lower than that of Ag at around 20 K, which will be the operational temperature of the on-board coil for the magneto plasma sail. Also, by giving attention to the experimental results shown in Fig. 2.4, the temperature differences, ΔT, in each conductor do not make an enough difference considering the difference of the thermal diffusivity between the YBCO coated-conductor and the other conductors. This result suggests that, for the bundled conductor or the coil, the thermal characteristic of the polyimide tape and heat transfer coefficient, h_0, are the dominant factor for the heat transfer. Figure 2.10 shows the thermal diffusivity of the whole bundles of the

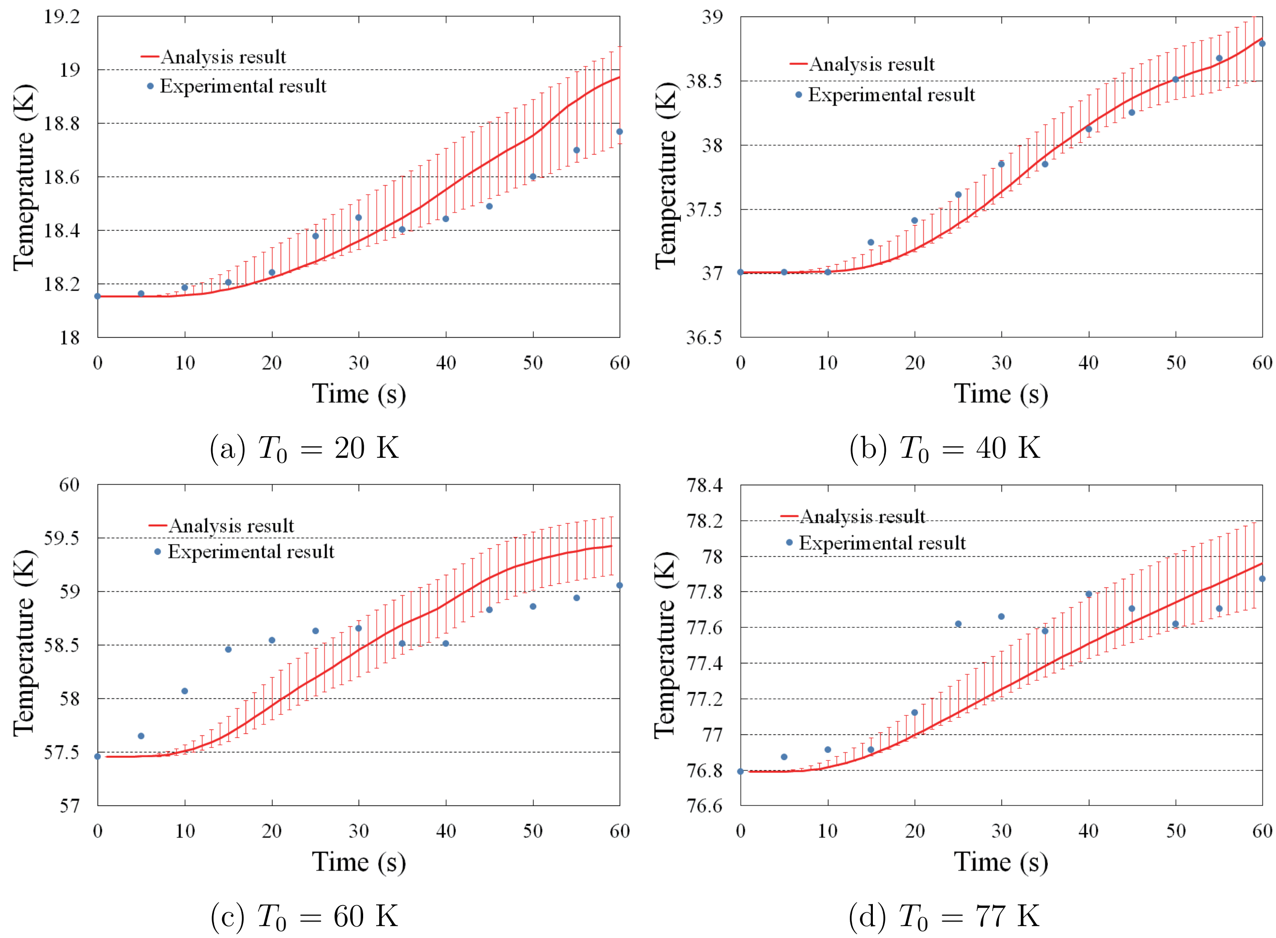

Figure 2.8: Temperature traces of the lower surface of the bundles during heater disturbance (10 W) for the uniform cooling system (experimental and one-dimensional analysis results).

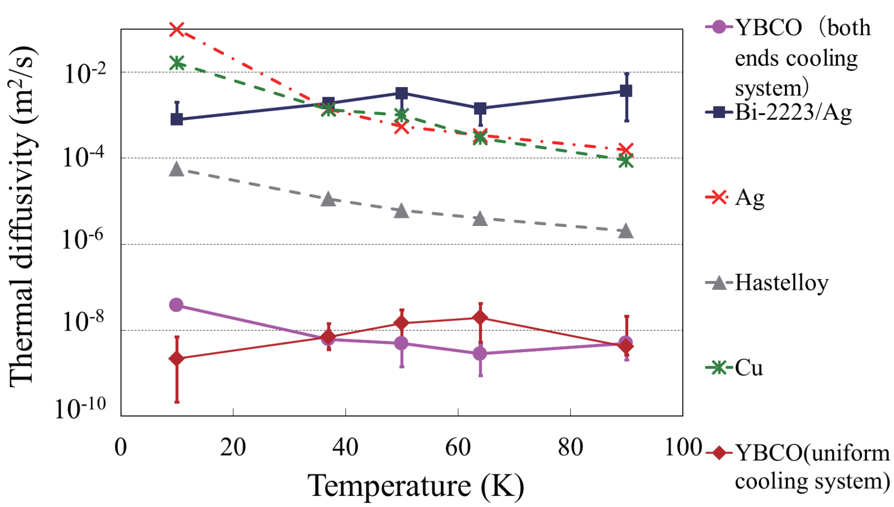

Figure 2.9: Estimated thermal diffusivity, in the perpendicular direction to the tape surface, from the fitting results for the uniform cooling system.

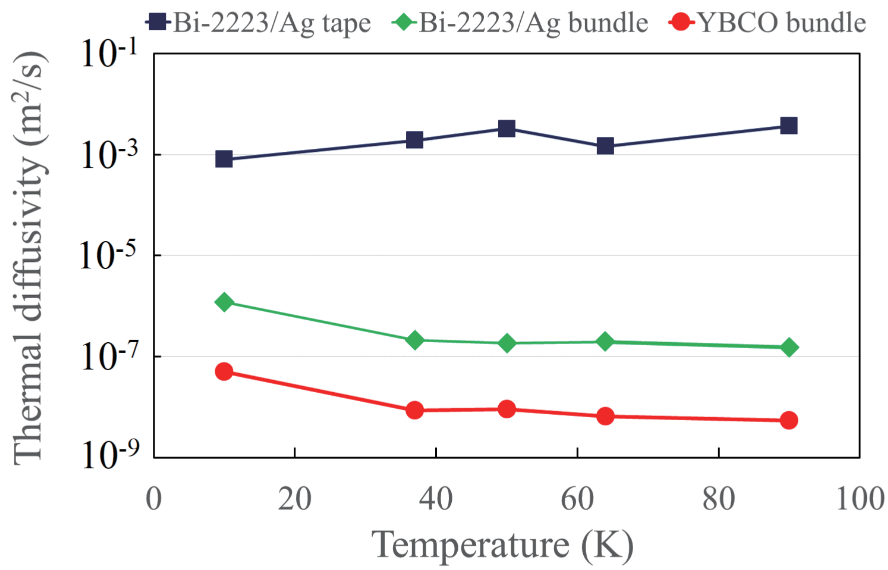

Figure 2.10: Estimated thermal diffusivity, in the perpendicular direction to the tape surface, of the bundled conductors.

Bi-2223/Ag and YBCO, obtained by the analysis assuming the bundle as just one material. The thermal diffusivity of the YBCO coated-conductor is obtained as the average value of two kinds of the experimental setups. As can be seen in the figure, as the bundle conductor, the thermal diffusivity of the Bi-2223/Ag becomes lower than that of the tape itself due to the thermal characteristics of the other materials and thermal resistivity between each material in the bundle, although it is still higher than that of the YBCO bundle. The thermal stability must be considered to avoid the coil quench even in the case of the Bi-2223/Ag coil. These thermal characteristics are important to design the HTS coils for use in space.

2.5 Summary

This chapter investigated the thermal diffusivities of the Bi-2223/Ag tape and YBCO coated-conductor to design a conduction-cooled HTS coil for the magneto plasma sail with precisely taking into account the thermal behavior of the coil. First, we measured temperature traces of the bundled conductors for the heater disturbance at conduction cooling conditions. Obtained results were modeled and analyzed using one-dimensional as well as two-dimensional heat balance equations. We showed that the analysis results successfully reproduced the experimental results for a wide temperature range from 20 to 77 K. On the basis of the modeling results, we clarified that the thermal diffusivity, in the perpendicular direction to the tape surface, of the YBCO coated-conductor is five orders of magnitude lower than that of the Bi-2223/Ag tape. In addition, even in the case of an HTS coil using the Bi-2223/Ag tape, the thermal stability of the coil is an important constraint and must be cared as the thermal characteristics of the coil or bundled conductors become worsen than that of the tape itself. Our results indicated that the consideration of a low thermal diffusivity of HTS tapes is important factor for the conduction-cooled magnet design.

Chapter 3

Current Transport and Thermal Analysis Model for HTS Coil

3.1 Introduction

This chapter investigated the quantitative current transport performance and thermal behavior of an HTS coil, and the effect of the critical current inhomogeneity along the longitudinal direction of HTS tapes on the coil performances. Space missions attach great importance to the reliability of the instruments installed in a spacecraft. For HTS coils, great care is needed to avoid coil quench in space. Although YBCO coated conductors (CCs) possess high performance with respect to the critical current in high magnetic fields, Bi-2223/Ag tapes are adopted in this study. This is because the cooling characteristics of the YBCO CCs are inferior to those of the Bi-2223/Ag tapes as obtained in the previous chapter and, in addition, long length tapes with high homogeneity in the local critical currents along the length of the conductors are difficult to be available in the case of the YBCO CCs.

Reducing the weight of the spacecraft is also important for the space missions. We aim to establish a light-weight HTS coil system based on radiation and/or conduction cooling which will utilize 3 K background temperature in space, similar to the JAXA "SPICA" satellite that is currently under development [56]. The temperature of the installed coil, however, becomes higher than the background temperature 3 K due to the heat invasion from the sun light under such cooling condition. The coil's operating temperature must be optimized with considering the balance among the performance of the conduction-cooled HTS coil, the cooling penalty and the weight of the cooling system. Hence, estimating the performance of the conduction-cooled HTS coil for arbitrary operational temperatures is essential for the optimal coil system and operating condition for the magneto plasma sail.

The electric field, E, versus current density, J, characteristics of HTS tapes vary in a complicated way as a function of temperature and magnetic field vector [57]-[61]. This nonlinear $E-J$ curves are the most important factors in order to understand the coil performance, such as thermal behavior. On the other hand, the magnetic field vector and temperature are distributed in the excited coil. This means that the $E-J$ curves are highly localized depending upon the position in the coil. In former reports, Higashikawa et al. made an analysis method to evaluate the current transport performance of HTS coils for HTS superconducting magnetic energy storage (SMES) with taking into account the distributed $E-J$ curves, based on the percolation depinning model [62]-[65]. However, although the validity of the percolation depinning model for HTS short tapes has been precisely verified, the validity for HTS coils has not been sufficiently confirmed by experiments. In addition, the longitudinal inhomogeneity of the critical current of HTS tapes has never been considered in the analysis, although this inhomogeneity is a serious constraint factor in the case of a large-sized coil with a long length tape such as for the magneto plasma sail.

In this study, in order to realize the optimal design of the HTS coil system for the magneto plasma sail, we developed an analysis method to predict the current transport performance as well as thermal behavior of a conduction-cooled HTS coil with taking into account the longitudinal distribution of critical currents of HTS tapes. We designed and fabricated a conduction-cooled experimental system and a Bi-2223/Ag double-pancake coil as a scale down model system for the magneto plasma sail. The current transport property and thermal behavior of the coil obtained by the analysis were compared with experimental results at various operational temperatures to validate the analysis method and the conduction-cooled system. We also investigated the effect of the critical current inhomogeneity in the longitudinal direction of the tape on the coil performances.

3.2 Experiment

3.2.1 Fabrication of Scale-down Model Coil

In order to validate an analysis method for characterizing an HTS coil and to design the optimal coil system for the magneto plasma sail, we fabricated and characterized a double-pancake coil using a Bi-2223/Ag tape with a length of 200 m as a scale-down model. The tape was 4.2 mm in width and 0.28 mm in thickness, and electrically insulated with polyimide tapes.

The specifications of the fabricated coil are shown in Table 3.1. Total turn number was 260, and the corresponding magnetomotive force was 10^5 A-turns for 400 A, which is one order of magnitude smaller than that of our targeted coil. Figure 3.1 shows the fabricated

Table 3.1: Specifications of the Bi-2223/Ag scale-down model coil for the magneto plasma sail spacecraft.

Items	Scale-down model coil
Shape	Double-pancake coil
Turn number	130 Layer × 2 stack
Inner diameter	0.200 m
Outer diameter	0.274 m
Tape width	4.2 mm
Tape thickness	0.28 mm
Tape length	200 m

Bi-2223/Ag double-pancake coil. The coil was wound on a G10 bobbin, and the copper electrodes were soldered at both ends of the windings. Whole surface of the coil was pasted with the epoxy resin. Six pieces of aluminum sheets for cooling were symmetrically attached at both top and bottom surfaces of the coil. We also fabricated a small double-pancake coil using a YBCO coated-conductor as shown in Fig. 3.2. The diameter and turn number of the YBCO coil are 0.1 m and 5 layer × 2 stack, respectively. We firstly measured the current transport performance of the coils cooled by liquid nitrogen as a preparatory experiment.

Figure 3.1: Bi-2223/Ag double-pancake coil (scale-down model for the magneto plasma sail).

3.2.2 Conduction-cooled System

Figure 3.3 shows the conduction-cooled experimental system. The lowest temperature in the vacuum chamber of the cryostat can reach 4 K by the GM cryocooler and, by using a cartridge

Figure 3.2: YBCO double-pancake coil.

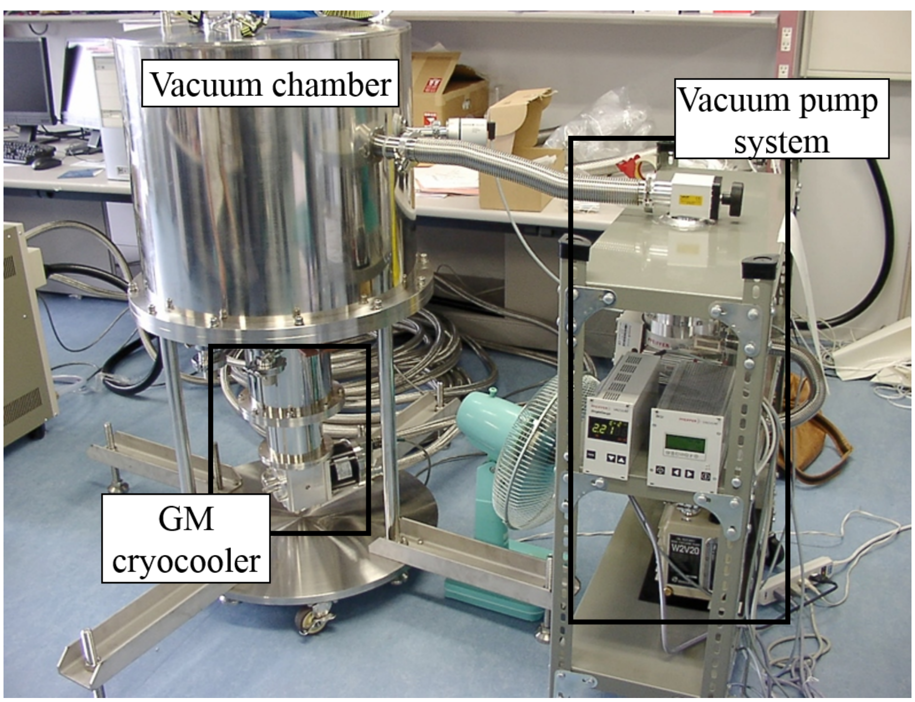

Figure 3.3: Conduction-cooled experimental system.

heater, the temperature can be controlled. The refrigerating capacity of the cryocooler was 1.5 W at 4 K.

3.2.3 Cooling Structure of Scale-down Model Coil

Figure 3.4 shows (a) a schematic diagram and (b) a photograph of the inside of the vacuum chamber. The fabricated scale-down model coil was installed at the second cold-stage of the GM refrigerator. Note that the coil was on the coil supports (GFRP) and only the aluminum cooling sheets were thermally connected to the cold-stage and cooling tower as shown in Fig. 3.4. From this structure, we restricted the cooling path of the coil for taking into account the cooling constraint of the spacecraft system. We also utilized the HTS current leads in order to reduce the thermal invasion from the outside of the chamber. The radiation shield walls were installed in between the voltage terminals and the coil. By introducing aforementioned cryogenic structures with trial-and-error basis, we finally developed the conduction-cooled HTS coil test system and cooled the coil down to 6 K uniformly. For the detailed examination of the temperature distribution in the coil, we installed Cernox® thermometers at various positions of both top and bottom surfaces of the coil (see Fig. 3.4(b)).

3.3 Analysis Model

3.3.1 Formulation of $E-J$ Characteristics

Kiss *et al.* proposed the percolation depinning model for the quantitative description of the current transport properties of HTS tapes [57, 59]. Based on this model, the electric field, E, versus current density, J, properties of the HTS tapes can be expressed as a function of temperature, T, magnetic field, B, and its applied direction, ϕ [66]-[69].

$$E = \begin{cases} \frac{\rho_{\mathrm{FF}} J_0(T,B_{\mathrm{eq}})}{m+1} \left(\frac{J-J_{\mathrm{cm}}(T,B_{\mathrm{eq}},\sigma)}{J_0(T,B_{\mathrm{eq}})}\right)^{m+1} & \text{for } B_{\mathrm{eq}} \leq B_{\mathrm{g}} \\ \frac{\rho_{\mathrm{FF}} J_0(T,B_{\mathrm{eq}})}{m+1} \left[\left(\frac{J+|J_{\mathrm{cm}}(T,B_{\mathrm{eq}},\sigma)|}{J_0(T,B_{\mathrm{eq}})}\right)^{m+1} - \left(\frac{|J_{\mathrm{cm}}(T,B_{\mathrm{eq}},\sigma)|}{J_0(T,B_{\mathrm{eq}})}\right)^{m+1}\right] & \text{for } B_{\mathrm{eq}} > B_{\mathrm{g}} \end{cases} \tag{3.3.1}$$

where B_{g} is so-called glass-liquid transition magnetic flux density. ρ_{FF} is the resistivity for uniform flux flow. J_0 and m are the scaling factor describing the width and the statistic parameter characterizing the shape of a critical current density, J_{c}, distribution. J_{cm} is the minimum value of J_{c} in the distribution. The transition magnetic flux densities B_{GL} and B_{k} are defined as the ones where J_{cm} and J_{k} are zero, respectively. Temperature-dependence of B_{GL} and B_{k} are described as follows, by the prediction of the two-dimensional d-wave

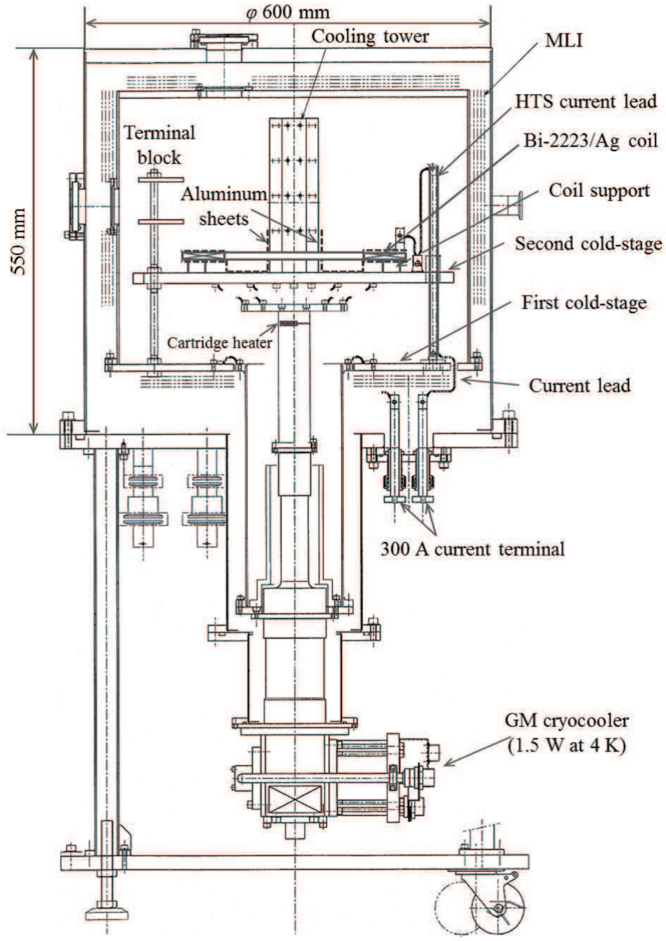

(a) Schematic diagram

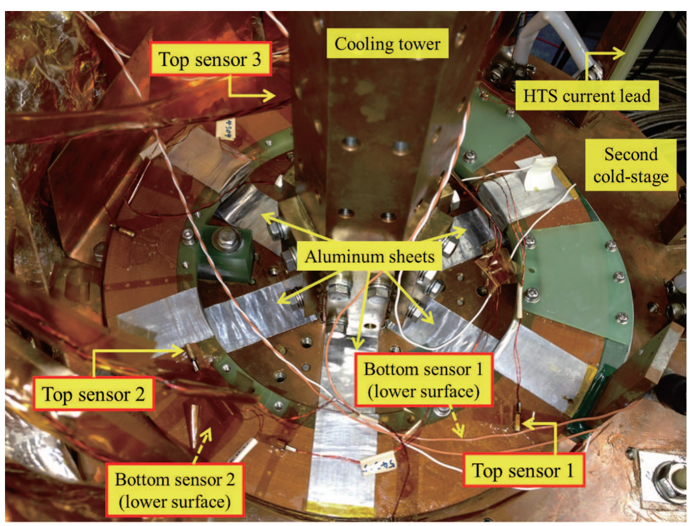

(b) Photograph

Figure 3.4: Cooling structure of the inside of the vacuum chamber. The second cold-stage and cooling tower were sufficiently cooled down to the operational temperature. (b) Three top thermo-sensors and two bottom thermo-sensors were installed at the surfaces of the coil.

symmetry [67].

$$
\begin{aligned}
B_{\mathrm{GL(or\,k)}} = \frac{b}{1-\nu_{\mathrm{p}}}\left(1-\frac{T}{T_{\mathrm{c}}}\right)\Bigg\{1-\frac{a}{1-T/T_{\mathrm{c}}} \\
+\sqrt{\left(1+\frac{a}{1-T/T_{\mathrm{c}}}\right)^{2}-4\nu_{\mathrm{p}}\frac{a}{1-T/T_{\mathrm{c}}}}\Bigg\}
\end{aligned} \tag{3.3.2}
$$

where a, b and ν_{p} are fitting parameters. Furthermore, magnetic field and temperature-dependence of J_{cm} and J_{k} can be obtained by the scaling of the pinning force density. The minimum value and the typical value of the pinning force density F_{pm} and F_{pk} are shown as follows [68]:

$$
\begin{aligned}
F_{\mathrm{pm}} &= J_{\mathrm{cm}}B \\
&= A\left(B_{\mathrm{GL}}^{\perp}f(\phi)\right)^{\zeta}\left(\frac{B}{B_{\mathrm{GL}}^{\perp}f(\phi)}\right)^{\gamma}\left(1-\frac{B}{B_{\mathrm{GL}}^{\perp}f(\phi)}\right)^{\delta}.
\end{aligned} \tag{3.3.3}
$$

$F_{\mathrm{pk}} = J_{\mathrm{k}}B$ is also given by the same form as eq. (3.3.3). A, ζ, α, γ and δ are pinning parameters. In order to take into account the dependence of the applied angle of the magnetic field, we use so-called equivalent perpendicular magnetic flux density, B_{eq}, [69] as

$$
B_{\mathrm{eq}} = B(\cos^2\phi + \frac{1}{\gamma^2}\sin^2\phi)^{\frac{1}{2}} \tag{3.3.4}
$$

where ϕ is an angle between the applied magnetic field and the perpendicular direction with respect to the broad surface of the tape. γ is the anisotropy ratio representing the misorientation of grains in HTS tapes as follow:

$$
\gamma = \frac{B_{\mathrm{g}(\phi=90^\circ)}}{B_{\mathrm{g}(\phi=0^\circ)}} \tag{3.3.5}
$$

The agreements between the percolation depinning model and experimental results of short samples (30 mm length HTS tapes) were confirmed at a variety of the amplitudes and angles of magnetic field as well as temperatures [66]-[69].

The strain, ε, dependence of the $E-J$ characteristics can be expressed by taking into account the strain dependence of the maximum pinning force density F_{pmmax} and F_{pkmax} as follows [64, 70, 71]:

$$F_{\mathrm{pmmax}\,or\,\mathrm{pkmax}}(T,\varepsilon) = f(\varepsilon) F_{\mathrm{pmmax}\,or\,\mathrm{pkmax}}(T,0) \tag{3.3.6}$$

$$f(\varepsilon) = A\left(1 - \left|\frac{\varepsilon - \varepsilon_{\mathrm{zero}}}{\varepsilon_{\mathrm{lim}} - \varepsilon_{\mathrm{zero}}}\right|^{\nu}\right) \tag{3.3.7}$$

$\varepsilon_{\mathrm{zero}}$, $\varepsilon_{\mathrm{lim}}$, ν, A are the parameters for materials. The above-mentioned fitting and pinning parameters, i.e., m, ρ_{FF}, A, ζ, α, γ, δ, a, b and ν_{p} can be obtained from experiments using a short HTS tape sample.

Furthermore, it was experimentally reported that the longitudinal inhomogeneity of the critical current of an HTS tape as shown in Fig. 3.5 can be approximated by a Gaussian distribution [72]. We now consider this longitudinal distribution of the local critical currents by assuming that the minimum critical current density, J_{cm}, in eqs. (3.3.1) has a Gaussian distribution with a specific standard deviation σ in the longitudinal direction. That is, the probability density function of J_{cm} along the longitudinal direction in the 200 m length tape can be described as shown in Fig. 3.6. The statistical calculation for this distribution in the long length tape is mentioned in the following section.

We measured the perpendicular magnetic flux density $B^{\perp}$ and temperature dependence of $E-J$ characteristics using a short-length sample of the Bi-2223/Ag tape, in order to determine the fitting and pinning parameters of the percolation depinning model. The tape was the same used for the scale-down model coil (4.2 mm wide, 0.28 mm thick), and the short sample (30 mm in length) was utilized for the measurement. Figure 3.7 shows a schematic diagram of the sample holder. The sample was installed on the cold head of a GM cryocooler. The voltage between two taps, 10 mm in distance, was measured by means of the direct current four points method. Magnetic field, perpendicular to the sample surface, was applied to the sample and the operational temperature was from 65 K to 77 K.

Figure 3.8 shows the obtained $B^{\perp}$-dependence of $E-J$ characteristics at 77 K. The symbols (solid circles) show the experimental results and the solid curves the fitted results by using Eqs. 3.3.1. As can be seen, the experimentally obtained $B^{\perp}$-dependence of the $E-J$ curves at 77 K was well reproduced by the percolation depinning model.

3.3.2 Current Transport Performance and Thermal Behavior of HTS Coil

Figure 3.9 shows (a) the three-dimensional (r, z, θ in cylindrical coordinates) analysis model of the double-pancake coil and (b) the flow-chart of the simulation. Since the coil is cooled

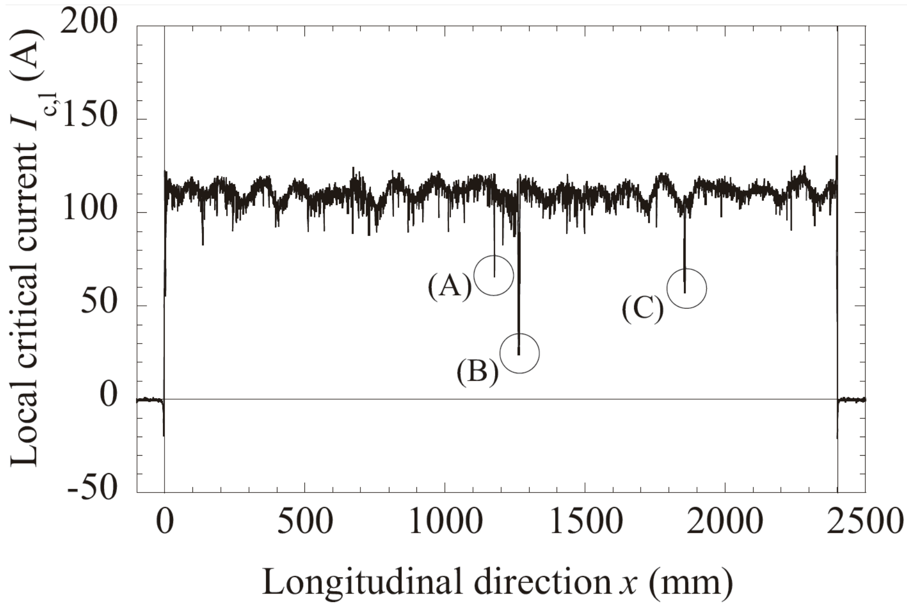

Figure 3.5: Experimental result of the local critical current in the GdBCO sample at 77 K [72].

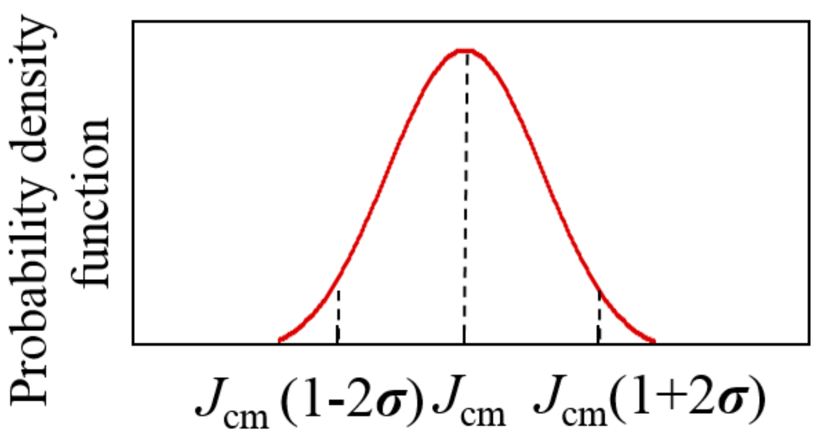

Figure 3.6: Probability density function of the minimum critical current, J_{cm}, along the longitudinal direction in the HTS tape.

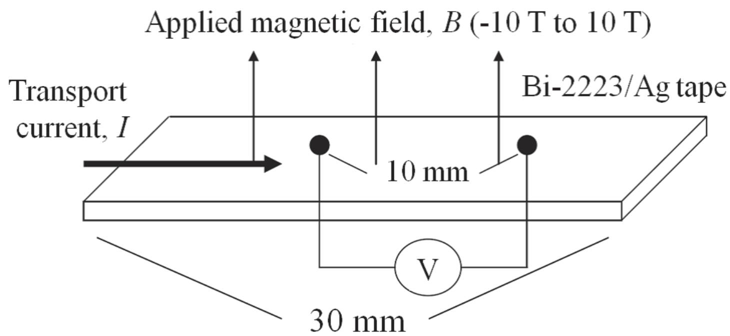

Figure 3.7: Schematic configuration of the sample holder for the measurement of magnetic field and temperature dependence of the $E - J$ characteristic of Bi-2223/Ag tapes.

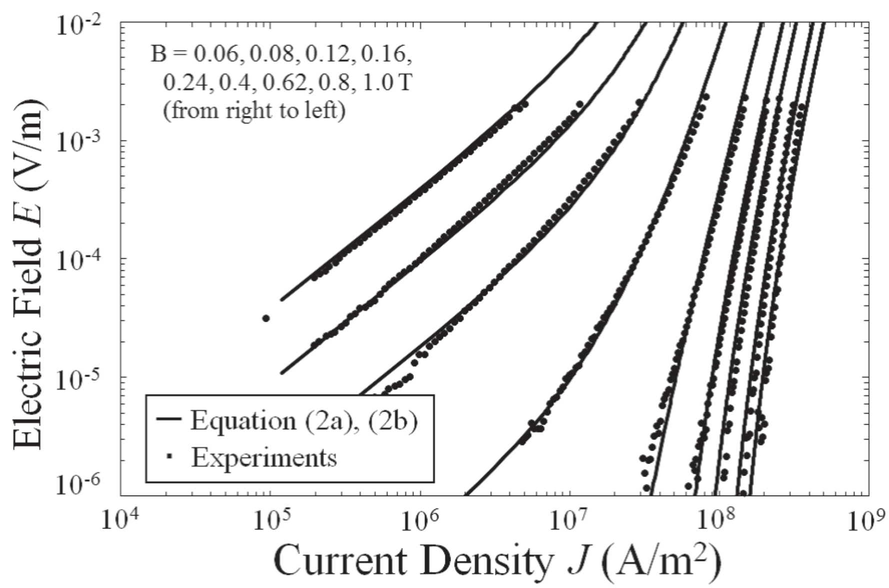

Figure 3.8: Perpendicular magnetic field-dependence of $E - J$ characteristics in the Bi-2223/Ag short (30 mm) sample at 77 K.

only by the aluminum sheets as mentioned in section 3.2.3 and the amount of the radiation cooling is much smaller and can be ignored, the boundary conditions for the temperature are set as stated in Fig. 3.9(a). We analyze the current transport property and thermal behavior of the HTS coil with taking into account the distributed electric field, i.e. $E_{r,z,\theta}(J,\ T_{r,z,\theta},\ B_{r,z,\theta},\ \phi_{r,z,\theta},\ \sigma)$, in the coil based on the percolation depinning model. The subscript, r, z, θ, means the position of the turn in the coil. The simulation is carried out by the following steps:

STEP1: Set the initial conditions, i.e. the initial transport current, I_{op}, operational temperature, T_{op}, and a standard deviation, σ, of the longitudinal variation in Fig. 3.6.

STEP2: By using the Biot-Savart law, calculate the distribution of the self-magnetic flux density, $B_{r,z,\theta}$, and its angle, $\phi_{r,z,\theta}$, in the coil.

STEP3: The distribution of the electric field, $E_{r,z,\theta}$, in the coil is computed by substituting J, $B_{r,z,\theta}$, $\phi_{r,z,\theta}$, and the coil temperature, $T_{r,z,\theta}$, into Eqs. (3.3.1). Since the minimum critical current density, J_{cm}, in each position in the coil is randomly determined according to the probability density function shown in Fig. 3.6, the calculation of the electric fields must be statistically processed [72]. The distribution of the electric filed, $E_{r,z,\theta}$, is obtained by the average value of 100 times calculations of STEP3.

STEP4: Terminal voltage, V, of the coil is computed by summing up the local electric fields, $E_{r,z,\theta}$, as eq. (3.3.8).

$$V = \sum_{r,z,\theta} r\theta E_{r,z,\theta} \tag{3.3.8}$$

STEP5: Calculate the heat generation per unit volume by $J \cdot E_{r,z,\theta}$ and solve the three-dimensional heat balance equation by finite difference method. The temperature distribution, $T_{r,z,\theta}$, in the coil is computed.

$$\begin{aligned} C\frac{\partial T}{\partial t} = \frac{1}{r}\frac{\partial}{\partial r}\left(\kappa r\frac{\partial T}{\partial r}\right) + \frac{\partial}{\partial z}\left(\kappa\frac{\partial T}{\partial z}\right) \\ + \frac{1}{r^2}\frac{\partial}{\partial \theta}\left(\kappa\frac{\partial T}{\partial \theta}\right) + J \cdot E \end{aligned} \tag{3.3.9}$$

where C denotes specific heat, κ thermal conductivity, and t time. These thermal parameters of the Bi-2223/Ag tape were obtained in the previous chapter as shown in Fig. 2.10.

STEP6: STEP6 has two kinds of procedures for each section in this paper.

Section 3.4.1 Increase the current value of I_{op} and recalculate from STEP2 until the Maximum electric field in the coil exceeds 1.0 $\times 10^{-4}$ Vm^{-1}, which is the electric field criterion of the minimum critical current I_{cmin} [73, 74]. We finally obtain the current, I, versus voltage, V, characteristics and the critical current, I_{cmin}, of the HTS coil.

Section 3.4.2 Recalculate from STEP3 at a fixed current value, I_{op}, until the coil temperature, $T_{r,z,\theta}$, diverges or converges to a specified temperature. If $T_{r,z,\theta}$ diverges, we decrease the current value of I_{op}, reset all $T_{r,z,\theta}$ to T_{op}, and recalculate from STEP2. We finally obtain the time evolution of the coil temperature at fixed current values and a quench current I_{q}, which is defined as the maximum current value in the case that $T_{r,z,\theta}$ converges.

We quantitatively compare the analysis results with experimental ones using the scale-down model coil in order to verify the validity of this analysis method, and examine the effect of the longitudinal inhomogeneity of the critical current on the coil performances.

3.4 Results and Discussion

3.4.1 Current Transport Performance of Scale-down Model Coil

The current transport property of the Bi-2223/Ag scale-down model coil as well as YBCO coil was firstly measured in liquid nitrogen (77 K). This cooling environment can cool the coils to 77 K uniformly, and the $I-V$ curve of the coils exactly at 77 K can be obtained. The experimental results are shown as symbols (solid circles) and the analysis results described in section 3.3.2 are plotted as curves in Figs. 3.10 and 3.11. In this analysis, the boundary condition of the whole coil surface for the temperature is set as the Dirichlet condition. As can be seen in Fig. 3.10, the analysis results agree well with the experimental ones with the standard deviation, σ, of the longitudinal inhomogeneity from 0.00 to 0.04. This result indicates that, as is well known, the longitudinal distribution of the current transport property of the Bi-2223/Ag tape is almost uniform, at least, over the length of 200 m. This is important for the practical design of the HTS coil. The agreement between the experimental result and the analysis assures the integrity of the analysis method. As can also be seen in Fig. 3.10, with increasing σ, the $I-V$ curve of the HTS coil is deteriorated, that is, a

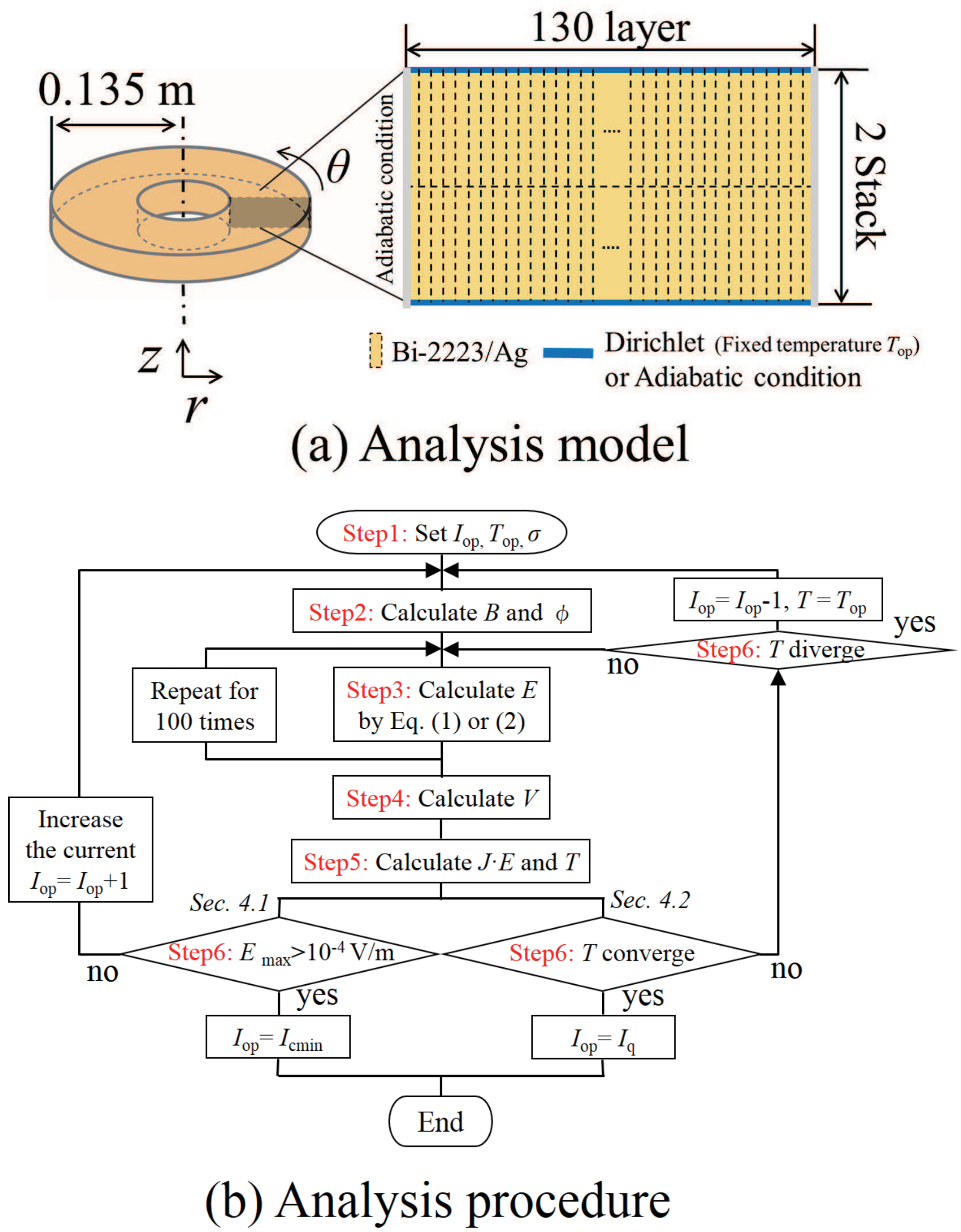

Figure 3.9: (a) Three-dimensional analysis model and (b) flow-chart of estimating the $I-V$ characteristics or the thermal behavior of the HTS coil. (a) The Dirichlet condition is set at the top and bottom surfaces with the aluminum sheets, and the Adiabatic condition is set at the other surfaces.

lower current generates a higher voltage. Our analysis results indicate that the longitudinal inhomogeneity of the critical current of the HTS tape adversely affects the current transport performance of the HTS coil. The difference between the experimental and analysis result is minimized at $\sigma = 0.02$, and the standard deviation, σ, of the longitudinal inhomogeneity of the Bi-2223/Ag tape is set to 0.02 in the following analyses. On the other hand, in the case of the YBCO coil, the experimental result is consistent with the analysis result of$\sigma = 0.17$. This result suggests that the local critical current of the YBCO coated-conductor greatly vary in the longitudinal direction as the making process of the YBCO coated-conductor has not yet been matured.

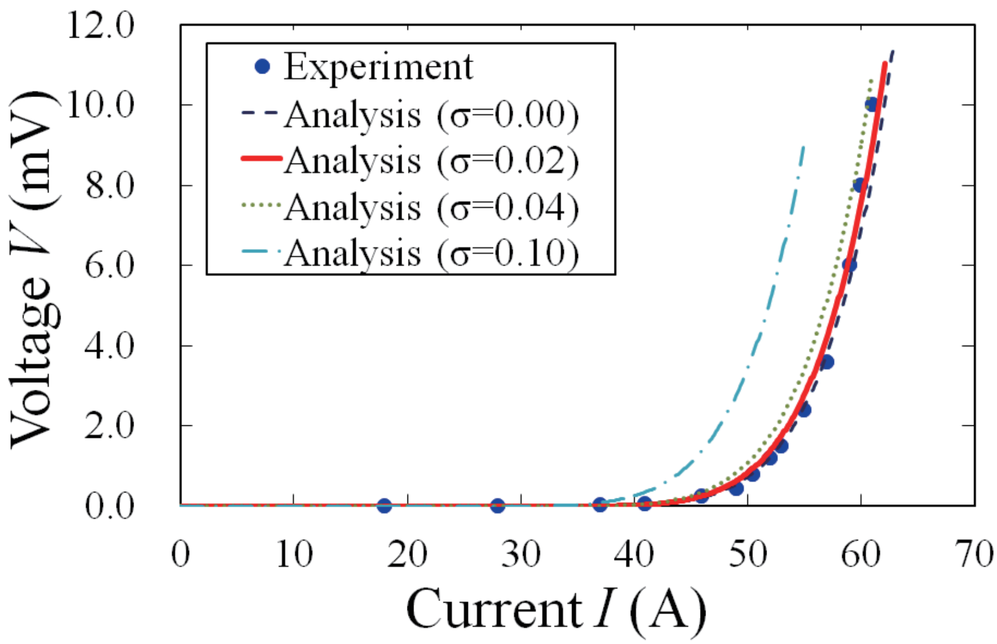

Figure 3.10: $I - V$ characteristic of the Bi-2223/Ag scale-down model coil cooled by liquid nitrogen (77 K). In the analysis, the standard deviation, σ, of the longitudinal inhomogeneity is changed from 0.00 to 0.10.

Figure 3.12 shows the distribution of (a) the magnetic field, $B_{r,z}$, and (b), (c) electric field, $E_{r,z}$, in the cross sectional area of the Bi-2223/Ag double-pancake coil. These distributions are obtained by the analysis process (STEP2 and 3) at $I_{\text{op}} = 63$ A and $T_{\text{op}} = 77$ K. Fig. 3.12(a) and (b) indicate that the magnetic and electric field are highly localized in the coil [62], and Fig. 3.12(c) shows that, with increasing σ, the maximum electric field in the coil is increased and also more irregularly distributed. Obviously, the HTS coil's performances must be described by considering these distributions, which can easily generate the hot spot in the HTS coil. The analysis of the thermal stability of the HTS coil, described in section

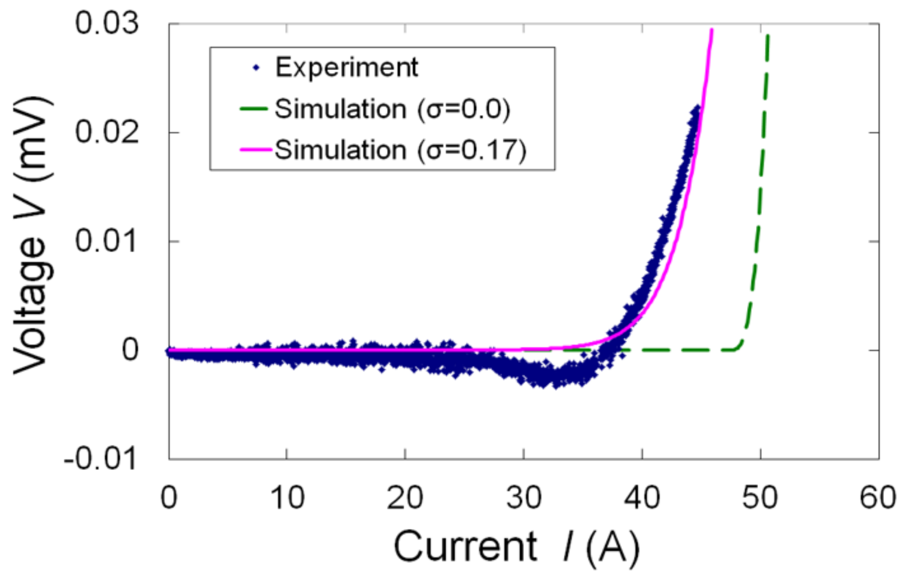

Figure 3.11: $I-V$ characteristic of the YBCO coil cooled by liquid nitrogen (77 K). In the analysis, the standard deviation, σ, of the longitudinal inhomogeneity is changed from 0.00 to 0.17.

3.4.2, is crucially important to avoid the hot spot and the quench in the coil.

Next, we measured the current transport properties of the scale-down model coil for different operational temperatures. In this experiment, the coil was set as in Fig. 3.4 at the conduction-cooling condition. The purpose of these measurements is to characterize the fabricated scale-down model coil and experimental system at various operational temperatures by means of the developed analysis code. Understanding the temperature-dependence of the performance of the HTS coil is useful to determine the optimal coil system and temperature for the magneto plasma sail. In the analysis, the boundary condition, T_{op}, at both top and bottom surfaces of the coil with aluminum sheets are set to the average values obtained by the top thermo-sensors and the bottom thermo-sensors in the experiments, respectively. We repeated the simulation procedure in section 3.3.2 from 4 to 80 K and the experiments from 45 to 80 K for obtaining the temperature-dependence of the current transport property of the scale-down model coil (here, σ is set to 0.02).

Figure 3.13 shows the temperature-dependence of (a) the $I-V$ curve and (b) the critical current of the Bi-2223/Ag scale-down model coil, obtained from the experiments (symbols) and the analysis (solid curve). In Fig. 3.13(b), the horizontal axis is the average of the top and bottom coil temperatures, and the vertical axis is the minimum critical current I_{cmin}, determined by the electric filed criterion as mentioned in section 3.3.2 (STEP 6). In Fig. 3.13(b), the effects of the temperature variation of the coil surfaces on the analysis results

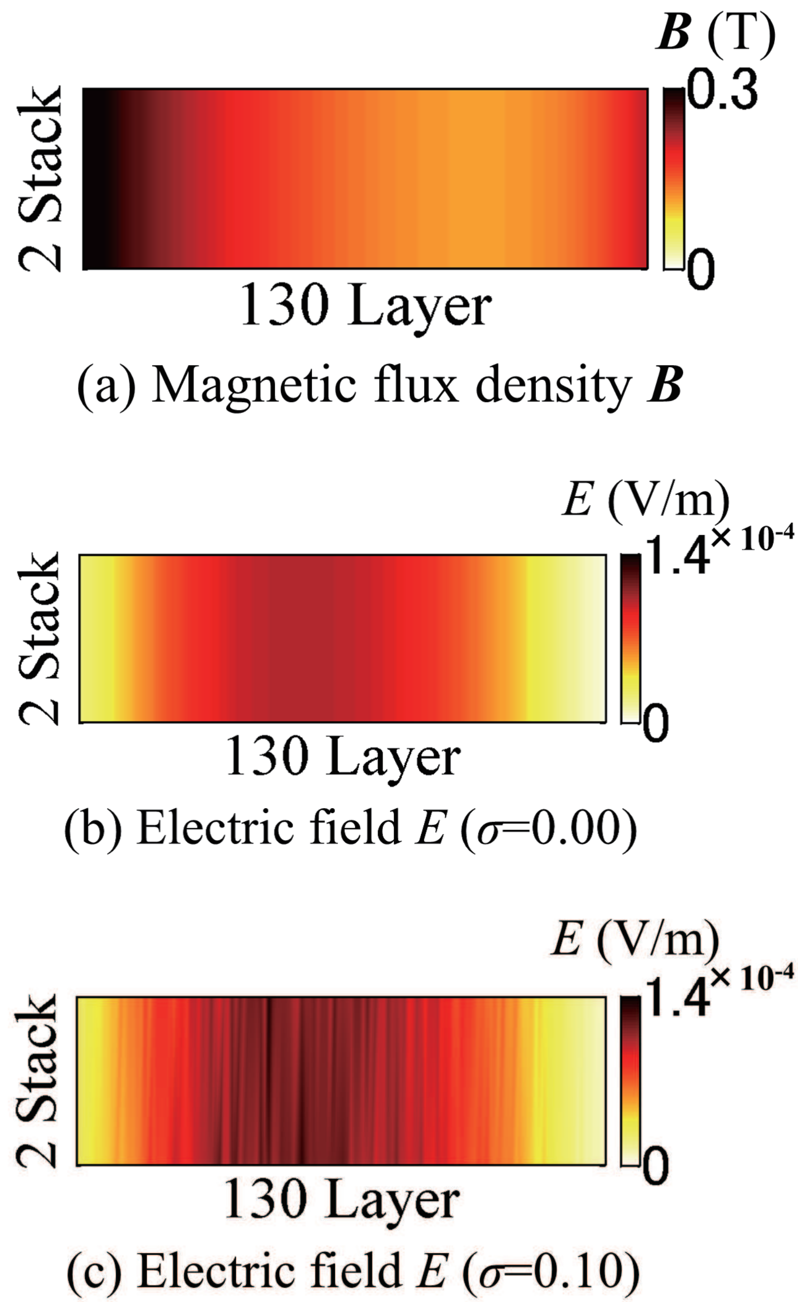

Figure 3.12: Analysis results of the distribution of (a) the magnetic and (b), (c) electric field in the cross sectional area of the scale-down model coil described in Fig. 3.9(a) ($I_{\mathrm{op}} = 63$ A, $T_{\mathrm{op}} = 77$ K). (b) $\sigma = 0.00$, (c) $\sigma = 0.10$.

are described as error bars. Note that the analysis results of the critical current from 4 to 80 K are obtained not from the $I-V$ curve of the short sample but that of the coil itself, in which locally distributed electric field (shown in Fig. 3.12) is quantitatively taken into account. We successfully estimated the $I-V$ curves and critical currents of the HTS coil at the wide range of the coil temperatures from 45 to 80 K within the errors which are caused by the temperature variation. The larger estimation error at the lower temperature (45 - 48 K) was caused because the temperature variation on the coil surface became widened at a lower temperature and also $E-J$ curves of the HTS tape were formulated by data only at higher temperature (65 - 77 K). These results indicate that the current transport property of the conduction-cooled HTS coil, including the temperature-dependence, can be sufficiently predicted on the basis of the percolation depinning model. The agreement between the experimental and analysis results also proves the integrity of the conduction-cooling system.

3.4.2 Thermal Behavior of Scale-down Model Coil

Estimating the thermal stability of the HTS coil is surely important for practical operations because the minimum critical current, I_{cmin}, described in previous section 3.4.1 is not necessarily consistent with the quench current, I_{q} (defined in section 3.3.2 STEP 6), of the HTS coil. We measured the temperature traces as well as its distribution on the coil during current applications under the conduction-cooled condition as in Fig. 3.4. The experimental results are compared with the thermal analysis ones in order to validate our thermal analysis of the HTS coil in section 3.3.2.

Figure 3.14 illustrates the analysis result of the distribution of the temperature rises, ΔT, on the top surface of the coil after $I_{\mathrm{op}} = 63$ A ($=I_{\mathrm{cmin}}$) is applied for seven minutes ($t = 420$ s, σ is set to 0.02). Only a half circle of the coil is described because of the symmetry of the cooling structure. As can be seen in Fig. 3.14, ΔT are barely distributed in a circumferential direction. We obtained the consistent result in the experiment by the three top thermo-sensors on the coil. This result confirms that the conduction cooling system effectively functioned and cooled the coil uniformly, although the coil was cooled only by the aluminum sheets which were placed with intervals for the limitation of the cooling path.

Figure 3.15 shows the time evolution of the temperature rises, ΔT, at top sensor 1 (Fig. 3.4(b)) on the scale-down model coil at $I_{\mathrm{op}} = 63$, 61, or 56 A and $T_{\mathrm{op}} = 77$ K. The experimental results are shown as symbols and the analysis as solid curves. The temperature rises obtained by the analysis agree well with the experimental ones for the various operational currents I_{op}. This result shows that, in addition to the current transport performance, the thermal behavior of the conduction-cooled HTS coil can be well described by the analysis based on the percolation depinning model with taking into account the cooling constraint condition.

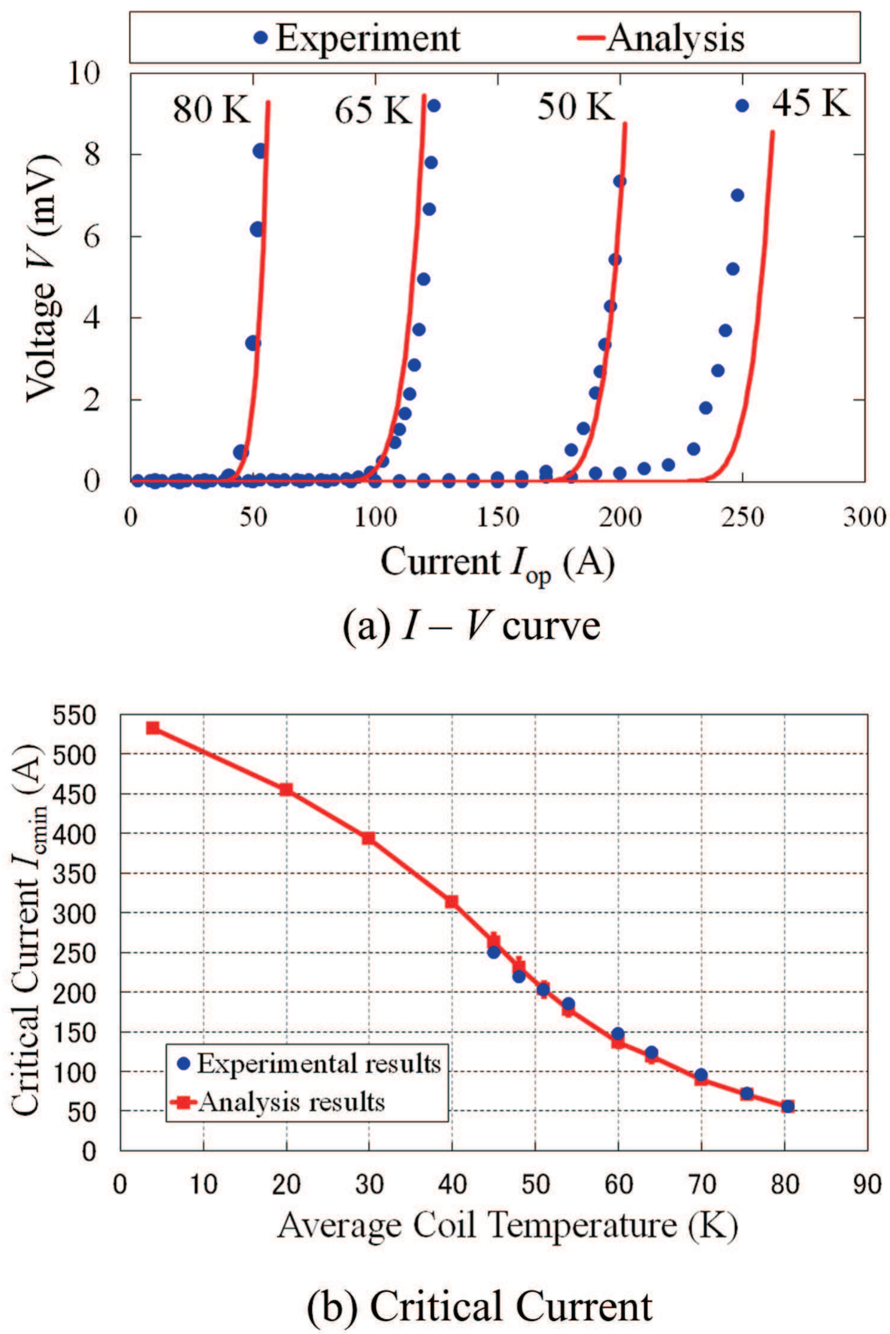

Figure 3.13: Temperature-dependence of (a) the $I - V$ curve and (b) the critical current of the Bi-2223/Ag scale-down model coil ($\sigma = 0.02$).

Furthermore, although the minimum critical current, I_{cmin}, at 77 K estimated in section 3.4.1 is 63 A, the coil quench occurs at $I_{\mathrm{op}} = 63$ A in the thermal analysis, i.e. the coil temperature diverges at this current as shown in Fig. 3.15. This result suggests that the electric field criterion, 1.0×10^{-4} Vm^{-1}, is not sufficient in order to avoid the coil quench especially under the conduction-cooled condition. The coil temperature converges to a specified temperature at $I_{\mathrm{op}} = 56$ A and the quench current, I_{q}, at 77 K is estimated as 56 A by our thermal analysis. Fig. 3.16 shows an example of the time transient of the distribution of the temperature at the top surface of the scale-down model coil when the thermal runaway occurs. It can be seen that the quench occurs locally around the center of the top surface of the coil.

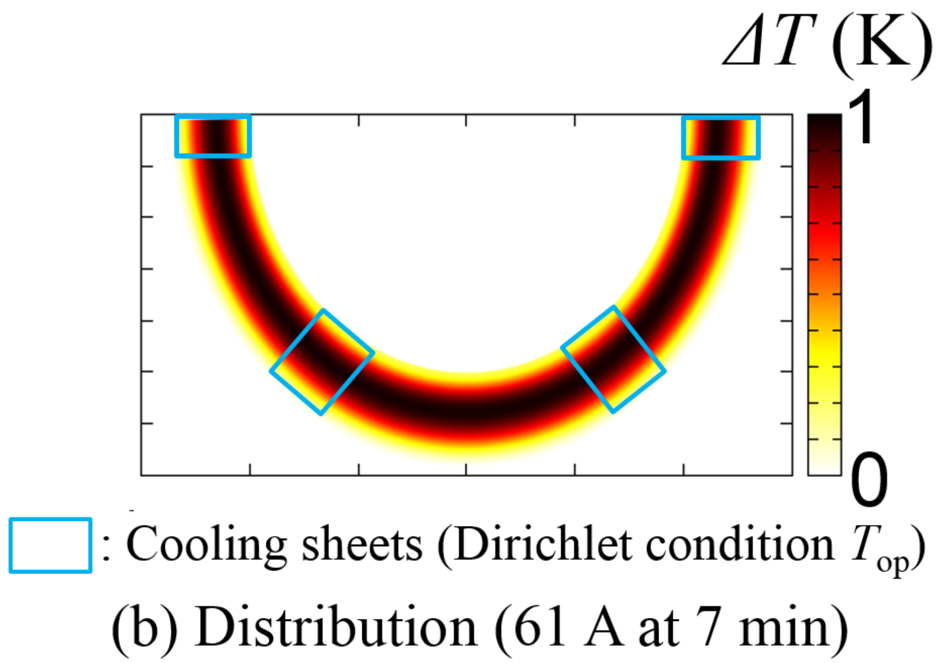

Figure 3.14: Analysis result of the distribution of the temperature rises, ΔT, at the top surface of the scale-down model coil ($I_{\mathrm{op}} = 63$ A, $T_{\mathrm{op}} = 77$ K, $t = 420$ s, $\sigma = 0.02$).

We perform the same analysis at different operational temperatures, and obtain the quench currents, I_{q}, for various operational temperatures. Figure 3.17 shows the analysis result of the temperature-dependence of the maximum electric field and total heat value in the coil at the coil quench. Figure 3.17 also contains the relation between the $I-V$ curve and quench current, I_{q}, for various operational temperatures. As can be seen in Fig. 3.17, the smaller electric field, coil voltage, and heat generation cause the coil to be quenched at the lower coil temperature. This result comes from the fact that, because the heat capacity of the Bi-2223/Ag tape decreases with the lower temperature, the temperature rises in the coil

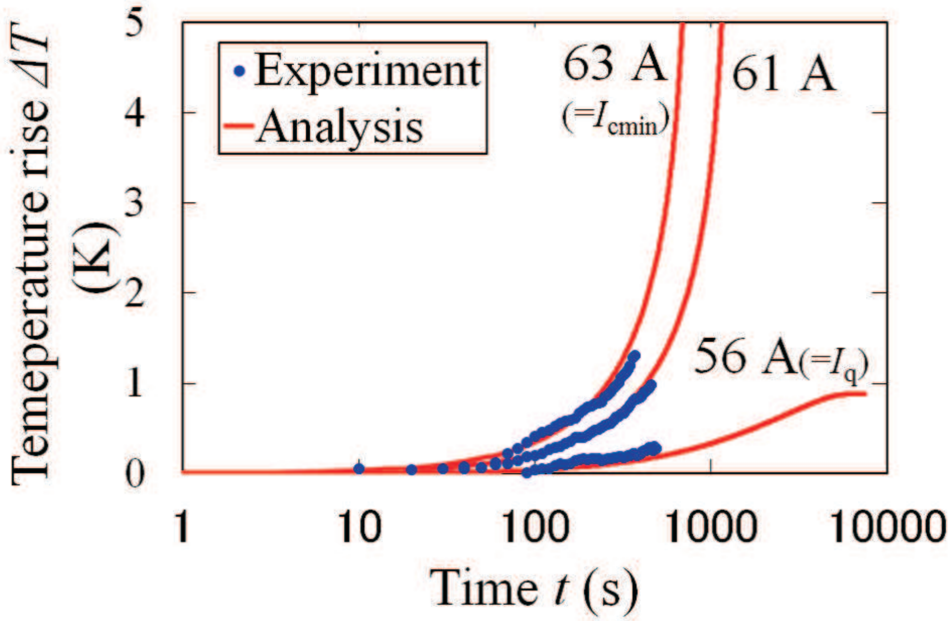

Figure 3.15: Time evolution of the temperature rises, ΔT, at top thermo-sensor 1 in Fig. 3.4(b). The currents (I_{op} = 63, 61, 56 A) were applied from t = 0 s (σ = 0.02, T_{op} = 77 K).

increases and the thermal stability of the coil decreases at the lower coil temperature. Note that, at less than 30 K, the electric fields which are more than one order of magnitude smaller than the common electric field criterion, 1.0 $\times 10^{-4}$ Vm^{-1}, bring about the coil quenches.

Figure 3.18 indicates the analysis result of the temperature-dependence of the quench current of the scale-down model coil and the influence of the longitudinal inhomogeneity on the quench current I_q. The quench current decreases with increasing the standard deviation, σ, of the longitudinal inhomogeneity. This result suggests that the critical current variation along the length of the HTS tape deteriorates the thermal stability of the coil and decreases the quench current I_q. This is caused because the local electric field, i.e. the heat generation, becomes higher and more irregularly distributed with increasing σ as shown in Fig. 3.12, and the coil can be easily quenched at this point.

As can also be seen in Fig. 3.18, the quench current of the scale-down model coil (σ = 0.02) is estimated as more than 400 A at the temperatures less than 20 K. The fabricated coil achieved the magnetomotive force, NI, at 10^5 A-turns at 20 K, which is one order of magnitude smaller than that of our targeted magneto plasma sail drive coil.

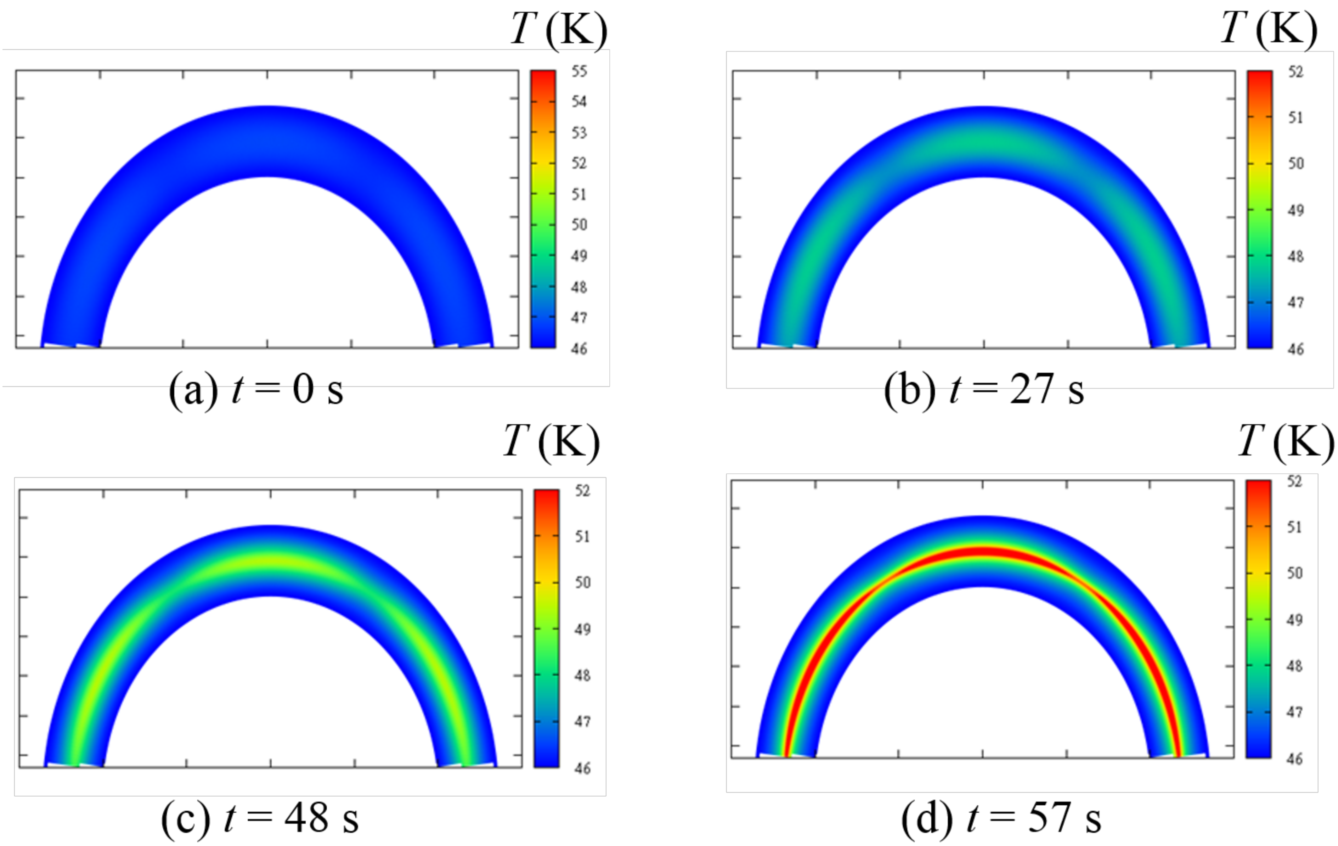

Figure 3.16: Simulation result of an example of the time transient of the distribution of the temperature at the top surface of the scale-down model coil when the thermal runaway occurs ($I_{\mathrm{op}} = 240$ A, $T_{\mathrm{op}} = 46$ K, $\sigma = 0.02$).

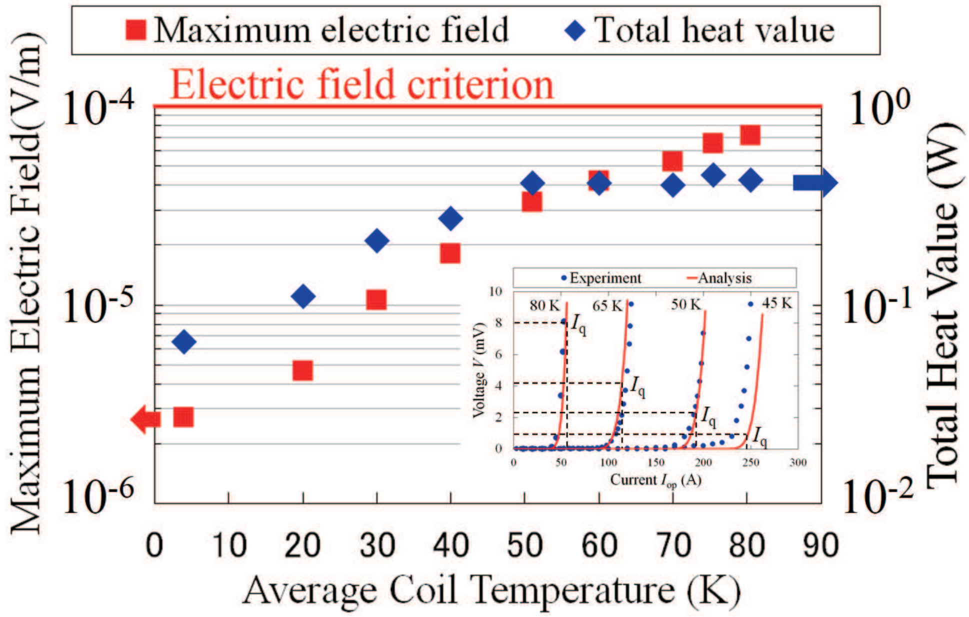

Figure 3.17: Analysis result of the temperature-dependence of the maximum electric field, terminal voltage, and total heat value in the scale-down model coil at the coil quench ($\sigma = 0.02$).

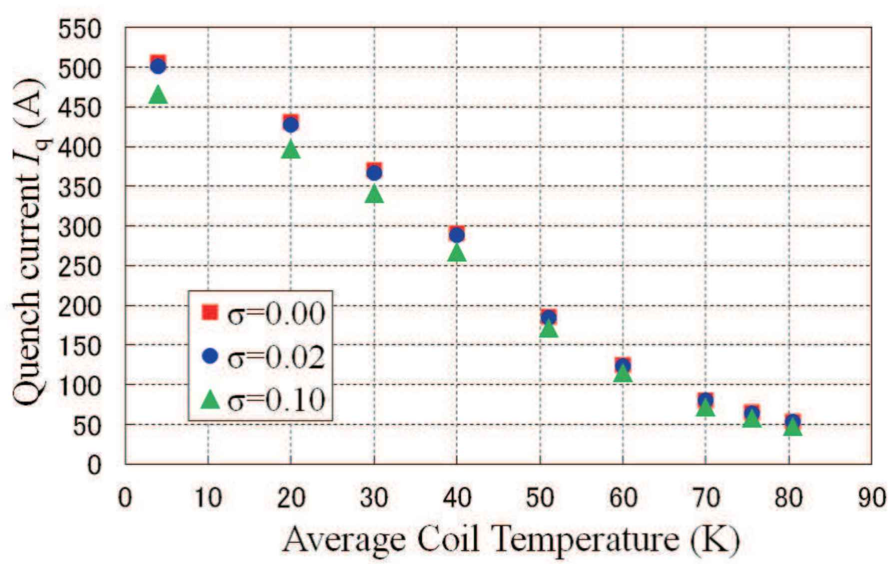

Figure 3.18: Analysis result of the temperature-dependence of the quench current of the Bi-2223/Ag scale-down model coil ($0.00 \leq \sigma \leq 0.10$).

3.5 Summary

We reported an analysis method to estimate the current transport properties and thermal stabilities of HTS coils, in order to design the optimal coil system for the magneto plasma sail spacecraft. This method made use of $E - J$ characteristics according to the percolation depinning model. The developed analysis for thermal stability can estimate the current which causes an HTS coil to be quenched by solving the three-dimensional heat balance equation. The analysis showed that this quench current of the coil was not consistent with the critical current based on the electric field criterion, 1.0 $\times 10^{-4}$ Vm^{-1}. In the analysis, the longitudinal inhomogeneity of the critical current of the HTS tape was considered for more precise estimation, and it was confirmed that such inhomogeneity deteriorated the current transport performance and thermal stability of the coil. We also fabricated and established a Bi-2223/Ag scale-down model coil and a conduction-cooed experimental system. We showed that the current transport performance and thermal behavior of the coil obtained by the analysis with taking into account the cooling condition quantitatively agreed with the experimental ones at various operational temperatures. These results proved the validity of the analysis method and the conduction-cooling experimental system for the magneto plasma sail drive coil.

Chapter 4

Analysis Model for Screening Currents Induced in HTS Coil

4.1 Introduction

Due to the strict limitation of mass and power consumption for the spacecraft, a stabilized power supply for a superconducting coil cannot be used in space, and light-weight DC/DC converters as shown in Fig. 4.1, which contain AC ripples in output DC currents, are considered to be used as the regulation of the power supply in the spacecraft. The DC/DC converters can significantly save the total mass of the power supply system in the spacecraft using an HTS coil [75]. One potential problem can arise from AC ripples, i.e., AC current with DC offset, in the output current of the DC/DC converter, which could generate induced currents and AC losses in the HTS coil. Since a spacecraft cannot be equipped with any refrigerants, mostly because of mass considerations, the AC loss could become a serious problem for the reliability of an HTS coil as well as the design of the HTS coil system in space. Although recent studies experimentally investigated the AC losses in HTS coils under AC currents with DC offsets [76]-[78], these losses have not been sufficiently investigated by analyses based on a physically oriented current transport model of HTS tapes. The quantitative estimation of the AC loss with the ripple current and the effect on the coil performance, e.g., its thermal stability in a conduction-cooled condition, is an important factor in order to apply the DC/DC converter as the power supply for the HTS coil and determine the optimal coil system and operating condition for use in space. Moreover, the screening current I_s induced in the coil could have large effects on the magnetic field distribution and current transport characteristics of the HTS coil itself [79]-[82]. These effects must be estimated to design optimal HTS coil systems for space missions. In addition, understanding I_s is highly important for terrestrial applications, e.g. magnetic resonance imaging, nuclear magnetic resonance imaging and cyclotrons, which require stable magnetic fields [79]-[82]. In this study, we investigated a Bi-2223/Ag coil, which is a candidate for magneto plasma sail spacecraft. It has been reported that multi-filamentary Bi-2223/Ag tapes have superconducting connections (bridging) between neighboring filaments [83]-[88]. The filament bridging can have effects on the loop length and inductance of I_s in the coil, and as a result, the AC loss and magnetic field distribution generated by the coil itself. Koyama et al. reported that due to the filament bridging, flux creep was a dominant factor for I_s induced in a Bi-2223/Ag coil [89]. To analyze the AC loss, magnetic field distribution and optimal design for the Bi-2223/Ag, it is essential to develop an analytical method that considers flux creep and understands how I_s is induced in the Bi-2223/Ag coil.

To evaluate the AC loss and magnetic field distribution of HTS coils accurately, we developed an analytical method to investigate induced current I_s in a Bi-2223/Ag coil that considers the effect of flux creep. We validated the method by comparing calculated results to measured magnetic fields generated by I_s. Using the developed method, we also investigated the effects of the AC losses with a variety of ripple currents with DC offsets on the coil performance , and clarified the reliability of the conduction-cooled HTS coil under the ripple currents.

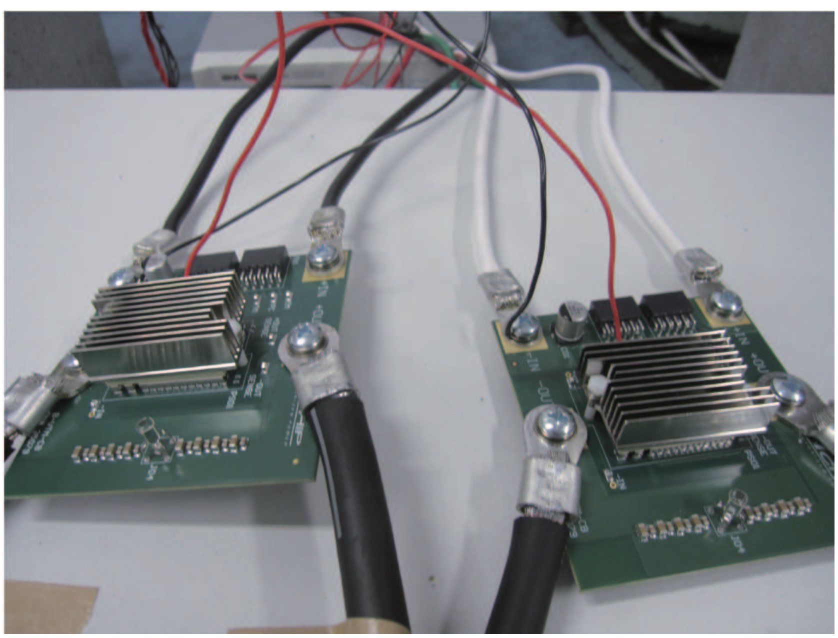

Figure 4.1: DC/DC converter for the regulation of the power supply.

4.2 Experiment

To investigate I_s induced in the coil during the coil excitation, we measured the axial magnetic fields generated by I_s with Hall sensors. The Hall sensors were installed at (I) the center and (II) the top surface of the scaled-down model coil (Fig. 3.1, Table. 3.1), as shown in Fig. 4.2. The residual magnetic fields due to I_s were obtained by subtracting the fields for the transport current (e.g. 1.17 mT/A at the center of the coil, calculated by the integration of the Biot–Savart law without any screening currents) from the measured values. We measured the loop inductance and magnitude of I_s in the Bi-2223/Ag coil and compared them with the analytical results from the model. To evaluate the inductance and loop length of I_s, the decay time constant, τ, was estimated. We measured the decay behavior of the magnetic field due to I_s by pausing the increase of the operational current, I_op, for several times during the excitation of the coil up to 200 A. The measurements were conducted under various conditions: at different temperatures from 4 to 50 K and with different sweep rates from 40 to 80 A/min.

To investigate the maximum ratio of the magnetic fields from I_s to those from the coil current, the hysteresis loops of the magnetization during charging and discharging of the coil were measured. The transport current was applied up and down to ±200 A at 50 K with a 40 A/min sweep rate.

4.3 Analytical Model for Screening Currents

We enhanced the developed thermo-electromagnetic field analysis model in the previous chapter by including the effects of flux flow and flux creep on I_s induced in HTS coils. Figure 4.3 shows the analysis model of the Bi-2223/Ag double pancake coil, whose features are described in Table. 3.1. I_s is induced by the temporal variation of the self-magnetic field, B_r, during the coil excitation and flow between filaments via the filament interconnections or silver sheath in the Bi-2223/Ag tape. We assumed I_s is induced by a single equivalent loop length, l, along the tape in the coil, as shown in Fig. 4.3 and current and electromagnetic filed distributions are uniform along the thickness of the tape. I_s was analyzed using Faraday's law, the percolation depinning model, the flux creep model and the equivalent circuit of the HTS coil.

The electric field, $\boldsymbol{E}_\mathrm{s}$, induced by the temporal variation of the radial component of the self-magnetic field B_r linked with the operational current, I_op, and I_s is expressed as follows:

$$\nabla \times E_\mathrm{s} = -\frac{\partial B_\mathrm{r}}{\partial t}. \tag{4.3.1}$$

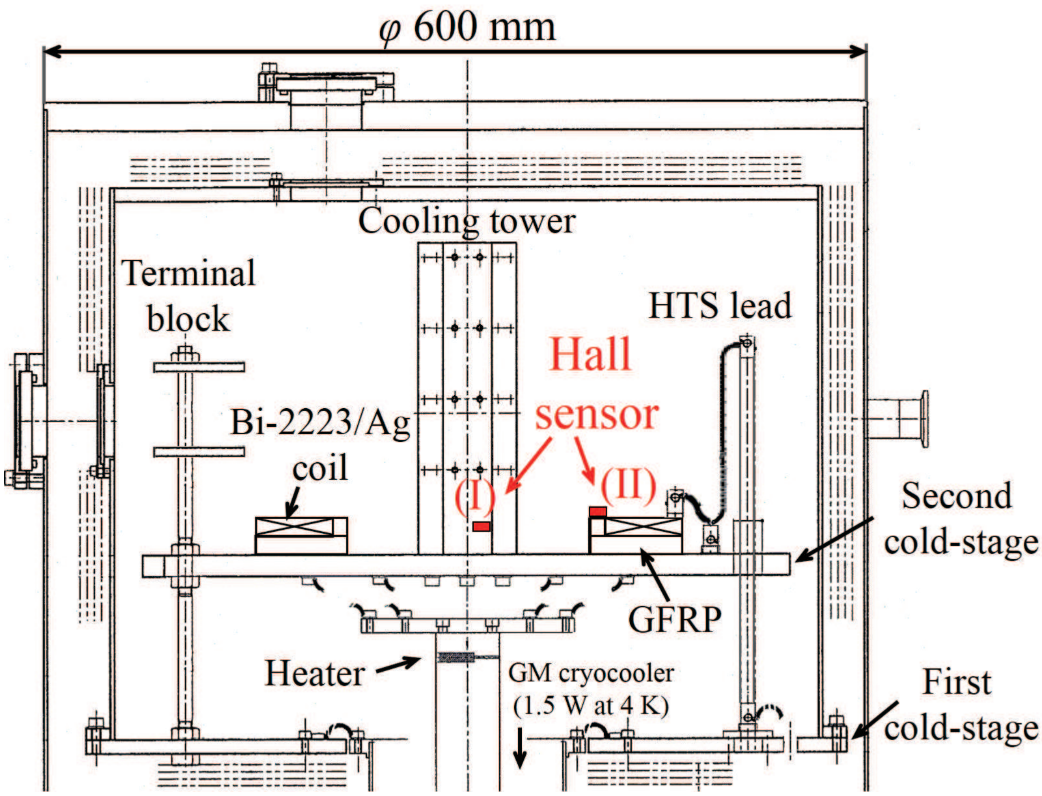

Figure 4.2: Schematic diagram of the inside of the vacuum chamber and setting of the Hall sensors for the experiments.

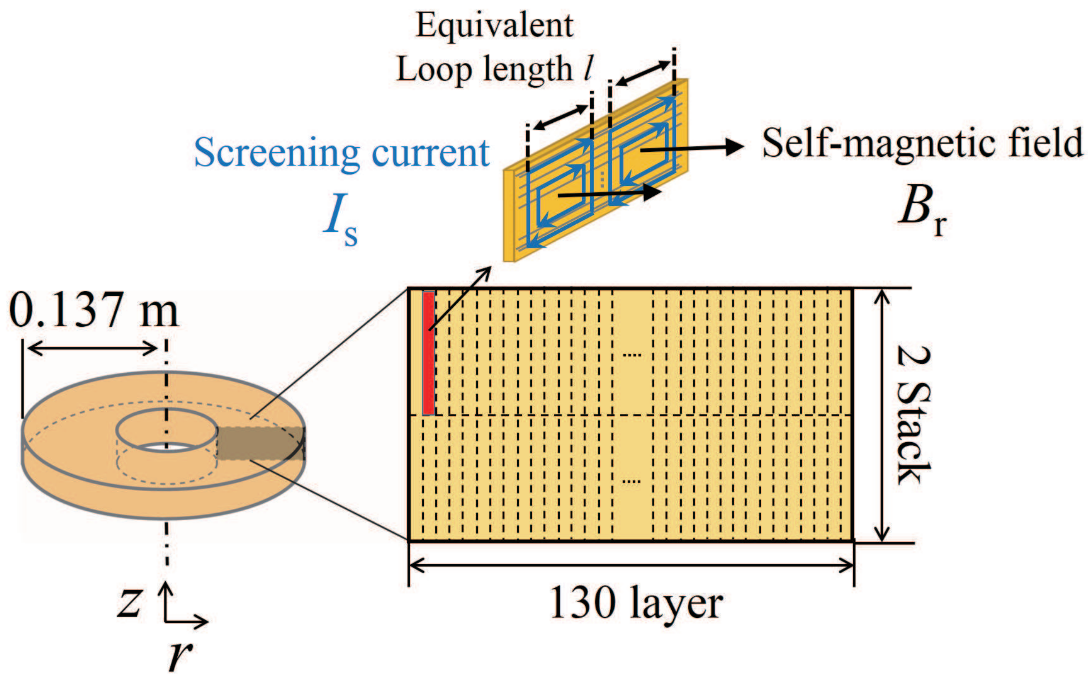

Figure 4.3: Analysis model of the Bi-2223/Ag double pancake coil. We assumed that all of the screening currents flowed with an equivalent loop length, l, in the Bi-2223/Ag coil.

$\boldsymbol{B}_{\mathbf{r}}$ at each time, t, is calculated using the Biot–Savart law.

Based on the percolation depinning model, the current density, J, versus the electric field, E, due to the flux flow relationship in HTS tapes can be described as a function of temperature, T, magnetic field and its applied angle [90],

$$J = \begin{cases} J_{\mathrm{cm}}(T, B_{\mathrm{eq}}) + \left(\frac{m+1}{\rho_{\mathrm{FF}}} E_{\mathrm{FF}} J_0(T, B_{\mathrm{eq}})^m\right)^{\frac{1}{m+1}} & \text{for } J_{\mathrm{cm}} \geq 0 \\ -\left|J_{\mathrm{cm}}(T, B_{\mathrm{eq}})\right| + \left(\frac{m+1}{\rho_{\mathrm{FF}}} E_{\mathrm{FF}} J_0(T, B_{\mathrm{eq}})^m + \left|J_{\mathrm{cm}}(T, B_{\mathrm{eq}})\right|^{m+1}\right)^{\frac{1}{m+1}} & \text{for } J_{\mathrm{cm}} < 0 \end{cases} \tag{4.3.2}$$

Considering the influence of thermally activated vortex hopping, i.e. flux creep, the relationship between J and E, especially in a lower load factor region, can be written as follows [91]:

$$E_{\mathrm{FC}} = \begin{cases} E_{\mathrm{c0}} \exp\left[-\frac{U(j)}{kT}\right]\left[1 - \exp\left(-\frac{\pi U_0 j}{kT}\right)\right] & \text{for } J < J_{\mathrm{c}} \\ E_{\mathrm{c0}} \exp\left[1 - \exp\left(-\frac{\pi U_0 j}{kT}\right)\right] & \text{for } J < J_{\mathrm{c}} \end{cases} \tag{4.3.3}$$

where $U(j) = U_0[(1{-}j^2)^{1/2}{-}j\cos^{-1}j]$, $E_{c0} = Ba_f v_0$ and $j = J/J_c$. a_f is the flux line lattice spacing, v_0 is the attempt frequency, U_0 is the height of the pinning potential for $j = 0$ and k is the Boltzmann constant. The total electric field from the flux flow and the flux creep can be calculated as the sum of the electric fields obtained from eq. 4.3.2 and eq. 4.3.3: $E(J) = E_{FF}(J) + E_{FC}(J)$ [92]. Figure 4.4 illustrates the equivalent circuit of the HTS coil. I_s can be obtained by satisfying the following equation:

$$\oint E_s ds = L_s \frac{\partial I_s}{\partial t} + RI_s, \tag{4.3.4}$$

where the subscript s and L_s, respectively, denote the loop element and the corresponding inductance for I_s as well as the resistance $R = R_{HTS} + (R_N \text{ or } R_{HTS})$. R_{HTS} is the equivalent resistance of the HTS tape based on the percolation depinning model 4.3.2 and the flux creep model 4.3.3. R_N is the resistance of the silver sheath [93] in cases where I_s flows across the silver matrix. We assume that the outermost current loops, shown in Fig. 4.3, flow via the filament interconnections with a length of l, and the inner current loops flow via the silver sheath in the Bi-2223/Ag tape. L_s is obtained by calculating B_r from only I_s.

The thermal stability of the coil during the ripple current application can be obtained by calculating the effective AC loss by $\rho_{HTS} J_s^2$ and solving the heat balance equation. ρ_{HTS} is the equivalent resistivity of the HTS tape based on the percolation depinning model and the flux creep model, and $J_s$is the screening current density. The detail procedure of the analysis for the thermal behavior of HTS coils is explained in section 3.3.2. The transport AC loss with the ripple current per unit volume per cycle, W, in the coil is computed as:

$$W = \frac{1}{v} \oint dt \int_v \rho_{HTS} J_s^2 dv, \tag{4.3.5}$$

where v is the total volume of the coil.

We compared the modeling results with the experimental ones assuming different values for loop length,l, for I_s to verify the validity of the analysis method and evaluate an equivalent l in the Bi-2223/Ag coil.

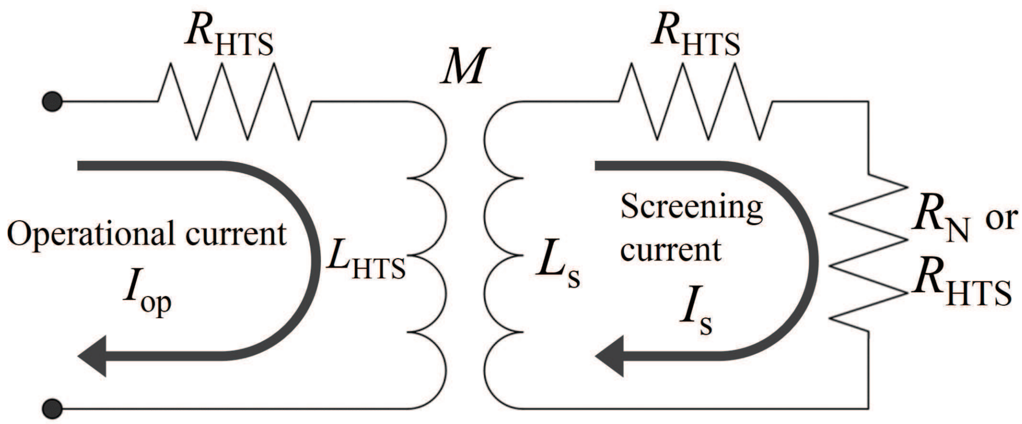

Figure 4.4: Equivalent circuit of the HTS coil. Both the operational transport current, I_{op}, and the screening current,I_s, in the HTS coil are considered.

4.4 Modeling Results

4.4.1 Decay Behavior of Screening Currents in the Bi-2223/Ag Coil

We first measured the decay behavior of I_s with long-term operation of the coil. Figure 4.5 shows the experimental result of the temporal variation of the residual magnetization due to I_s, which was obtained by subtracting the magnetic field generated by the coil current from the measured one at Hall sensor (I). In this experiment, we increased $I_{op}$from 0 to 80 A at a rate of 40 A/min. At 80 A ($t = 0$ in Fig. 4.5), I_{op} was fixed and the decay of the magnetization was measured. A typical logarithmic decay in the magnetization is shown by a dashed line in Fig. 4.5. This result indicates that the decay behavior of I_s in the Bi-2223/Ag coil is controlled by flux creep, as discussed by Koyama et al. [89] and Pust [94]. The result also suggests that much of I_s flows as persistent currents via the filament interconnections in the Bi-2223/Ag coil without any normal resistance [89]. Conversely, the rapid decay of the magnetization at $t < 3$ s in Fig. 4.5 suggests that some I_s in the Bi-2223/Ag coil flow across the silver sheath and rapidly disappear due to the resistance, R_N, of the silver sheath, as suggested by Koyama et al [89]. Approximately 46% of the magnetic field generated by I_s rapidly diminished at $t < 3$ s. Because of this decay behavior, we continued to consider both the flux creep and the silver sheath resistance in our analysis of I_s in the coil, as described in the previous section. As mentioned in section 4.2, we investigated the inductance and loop length, l, of I_s induced in the Bi-2223/Ag coil. We measured the decay time constant, τ, of the magnetic field generated by I_s due to the normal resistance, R_N, and fitted the model result to the measured one. The fitting parameter was l for I_s in the Bi-2223/Ag tape. The corresponding inductance, L_s, was obtained by calculating B_r from only I_s of the loop itself and $\tau = L_s/R_N$. Figure 4.6(a) shows the temporal variation of the experimental residual magnetization due to I_s at Hall sensor (I). As previously mentioned in section 4.2 and as shown in Fig. 4.6(a), we intermittently halted the increase of I_{op} six times and investigated τ for the condition of no induced electric fields, E_s, originating from I_{op} for various load factors, I_{op}/I_{cmin}, for the HTS coil. I_{op} was increased up to the minimum critical current, I_{cmin} = 200 A (when E_{max} = 1.0 μV/cm), with a fixed 40 A/min sweep rate and T = 50 K, and the magnetic field was measured every 0.5 s. The experimental results (solid circles) indicate that the magnetic field from I_s drastically decreased under constant current conditions with no induced electric field due to E_s. In addition, the decay ratio and τ of the magnetic field slightly decreased with increasing load factor, i.e. increasing resistance of the HTS tape, R_{HTS}. The fact that this rapid decay was observed even at an extremely low load factor, i.e. at a no flux flow region, suggests that the decay is caused mainly by the influence of R_N and the flux creep, as in the case shown in Fig. 4.5. At I_{op} = 20 A, for example, τ of I_s is estimated to be approximately 0.9 s. Figure 4.6(b) and Table. 4.1 depict the model fitting results assuming various values for l for I_s. The maximum value and decay time constant of the magnetic field for each l are shown in Table. 4.1. Considering the standard deviation of the measurements, the experimental results can be successfully modeled using $l = 9 \pm 3$ mm. This value of l is of the same order as the length of the filament bridging in a Bi-2223/Ag tape of approximately 5 mm, as suggested in a previous study [87]. This may imply that I_s flows through the filament bridging in the Bi-2223/Ag tape, as discussed for the results of Fig. 4.5. In addition, these results suggest that in Bi-2223/Ag tape, I_s is induced in smaller current loops compared to those in RE-system-coated conductors, such as GdBCO tapes. The analytical results in Fig. 4.6(b) and Table 4.1 also show the tendency of the smaller I_s loops to generate smaller magnetic fields. This result derives from the fact that in the case of a smaller loop, the maximum value of I_s becomes lower because of the smaller loop area and smaller E_s in 4.3.4. Consequently, I_s induced in Bi-2223/Ag tape with smaller loops due to the effect of the filament bridging has less effect on the magnetic field distribution from the coil current than I_s in a coated conductor.

4.4.2 Effect of Sweep Rate and Temperature

We also conducted experiments and analyses with varying sweep rates and T, examples of which are shown in Fig. 4.7. The horizontal axis is I_{op} in Fig. 4.7(a) and time in Fig. 4.7(b). The modeling for both figures assumes l = 9 mm. In Fig. 4.7(a), with increasing sweep rate,

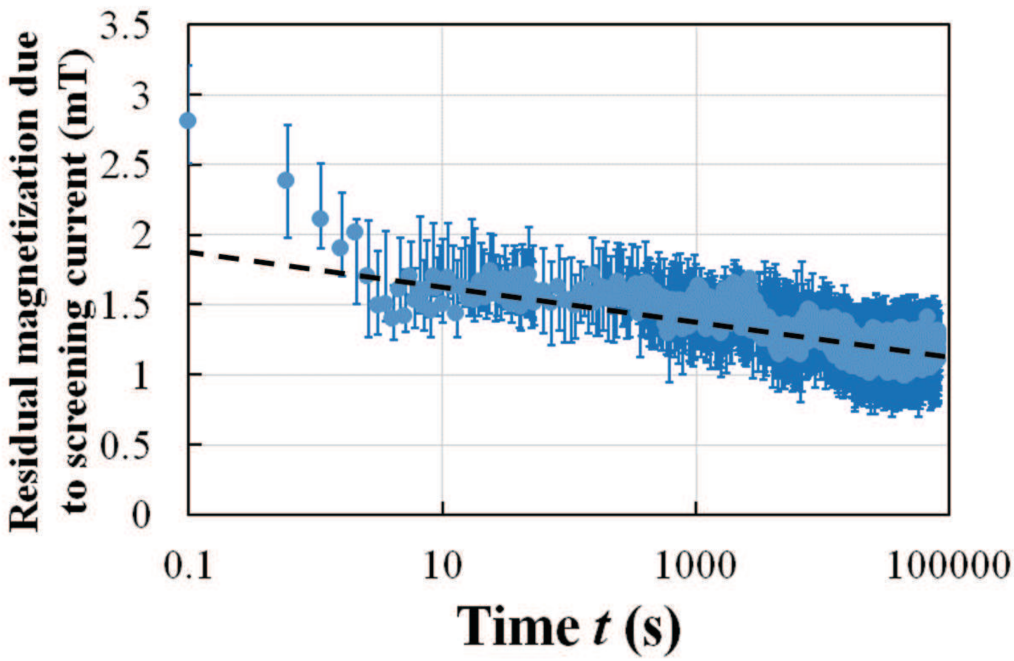

Figure 4.5: Semi-logarithmic plot of the temporal variation of the experimental residual magnetization at Hall sensor (I). I_{op} and T were 80 A and 50 K, respectively.

Table 4.1: Experimental result and modeling for the magnetization due to I_{s} for different values of l. $T = 50$ K, sweep rate = 40 A/min.

	Maximum value of the magnetization	Decay time Constant τ
Experiment	2.8 mT	0.6 - 1.0 s
Analysis (l = 5 mm)	2.5 mT	0.4 - 0.6 s
Analysis (l = 9 mm)	2.7 mT	0.7 - 0.9 s
Analysis (l = 50 mm)	4.2 mT	2.5 - 3.2 s
Analysis (l = 100 mm)	5.5 mT	5.0 - 6.3 s

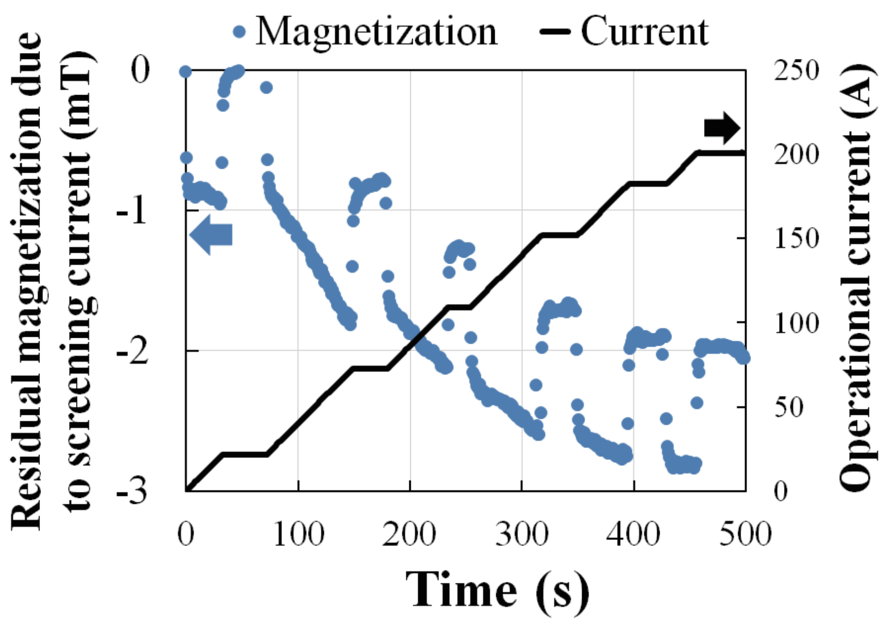

(a) I_{op} and residual magnetization with time

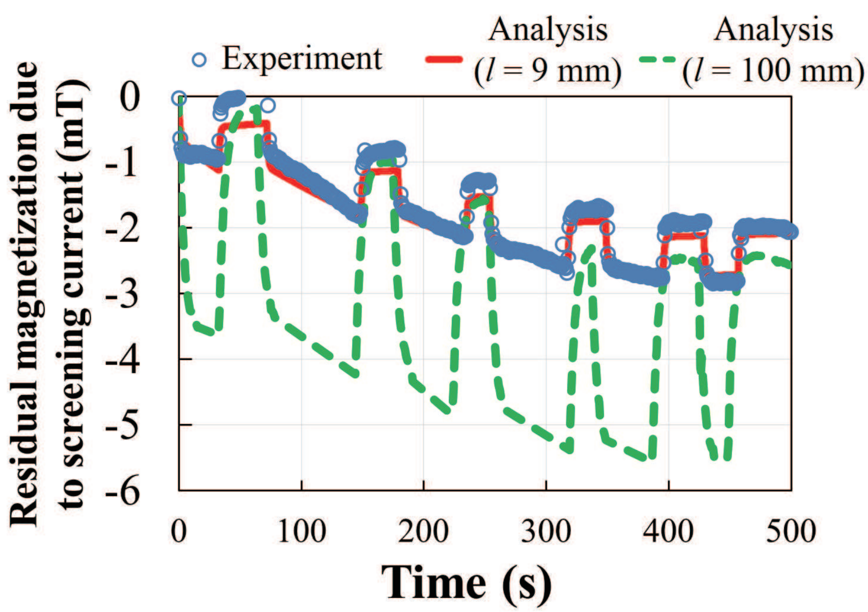

(b) Analysis fitting result

Figure 4.6: Temporal variations of (a) I_{op} and the magnetization generated by I_{s} at Hall sensor (I) and (b) fitting of the model for the magnetic field using two different values for l. T = 50 K, sweep rate = 40 A/min.

the temporal variation ratio of B_r and E_s increase, and as a result, the maximum value of the induced I_s increases according to eq. 4.3.4. In the case of Fig. 4.7(b), with a decrease in T,R_N of the silver sheath decreases [93], and as a result, the maximum value and time constant,$\tau = L_\mathrm{s}/R_\mathrm{N}$, of I_s increases according to eq. 4.3.4. These tendencies can be seen in the experimental results in Fig. 4.7 and can be modeled assuming $l = 9$ mm. This result indicates that the maximum value of I_s and its time constant in the Bi-2223/Ag coil are affected by the operational conditions of the coil and can be well described by the model.

4.4.3 Hysteresis Effect of the Magnetization Due to Screening Currents

As mentioned in section 4.2, we measured the hysteresis of the magnetic field generated by I_s, and investigated the maximum ratio of the induced magnetic field to that of the coil current itself. Figure 4.8 illustrates the experimental data and the modeling of the magnetization due to I_s at Hall sensors (I) and (II). The measured data are the solid circles, and the polarity of the hysteresis loops is dependent on the position of the sensor relative to the coil [89]. I_s in the coil tends to saturate at specific values in a higher load factor region due to the increasing resistance of the HTS tape, R_HTS. Since the sweep rate of 40 A/min, which corresponds to 46 mT/min at Hall sensor (I), is much higher than τ due to the flux creep, which is of the order of nT/min–μT/min, the decay effect due to flux creep is not detected in these hysteresis curves. The saturation values at the Hall sensors are (I) -2.85 mT and (II) 9.6 mT, which are only 1.2% and 1.8% of the magnetic field from I_op, respectively. The modeling of the hysteresis loops are depicted in Fig. 4.8 as lines. We used $l = 9$ mm, as estimated in the previous section, and $l = 100$ mm for I_s. As shown in the figures, the modeling assuming $l = 9$ mm agrees well with the experimental data. These results also support the validity of the developed model, and suggest that l for I_s in the Bi-2223/Ag coil can be assumed as approximately 9 mm, which agrees well with the bridging length of the filament in the Bi-2223/Ag tape. As also shown in Fig. 4.8, the saturation values of the magnetic field due to I_s greatly increase with the increasing loop length of I_s. This result indicates that the amount of the influence of I_s on the magnetic field generated by I_op depends on the loop length of I_s in the coil. Our model considering the loop length of I_s is surely helpful to estimate the effect of I_s on the magnetic field from I_op, which is directly related to the propulsive force of the magneto plasma sail. We will next enhance the model in order to clarify the effect of the loop length of I_s on AC loss in HTS coils for space applications. The developed model can also be applied to a coil made from RE-system-coated conductors. In this type of coil, a more complicated screening current will flow in the thin film superconducting area, and

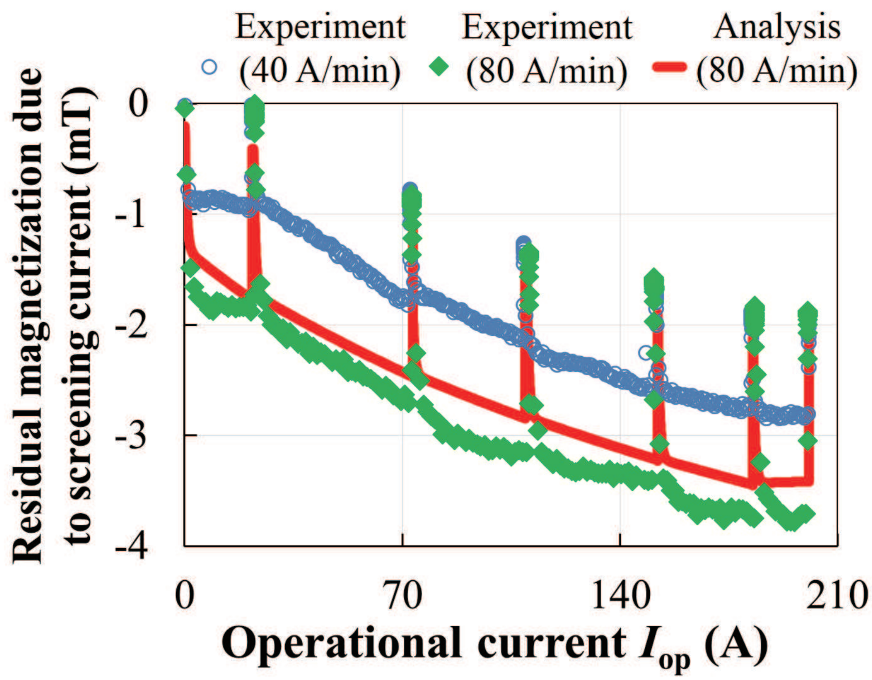

(a) For different sweep rates at $T = 50$ K

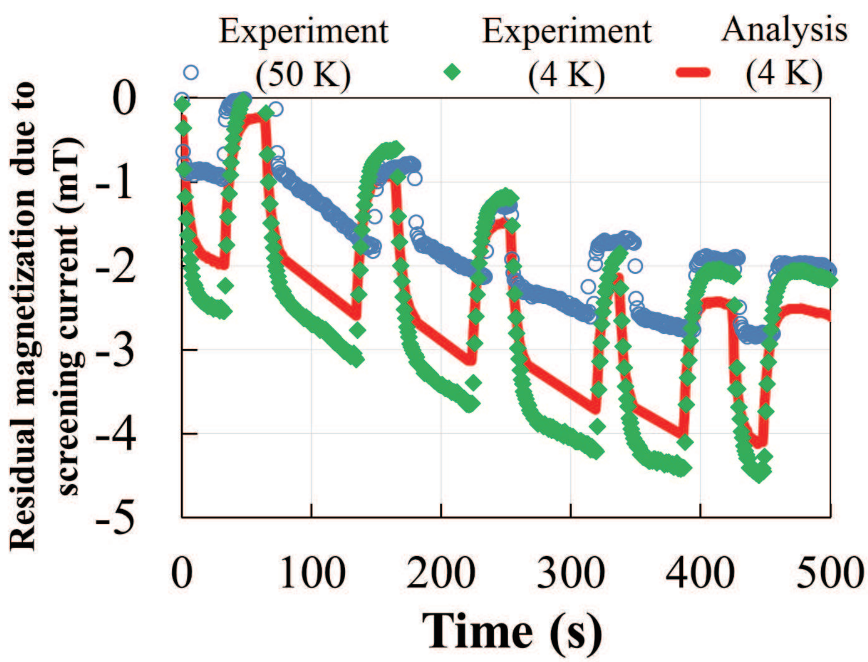

(b) For different T at sweep rate = 40 A/min

Figure 4.7: Temporal variations of the experimental and analytical results for the magnetic field generated by I_s at Hall sensor (I). The experimental and analytical conditions were (a) two different sweep rates of 40 and 80 A/min at $T = 50$ K and (b) two different temperatures, T, of 4 and 50 K for sweep rate 40 A/min.

the influence of such a current upon the residual magnetic field will be a focus of our future study.

4.5 Thermal Stability of HTS coil Under AC Ripple Current

4.5.1 AC Loss With AC Ripple Current in HTS Coil

We investigated the maximum electric field and effective AC loss generated by AC ripple currents with DC offsets, i.e., the loss characteristics in the HTS coil. We reported that the thermal stability of the coil depends on the maximum electric field in the coil in section 3.4.2. Figure 4.9 indicates the analysis results of the maximum electric field in a cycle, generated in the coil under DC currents with a variety of AC ripple components. The wave form of I_{op} applied to the scale-down model coil and the definition of I_{offset}, I_{ac}, and I_{peak} are depicted in Fig. 4.10. The DC currents of the horizontal axis are normalized by the critical current, I_{c}, and the frequency of the AC component is 10 Hz. As can be seen in Fig. 4.9, the AC component, I_{ac}, generates the electric field, E_{s}, in the coil according to the Faraday's law at lower DC currents, where the DC current without the AC component (solid line, E_0, in Fig. 4.9) does not. Such electric fields, E_{s}, from the AC currents can adversely affect the stable operation of the HTS coil at a lower load factor $I_{\mathrm{offset}}/I_{\mathrm{c}}$. On the other hand, it can be seen that, at a higher load factor, the electric field, E_0, caused by the flux-flow (solid line in Fig. 4.9) becomes dominant. Figure 4.9 also indicates that the higher I_{ac} generates the higher electric field, E_{s}, in the coil in case of the same I_{offset}. This is because the temporal variation of the self-magnetic field increases with the amplitude of the AC current I_{ac}. Figure 4.11 shows the analysis results of the effective AC loss per unit volume per cycle (AC loss density) in the HTS coil according to the amplitude of the AC current, I_{ac}, for various frequencies and DC offsets I_{offset}. The frequency of the ripple current is changed from 10 to 50 Hz. As shown in Fig. 4.11, the AC loss density is not much affected by the frequency of the ripple current. On the other hand, the AC loss density clearly increases with the amplitude of the AC current, I_{ac}, as is the case with the electric field E_{s}. The higher DC offset, I_{offset}, also generates the higher AC loss density even when I_{ac} is small. The effective AC loss density are not appeared while the peak value of the operational transport current density, J_{peak} ($I_{\mathrm{peak}} = I_{\mathrm{offset}} + I_{\mathrm{ac}}$), is below the minimum critical current density, J_{cm}, which is obtained by the percolation depinning model of eq. 4.3.2. This result is due to the superconducting property that the resistivity of the HTS tape, ρ_{HTS}, is almost zero while J_{peak} is below J_{cm}. On the other hand, the AC loss density rapidly increases when I_{peak} exceeds the critical

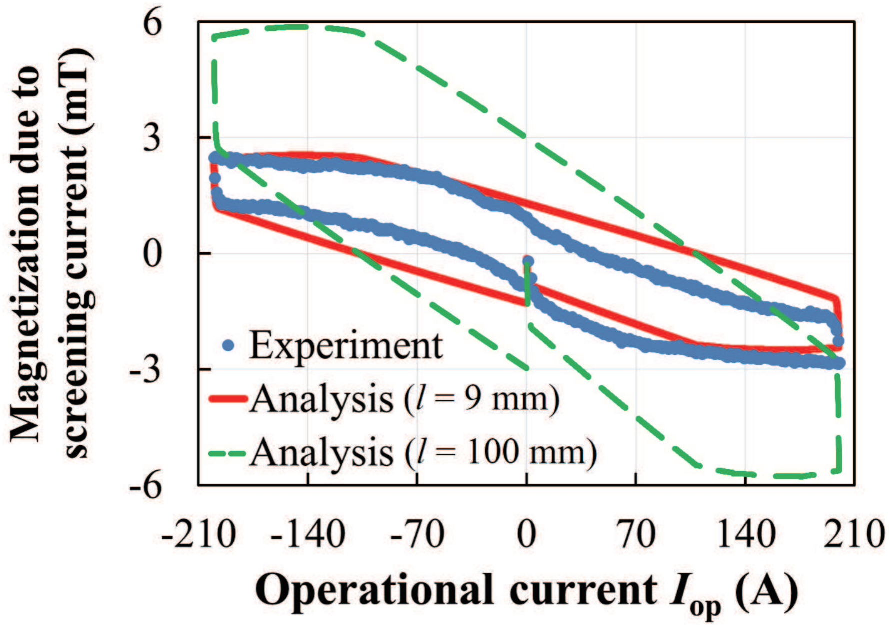

(a) Hall sensor (I)

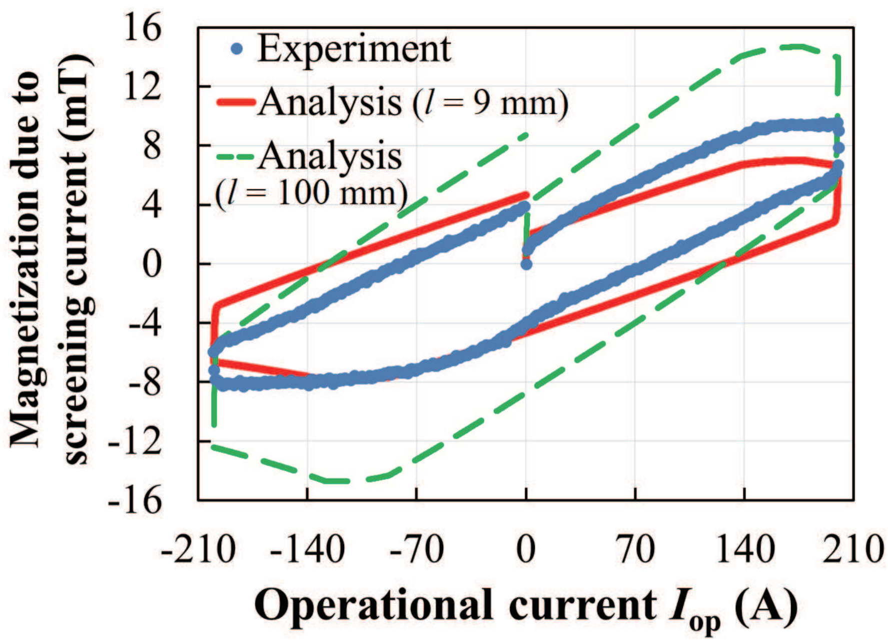

(b) Hall sensor (II)

Figure 4.8: Experimental and analytical results for the hysteresis of the magnetization due to I_s in the coil; sweep rate = 40 A/min and T = 50 K.

current, I_c (= 68 A), of the HTS coil because ρ_{HTS} greatly increases beyond the critical current. The obtained results suggest that I_{peak} of the ripple current determine the effective AC loss in the coil, and the DC offset strongly affects the AC loss characteristics in the HTS coil.

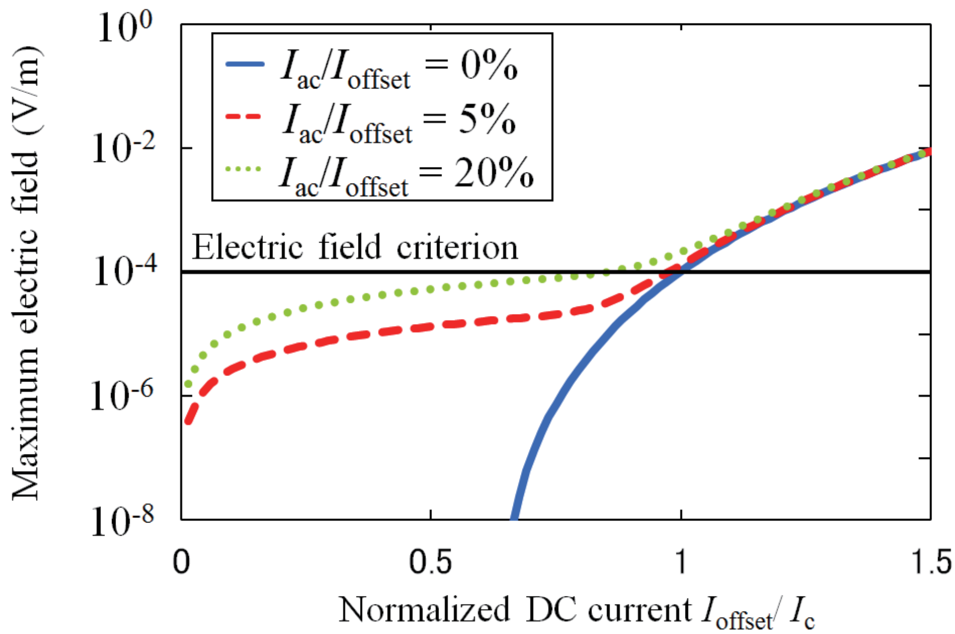

Figure 4.9: Maximum electric field in the Bi-2223/Ag coil under the various combination of the AC current, I_{ac}, and DC offsets I_{offset}. The operational temperature, T = 77 K, the critical current I_c = 68 A, and the frequency of $I_{ac}$is 10 Hz.

4.5.2 Effect of AC Loss With AC Ripple Current on Thermal Stability of HTS Coil

For practical operations, we analyzed the effect of the AC loss with the ripple current on the thermal stability of the HTS coil by solving the two-dimensional heat balance equation. Figure 4.12 shows the analysis results of the temporal evolution of the temperature rises, ΔT, on the top surface of the double-pancake coil during various ripple current applications. The frequency of the AC current is set to 10 Hz, and the amplitude, I_{ac}, are changed from 0 to 8 A in each I_{offset} (= 40, 55, 68 A). The conditions of each operation are described as Table 4.2.

As shown in Fig. 4.12(a), in the case of I_{offset} = 68 A (= I_c), the temperature of the coil diverges and the coil quench occurs even at I_{ac} = 0 A. The critical current, I_c, cannot be stably applied due to the cooling condition of the conduction cooling. On the other hand,

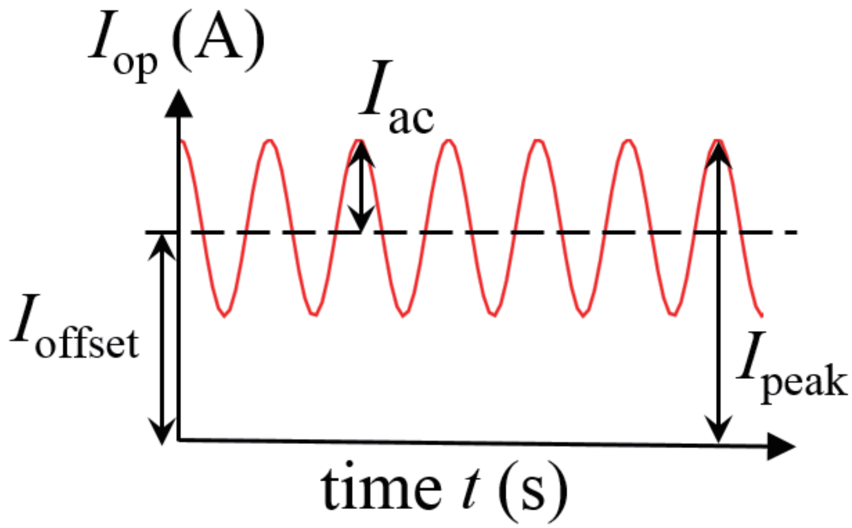

Figure 4.10: Definition of I_{offset}, I_{ac}, and I_{peak}.

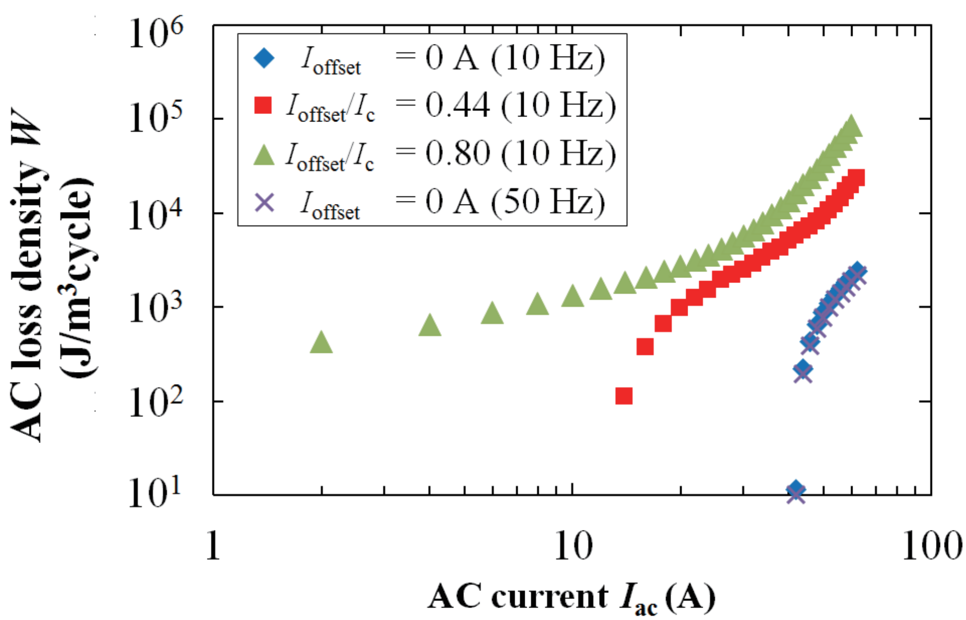

Figure 4.11: Dependence of the effective AC loss with the ripple current in the Bi-2223/Ag coil on I_{ac} and I_{offset}. The operational temperature T = 77 K and the critical current I_c = 68 A. DC offset are 0, 30 ($I_{offset}/I_c = 0.44$), and 55 A ($I_{offset}/I_c = 0.80$).

Table 4.2: Conditions of the operations of the coil in Fig. 4.12.

Fig. 4.12	Load factor $I_{\mathrm{offset}}/I_{\mathrm{c}}$	DC offset I_{offset}	Electric field in the coil
(a)	100%	68 A	$E_0 > E_{\mathrm{s}}$
(b)	80%	55 A	$E_{\mathrm{s}} > E_0$
(c)	59%	40 A	$E_{\mathrm{s}} >> E_0 \approx 0$

the coil temperature converges to a specified temperature when $I_{\mathrm{offset}}/I_{\mathrm{c}} = 0.80$ and $I_{\mathrm{ac}} = 0$ A in Fig. 4.12(b). The coil can be stably operated with the DC current at the load factor of 80% owing to the smaller electric field E_0. However, as shown in Fig. 4.12(b), the AC loss with I_{ac} drastically deteriorates the thermal stability of the HTS coil and brings about the coil quench, i.e., temperature of the coil diverges with I_{ac}. In the case of Fig. 4.12(c), although the AC loss of the ripple current slightly increases the coil temperature, the large ripple current has an insignificant effect on the thermal stability of the HTS coil. This is because the HTS tapes are not in the flux-flow state in the case of Fig. 4.12(c) (E_0 and $\rho_{\mathrm{HTS}} \approx 0$), and most of the AC power are consumed as a reactive power even though the electric field, E_{s}, is generated. These results suggest that, when the load factor $I_{\mathrm{offset}}/I_{\mathrm{c}}$ is high as much as HTS tapes in the coil are in the flux-flow state, i.e., $J_{\mathrm{peak}} > J_{\mathrm{cm}}$, the ripple current adversely affects the thermal stability of the coil. On the other hand, at a lower load factor such as 60%, the ripple current is not a big matter. Consequently, I_{offset} greatly influences the AC loss characteristics in the HTS coil, and the operational load factor $I_{\mathrm{offset}}/I_{\mathrm{c}}$ must be properly selected in order to apply the AC ripple current to HTS coils. The appropriate load factor for the operation depends on the cooling characteristics and condition of HTS coils.

4.6 Summary

To characterize and design optimal HTS coils for space missions, we developed a numerical analysis method based on the percolation depinning and the flux creep models, considering screening currents, I_{s}, induced in the coil. In this study, I_{s} induced in a Bi-2223/Ag double pancake coil was investigated and modeled. We measured the decay behavior of the magnetic field due to I_{s}, and then modeled the results assuming an equivalent loop length, l, for I_{s} in the coil. The experimental and analytical results suggest that the decay behavior of I_{s} in the Bi-2223/Ag tape was dominated by the silver sheath resistance and the flux creep, especially at a lower load factor. In addition, the experimental results under varying conditions could be quantitatively modeled assuming an equivalent l of approximately 9 mm for I_{s} in the coil. The good agreement between the measurements and the analyses proved the validity of our model, which considered the effects of the flux flow and flux creep on I_{s} induced in the HTS

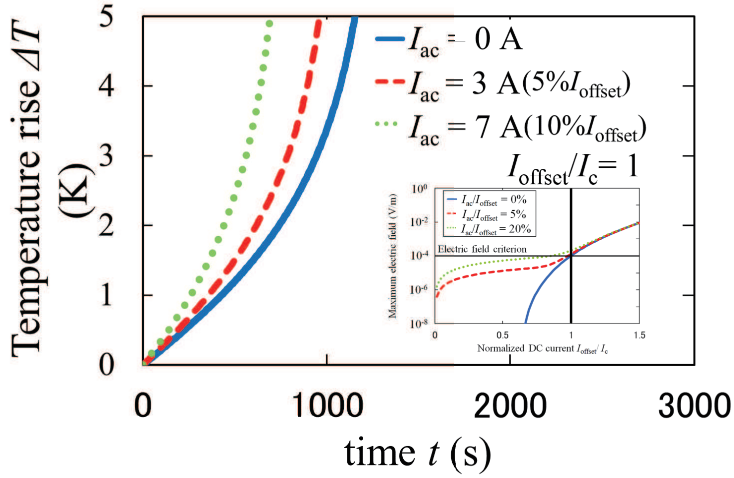

(a)

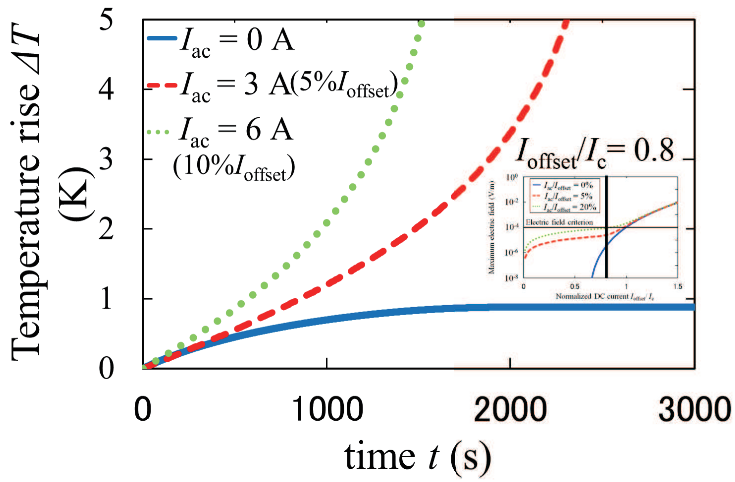

(b)

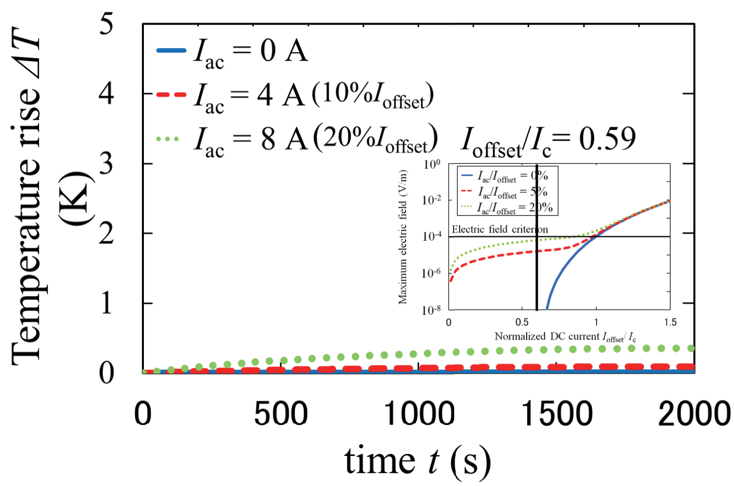

(c)

Figure 4.12: Time transient of the temperature rises, ΔT, on the top surface of the Bi-2223/Ag double-pancake coil during the various ripple current applications. The temperature rises at the middle layer on the upper surface of the coil, at which the maximum electric field is generated, are plotted. (a) I_{offset} = 68 A, (b) I_{offset} = 55 A, and (c) I_{offset} = 40 A. The operational temperature, T, is 77 K and the frequency of I_{ac} is 10 Hz.

coil. The precise identification of the mechanism for the smaller loops of I_s is our future work. To use DC/DC converters as a power supply and design a light-weight HTS coil system for space missions, we also investigated the effects of the transport AC losses under various ripple currents with DC offsets on the conduction-cooled coil performance. The developed analysis method can estimate the effective AC loss in HTS coils. Our analysis results implied that the AC loss with the ripple current deteriorated the thermal stability of a conduction-cooled coil when HTS tapes in the coil are in the flux-flow state, e.g., the load factor (operational current/critical current) of 80%. However, at a lower load factor, most of the AC power were consumed as a reactive power and the ripple current cannot be a serious problem for the thermal stability of the conduction-cooled coil. These results suggest that, if the operational load factor is properly selected by the developed analysis code, the light-weight power supply system including an AC ripple current can be used for the HTS coil spacecraft system.

Chapter 5

Conceptual Design of HTS Coil for Magneto Plasma Sail

5.1 Introduction

The propulsive force of the magneto plasma sail is proportional to the magnetic moment, μ, of the coil. The magnetic moment, μ, of circular coils can be expressed as

$$\mu = \sum_{t=1}^{N} I \pi r_t^2, \tag{5.1.1}$$

where N denotes the total turn number of the coil, I is the operational transport current, and r_{t} is the radius at each turn t ($1 \leq t \leq N$) of the coil.

The purpose of the study is to use HTS conductors to realize a magnetomotive force at $NI = 10^6 - 10^7$ A-turns under the size limitation of the spacecraft ($r_{\mathrm{t}} \leq 2.0$ m). The HTS coil must be designed with a larger magnetic moment and higher thermal stability without the use of any refrigerants. As is well known, Yttrium Barium Copper Oxide (YBCO)–coated conductors (CCs) possess high mechanical strength against electromagnetic forces such as hoop stress. Since the magneto plasma sail requires a large-sized coil with a diameter of approximately 4 m, the hoop stress in the coil becomes a serious constraint on the design of the coil. YBCO CCs are expected to be utilized in larger-sized coils than in the case of Bi-2223/Ag, owing to the high tolerance of the Hastelloy® substrates. In this study, HTS coils using YBCO CCs as well as Bi-2223/Ag tapes are conceptually designed for the magneto plasma sail. For the magneto plasma sail, the magnetic moment, μ, must be as large as possible; for example, $\mu = 1.2 \times 10^7$ to 1.2×10^8 $\mathrm{A \cdot m^{-2}}$ and $10^6 - 10^7$ A-turns with a diameter of 4 m will suffice. In addition, the above-mentioned thermal stability and electromagnetic force should be considered to avoid coil quenches and the degradation of superconducting properties in space. In this chapter, we analyze the current transport performance, thermal stability, and experienced stresses of HTS coils, on the basis of the developed analysis model, i.e., a electromagnetic field as well as thermal analysis. A suitable configuration of the coil is searched to increase the magnetic moment, μ, of the coil, based on the constraint conditions of the maximum electric field, hoop stress, transverse compressive stress, total heat generation, and thermal stability of the coils.

5.2 Design Conditions

The Bi-2223/Ag tape used for the coil design is the same as the tape used for the scale-down model coil in the previous chapters 3.1. The YBCO CC applied to the coil is 3.0 mm in width and 0.1 mm in thickness, which is additionally reinforced against mechanical strain with Hastelloy® substrates (0.05 mm in thickness). The longitudinal variation in the local critical currents of the YBCO CCs is not taken into account in this study. Figure 5.1 illustrates a schematic diagram of the designed coil and the definitions of the variables, as well as the x–y direction used in the analysis. We now analyze the distribution of the magnetic field vector, electric field, heat generation, and heat transfer in the cross section of the coil described in Figure 5.1, by means of the developed thermo-electromagnetic field analysis based on the percolation depinning model. Since the coil is cooled by radiation in outer space, the Dirichlet condition (constant temperature T_{op}) was set at the top, bottom, and outer surfaces of the coil and the Adiabatic condition on the inner surface. As the sensitivity analysis, the optimal outside radius, r_{o}, the number of layers, m, and stack, n, of the coil are searched in order to maximize its magnetic moment of eq. 5.1.1 with the constraint conditions described below:

1. Operational temperature T_{op} is set to 20 K.

2. Total length and weight of the CCs are constant, approximately 50 km and 200 kg, because of the mass limit for the spacecraft.

3. Coil size is limited to $\phi 4 \times 7$ m (outside diameter $2r_o \times$ height), due to the installation size limitation in the rocket for launch.

4. The MAXIMUM electric field in the coil does not exceed 1 $\mu\mathrm{Vcm}^{-1}$. This definition is equivalent to evaluating the minimum critical current I_{cmin} in the coil in order to avoid coil quenches [95].

We also examined the total heat generation in the coil for the thermal behavior of the coil taking into account the cooling capacity, and also the hoop stress, which is calculated as $B_y \times J \times r_\mathrm{t}$ at each turn t [96], and transverse compressive stress applied to the coil for considering the strength of stresses that the HTS can tolerate in terms of mechanical strength [97]-[99]. The optimal configuration of the coil is searched by evaluating the magnetic moment of eq.5.1.1 in the case of $I = I_\mathrm{cmin}$ and the above-mentioned parameters on each coil design.

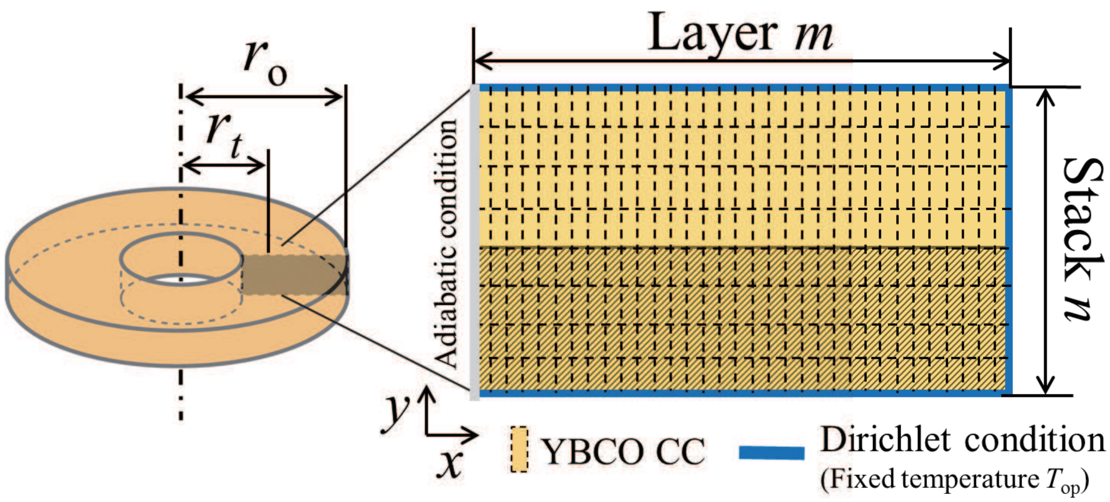

Figure 5.1: Schematic diagram of a cross section of designed coils. (r_o: outside radius, r_t: radius at each turn t, m: layer number, n: stack number).

5.3 Sensitivity Study

5.3.1 YBCO Coil

Figure 5.2 shows the analysis results of the magnetic moments of the coil according to its configuration. The total length of the CCs is constant. As can be seen in Fig. 5.2, the magnetic moment clearly increases with the outside radius r_o. This is because the magnetic moment is proportional to the square of the radius (see eq. 5.1.1). In addition, the magnetic moment is larger with a greater stack number n, or, in other words, a lower layer number m, with the condition that the outside radius, r_o, stays the same.

Figure 5.3 indicates the effect of the stack number, n, in the case of $r_\mathrm{o} = 2.0$ m, on (a) the critical current and the magnetic moment of the coil, and (b) the maximum hoop stress and transverse compressive stress applied to the coil. As can be seen in Fig. 5.3(a), the critical current I_cmin increases with a very high or very low stack number. Higher critical currents

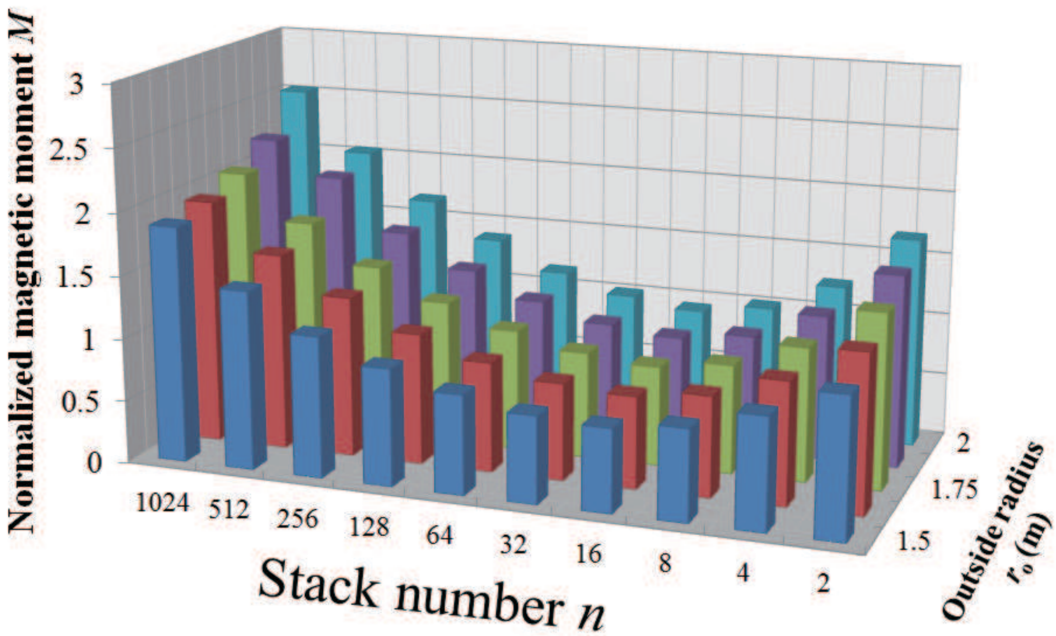

Figure 5.2: Dependence of the magnetic moment on the configuration of the coil. The total length of the CCs is constant. The magnetic moment is normalized by $\mu = 1.2 \times 10^7$ A $\cdot$ m^2, which is the minimum requirement for the magneto plasma sail (10^6 A-turns with an outside radius r_o of 2 m).

Table 5.1: Specifications of the coils shown in Fig. 5.3.

	(a) Coil (I)	(b) Coil (II)	(c) Coil (III)
Outside radius r_o	2.0 m	2.0 m	2.0 m
Stack number n	4	16	512
Layer number m	1050	252	8
Weight	200 kg	200 kg	200 kg
Critical current I_{cmin}	325 A	236 A	493 A
Magnetomotive force NI_{cmin}	1.4×10^6 A-turns	0.95×10^6 A-turns	2.0×10^6 A-turns
Total heat generation	56 W	7.4 W	1.0 W
Maximum hoop stress	5.4 GPa	4.4 GPa	0.78 GPa
Maximum transverse compressive stress	5.9 MPa	23 MPa	150 MPa

make the magnetic moment much larger. The critical current tends to decrease when the aspect ratio of the cross section of the coil approaches 1:1 (in the case of $n = 15$).

This fact can be understood further from Figs. 5.5 and 5.6. These figures show the distribution of the magnetic flux density, B, and the perpendicular magnetic flux density, B_x, respectively, perpendicular to the tape's broad surface, in the cross section of the coil. Only the lower half of the coil cross section, (the shaded area in Fig. 5.1) is described due to the symmetry of the electromagnetic field. The corresponding coils (I)–(III) are shown in Fig. 5.3 and Table 5.1. Illustrations of the shape of coil (II) and coil (III) are also depicted in Fig. 5.4. As can be seen in Figs. 5.5 and 5.6, the magnetic flux density, especially B_x, in coils (I) and (III) is smaller than that in coil (II) (in the case of a cross-sectional aspect ratio ≈1:1). Critical currents in the highly perpendicular magnetic field region are greatly decreased because of the magnetic field dependency of the E–J curve of the HTS tapes. Larger critical currents can be produced in the case of high or low stack numbers, as shown in Fig. 5.3(a), due to smaller stray magnetic fields.

Fig. 5.3(b) and Table 5.1 also indicate that, as the stack number increases, the maximum hoop stress decreases and the transverse compressive stress increases monotonically. This is because the hoop stress ($B_y \times J \times r_t$) is proportional to B_y, parallel to the tape's broad surface, which decreases as the stack number increases, as shown in Fig. 5.5. The transverse compressive stress also increases with the decreasing top and bottom surface areas of the coil, i.e., with decreasing layer number m. The broken lines in Fig. 5.3(b) indicate the upper limit for the YBCO CCs. Hence, the shaded area shown in Fig. 5.3(b) indicates the configurations that satisfy the constraint condition for the applied stresses. The other configurations in the case of $r_o = 2.0$ m cannot be realized in terms of the mechanical strength.

Figs. 5.7 and 5.8 show the thermal behavior of the coils. Specifically, Fig. 5.7shows the heat generation density and Fig. 5.8 shows the temperature distributions. As can be seen

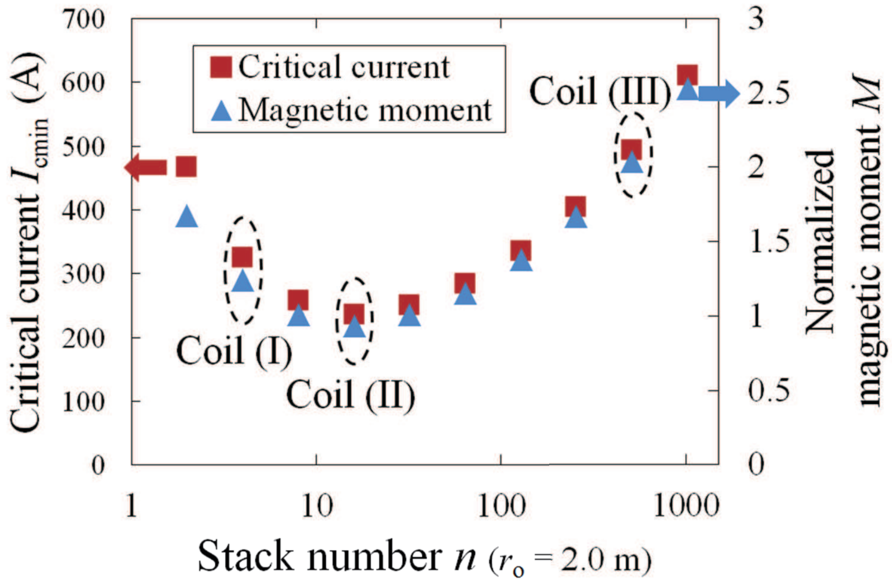

(a) Critical current and Magnetic moment

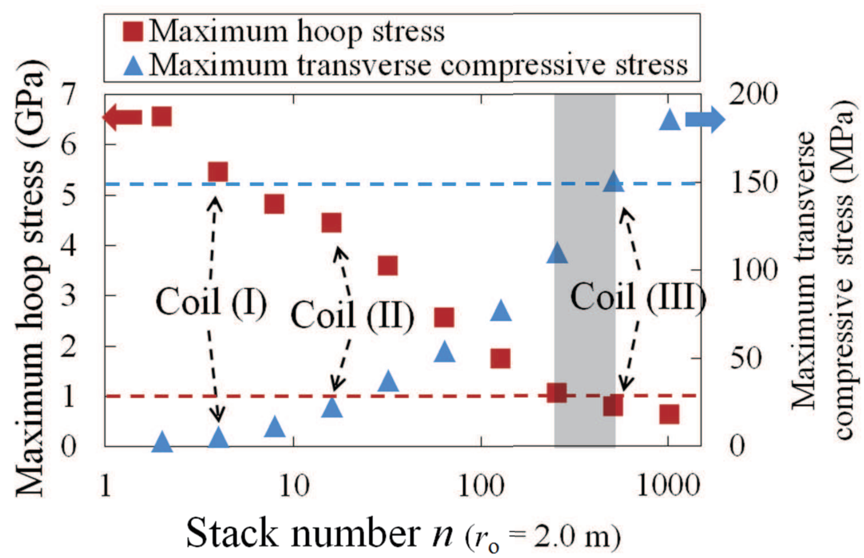

(b) Maximum Hoop stress and Transverse compressive stress

Figure 5.3: Dependence on the stack number of (a) critical current and magnetic moment and (b) maximum hoop stress and transverse compressive stress, in the case of an outside radius of $r_o = 2.0$ m. The total length of the CCs is constant. The maximum hoop stress is located at the middle stack in the innermost layer. Specifications of the coil (I)–(III) are shown in Table I. The broken lines in (b) indicate the limited stresses allowed for the YBCO CCs [97]-[99].

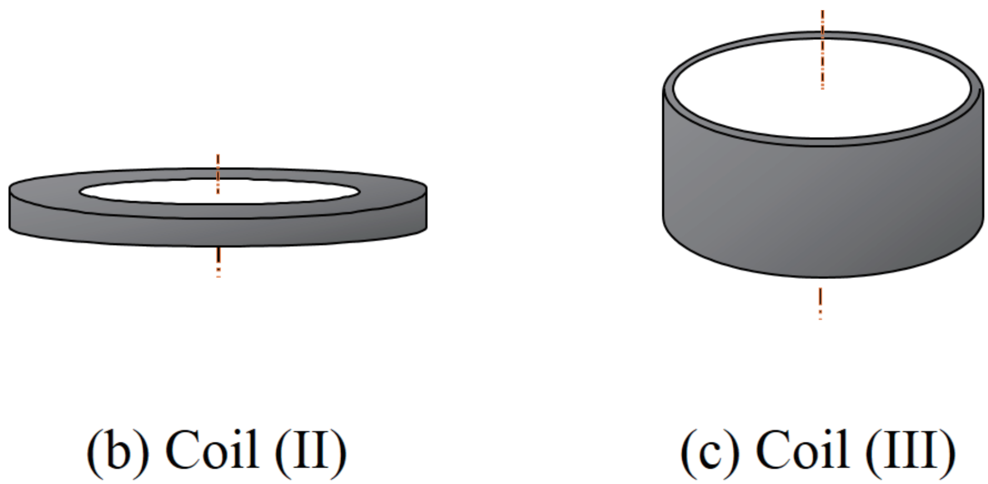

(b) coil (II)

Figure 5.4: Illustrations of the shape of coil (II) and coil (III).

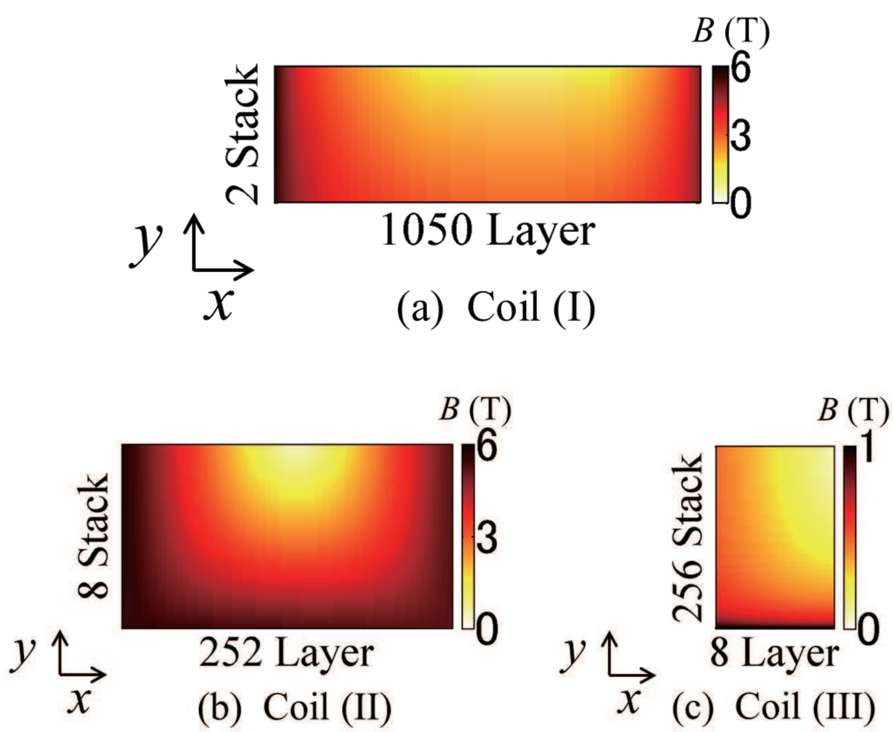

Figure 5.5: Magnetic flux density, B, distribution in the coils at $T_{\mathrm{op}} = 20$ K, $I = I_{\mathrm{cmin}}$ (maximum values (a) 5.62 T, (b) 5.75 T, and (c) 1.31 T).

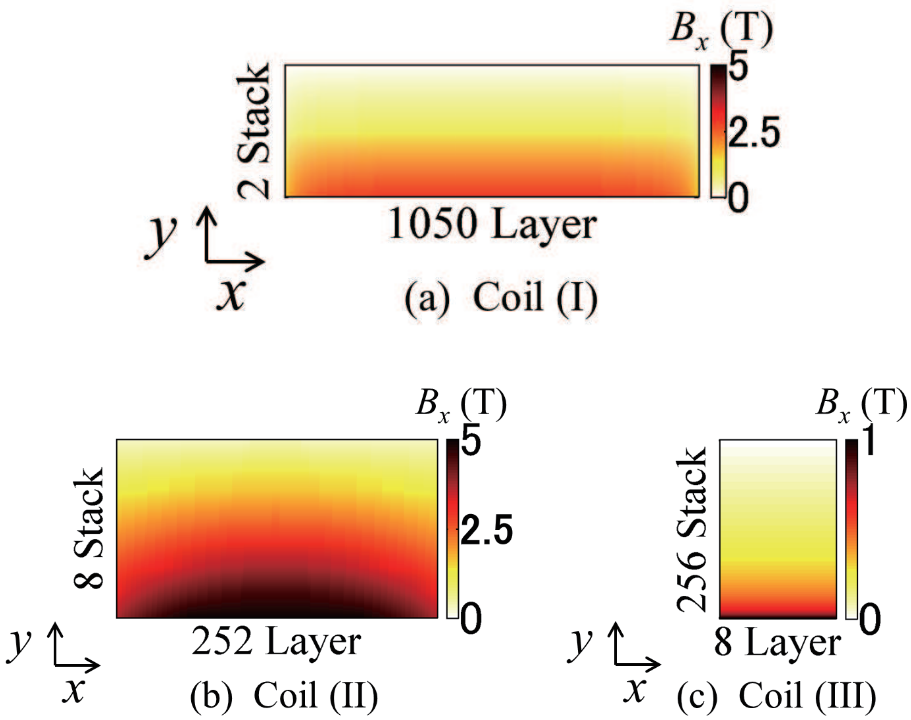

Figure 5.6: Perpendicular magnetic flux density, B_x, distribution in the coils at $T_{\mathrm{op}} = 20$ K, $I = I_{\mathrm{cmin}}$ (maximum values (a) 2.88 T, (b) 5.33 T, and (c) 1.26 T).

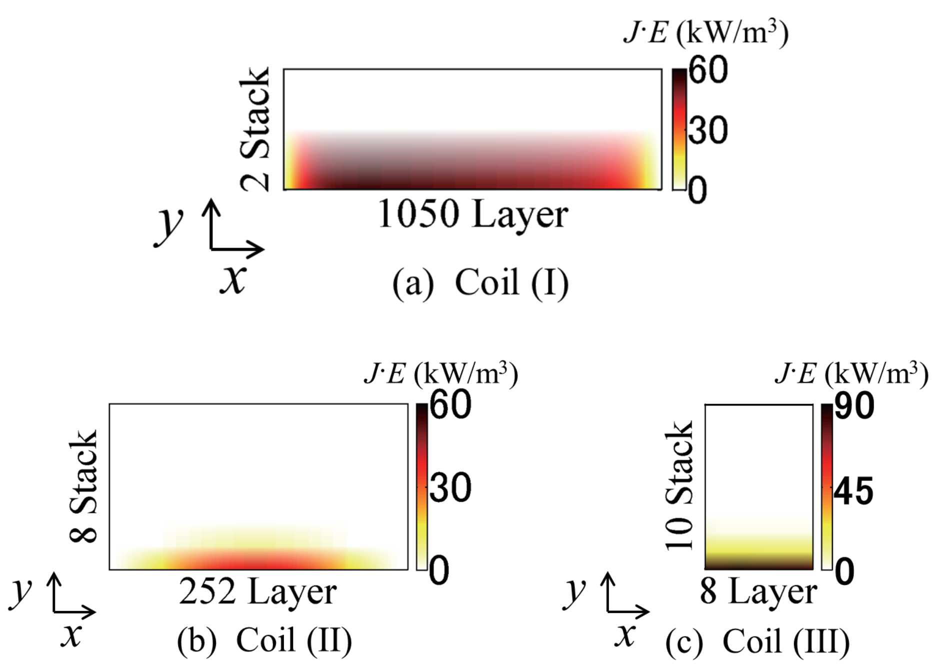

Figure 5.7: Heat generation density, $J \cdot E$, distribution in the coils at $T_{\mathrm{op}} = 20$ K, $I = I_{\mathrm{cmin}}$ (maximum values (a) 54.5 kWm^{-3}, (b) 39.7 kWm^{-3}, and (c) 85.8 kWm^{-3}).

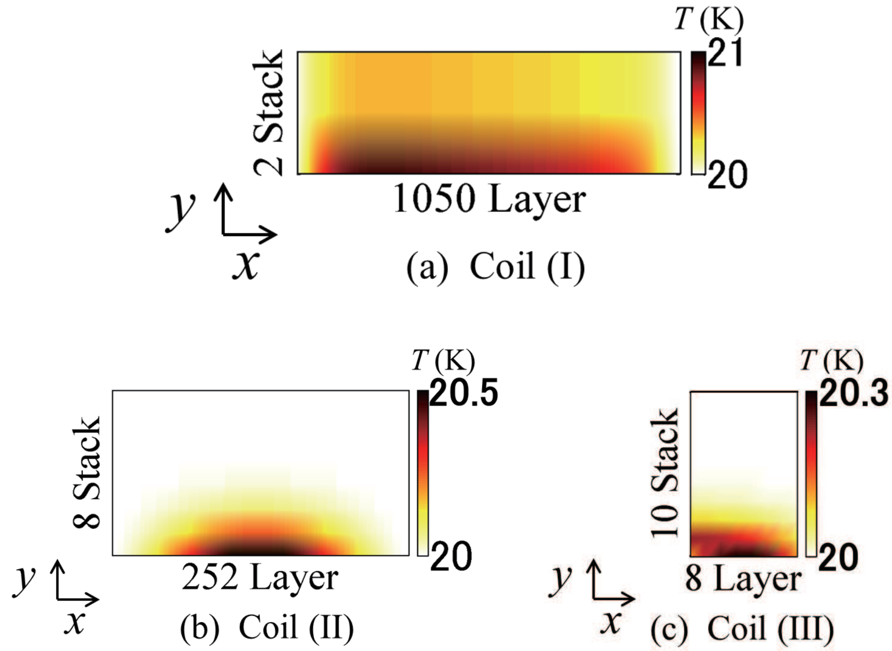

Figure 5.8: Temperature, T, distribution in the coils at $T_{\mathrm{op}} = 20$ K, $I = I_{\mathrm{cmin}}$, $t = 60$ s (maximum values (a) 20.9 K, (b) 20.5 K, and (c) 20.3 K).

in these figures, the maximum heat generation and temperature rise are located near the middle turn on the bottom stack in the coil due to the perpendicular magnetic flux density B_x being strongest in this area. As can also be seen in Fig. 5.8, temperature rise in coil (III) is smaller than that in coils (I) and (II), despite the larger heat generation density depicted in Fig. 5.7. This is because the cooling surface area of the coil increases due to the so-called flat-wise winding of the coil. Table 5.1 also shows that total heat generation in the coil decreases with the increasing stack number n because the area of the flux flow state decreases as shown in Fig. 5.7. These results suggest that thermal stability of the coil can be improved by increasing the number of the stack, n.

From these analysis results, coil (III) achieves the magnetomotive force NI at 2.0×10^6 A-turns with a diameter of 4 m and is the suitable configuration for obtaining the maximum magnetic moment at 2.5×10^7 A $\cdot$ m^2 under the conditions of this study. Consequently, we can conclude that a thin-walled coil with a larger diameter, i.e., large r_{o}, high n, and low m, such as coil (III), is the suitable design for obtaining larger magnetic moments with higher thermal stability and lower hoop stress. However, the transverse compressive stress becomes much larger and must be taken into account for such coil design.

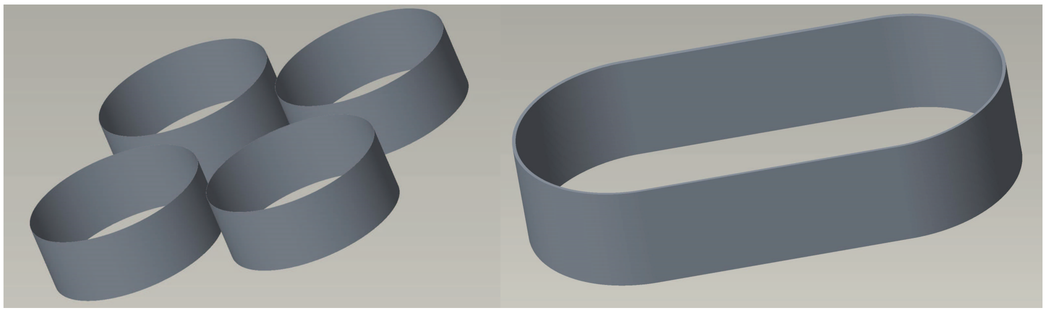

(a) (b)

Figure 5.9: Illustration of the shape of (a) multi-pole and (b) racetrack coil.

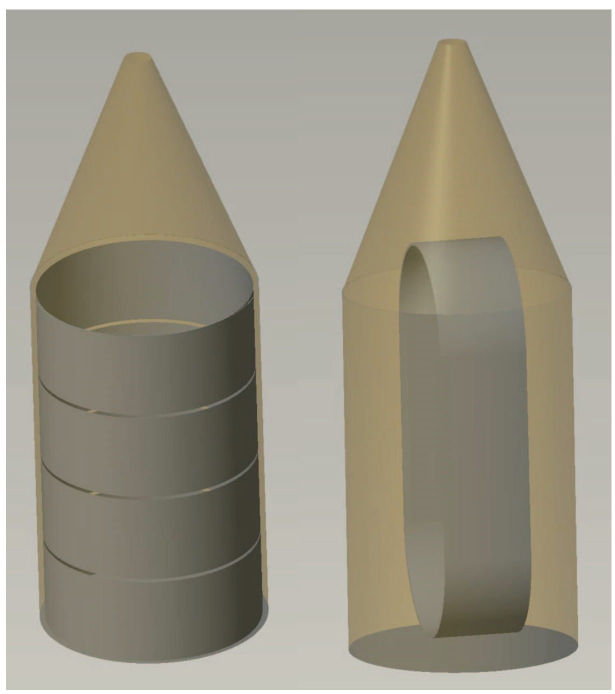

(a) (b)

Figure 5.10: Illustration of the on-board (a) multi-pole and (b) racetrack coil.

5.3.2 Bi-2223/Ag, Multi-pole and Racetrack Coil

The same analysis was performed with Bi-2223/Ag circular coils as well as additional two kinds of coil configurations; i.e., multi-pole, and racetrack coil using YBCO CCs, as shown in Fig. 5.9. The multi-pole coil consists of more than one coil (Fig. 5.9(a)). The racetrack coil is the coil with the shape of the racetrack geometry (Fig. 5.9(b)). The multi-pole coil and racetrack coil are loaded into the rocket as shown in Fig. 5.10. The multi-pole coil needs to be deployed in space after the launch. The suitable coil configuration to maximize the magnetic moment was searched under the constraint conditions described below:

1. Operational temperature T_{op} is set to 20 K.

2. Total weight of the HTS tapes are constant, approximately 200 kg, because of the mass limit for the spacecraft.

Due to the installation size limitation in the rocket for launch, the coil size is limited as;

1. For circular coil, coil diameter $2r_o$= 4 m. The height of the coil is limited to 7 m.

2. For multi-pole coil, the coil number is 4. Each coil diameter $2r_o$= 4 m. The height of each coil is limited to 1.6 m.

3. For racetrack coil, the coil size is limited to 4 m $\times$ 7 m (minor (shorter) diameter $\times$ major (longer) diameter).

In the present analysis, the maximum magnetic moment was defined if one of the constraint conditions described below is satisfied:

1. The temperature of the coil diverges and coil quench occurs on the basis of the developed thermal analysis.

2. For the Bi-2223/Ag coil, Hoop stress or transverse compressive stress exceeds 470 MPa or 70 MPa, respectively [100].

3. For the YBCO coils, Hoop stress or transverse compressive stress exceeds 1 GPa or 150 MPa, respectively [97]-[99].

Figure 5.11 indicates the dependence of the maximum magnetic moment of the coil on the stack number, n, for each coil configuration. Table 5.2 shows the configurations of each coil type for obtaining the maximum magnetic moment under the constraint conditions. The magnetic moment is normalized by $\mu = 1.2 \times 10^7$ A $\cdot$ m^2, which is the minimum requirement for the magneto plasma sail (10^6 A-turns circular coil with an outside radius r_{o} of 2 m). As can be seen in Fig. 5.11, for all kinds of the coils, the magnetic moment clearly increases with a higher stack number n, or, in other words, a lower layer number m, i.e. a coil with a thin-wall. This is because the critical current I_c increases with a very high stack number thanks to smaller stray magnetic fields as mentioned in the previous section. On the other hand, at a lower stack number n, the magnetic moments become smaller than that of thin-walled coils because, for the coils with a large diameter, the hoop stresses become much larger than the limited value in the case of coils with a lower stack number, n, as shown in Fig. 5.3(b), and the large currents can not be applied to such coils due to the mechanical strength of the HTS.

When the Bi-2223/Ag circular coil is compared to the YBCO circular coil, the magnetic moment of the Bi-2223/Ag coil is much lower than that of the YBCO circular coil. This is mainly because the stress tolerance and current transport characteristics in a high magnetic field of the Bi-2223/Ag coil are inferior to those of the YBCO coil, although the Bi-2223/Ag coil is superior to the YBCO coil in terms of the cooling characteristics. However, we assumed the YBCO CCs with uniform characteristics along with the length of the CCs, although the long length of YBCO CCs with high homogeneity in the local critical currents are now difficult to be available. The making process of the YBCO CCs is expected to be matured.

As can also be seen in Fig. 5.11 and Table 5.2, when the YBCO multi-pole and racetrack coil are compared to the YBCO circular coil, the magnetic moment of the multi-pole and racetrack coil is higher than that of the circular coil in most cases. Using a multi-pole or racetrack coil geometry, the total turn number of the coil can be smaller than that of the circular coil as shown in Table 5.2 with the condition that the total length of the CCs stays almost the same. The magnetic flux density in each coil tape becomes smaller thanks to a lower neighboring turn number. For this reason, the larger current can be applied to the multi-pole and racetrack coil if the same length of the CCs is used due to the magnetic field dependency of the E–J curve of the HTS tapes. This study reveals that the YBCO multi-pole or racetrack coil can realize the magnetic moment which is approximate three times larger than the minimum requirements for the magneto plasma sail, which corresponds to the thrust of 0.5 mN approximately according to the previous study [53]. Note that, however, the multi-pole coil is required to deploy the coils in space and needs a complex structure to support the multi-coil, and also the racetrack coil occupies a larger area than a circular coil in the rocket for launch.

We also investigated the required weight of the coil to obtain the minimum requirement of the magnetic moment (10^6 A-turns circular coil with an outside radius r_o of 2 m) at a variety of operational temperature, T_{op}, in the case of the racetrack coil using the YBCO CCs. Figure 5.12 shows the dependence of the required weight of the coil to obtain the

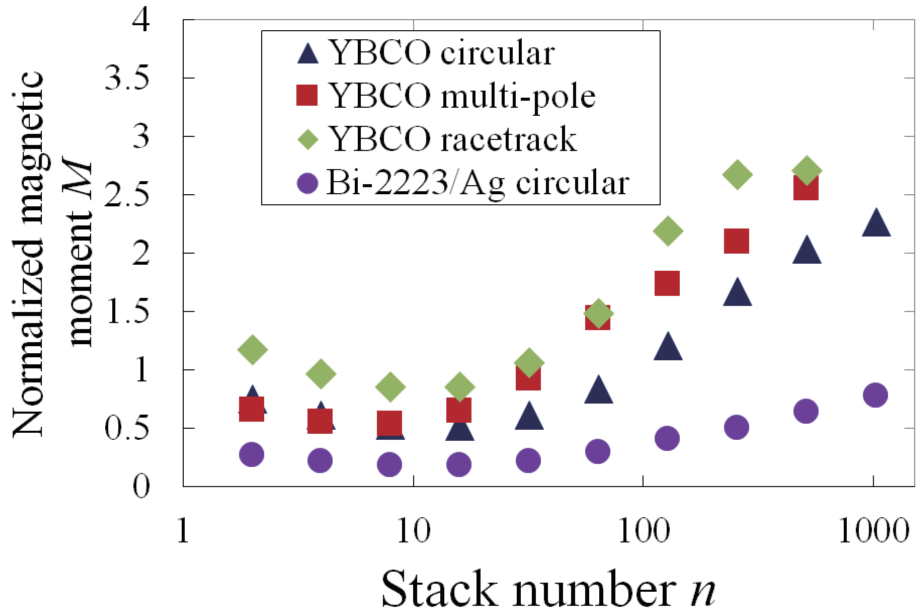

Figure 5.11: Dependence on the stack number of the magnetic moment of the coils in the case of an outside radius of $r_o = 2.0$ m. The total length of the Bi-2223/Ag tape or YBCO CCs is constant.

Table 5.2: Coil configurations to obtain the maximum magnetic moment.

	Bi-2223/Ag circular	YBCO circular	YBCO multi-pole	YBCO racetrack
Outside radius r_o	2.0 m	2.0 m	2.0 m	1.7 m×3.5 m
Stack number n	1024	1024	512	512
Layer number m	2	4	2	6
Total turn number N	2048	4096	1024	3072
Operational current	374 A	547 A	616 A	535 A
Magnetomotive force NI_{op} (A-turns)	0.8×10^6	2.2×10^6	2.5×10^6	1.6×10^6
Normalized magnetic moment	0.8	2.2	2.5	2.7
Maximum hoop stress	130 MPa	380 MPa	260 MPa	380 MPa
Maximum transverse compressive stress	70 MPa	150 MPa	120 MPa	140 MPa

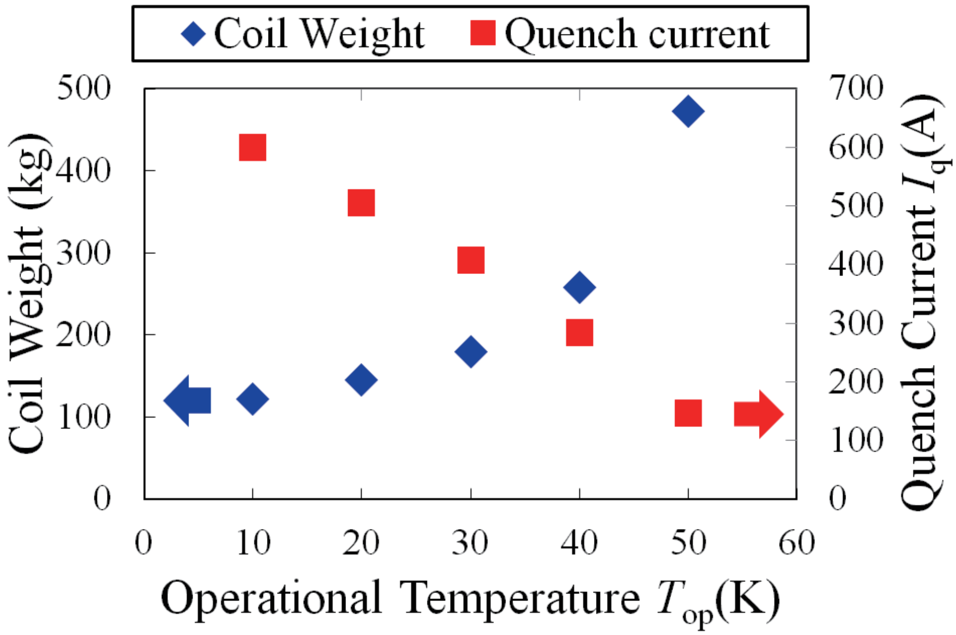

Figure 5.12: Dependence on the operational temperature, T_{op}, of the required weight of the YBCO racetrack coil to obtain the minimum requirement of the magnetic moment for the magneto plasma sail.

minimum requirement of the magnetic moment for the magneto plasma sail as well as the quench current on the operational temperature, T_{op}, of the coil. As can be seen in Fig. 5.12, the required weight of the coil increases with the operational temperature, T_{op} because the quench current which causes the coil quench drastically decreases with T_{op}as shown in Fig. 5.12 due to the temperature dependency of the E–J curve of the HTS tapes. Considering the mass limit of the spacecraft, the weight of the coil should be less than 200 kg. Based on this analysis result, therefore, the operational temperature of the on-board coil should be less than 30 K to satisfy the requirement of the magnetic moment for the magneto plasma sail.

The present analysis makes a rough design of the HTS coil for the magneto plasma sail without taking into account the cooling structure to cool down each coil configuration. More precise optimization of the HTS coil considering the cooling structure of the HTS coil to maximize the magnetic moment to mass ratio of the system, i.e., acceleration of the spacecraft, is required to consider the practical use of the magneto plasma sail.

5.4 Summary

An HTS coil with a larger magnetic moment using YBCO coated conductors and Bi-2223/Ag tape was designed for a magneto plasma sail. For the coil design, we analyzed the current transport properties, thermal behavior, and applied stresses of the HTS coils, and compared these characteristics for each coil configuration. This analysis method made use of $E-J$ characteristics according to the percolation depinning model. As a sensitivity analysis, it was revealed that a thin-walled coil with a larger diameter can generate a larger magnetic moment with higher thermal stability and lower hoop stress. However, transverse compressive stress becomes a serious constraint factor for such a thin-walled coil design. We also analyzed with the racetrack and multi-pole coil configurations as well as a Bi-2223/Ag circular coil to obtain a larger magnetic moment. From a point of view of maximizing the magnetic moment for the spacecraft, the racetrack and multi-pole coil is more suitable configuration than a circular coil and the magnetic moment can be increased to approximate three times larger than the minimum requirement for the magneto plasma sail. The present study also investigated the required weight of the coil to obtain the minimum requirement of the magnetic moment at a variety of operational temperature in the case of the racetrack coil using the YBCO CCs. According to the analysis result, the operational temperature of the magnetic sail drive coil should be less than 30 K to meet the requirement of the magnetic moment for the magneto plasma sail, considering the mass limit of the spacecraft.

Chapter 6

HTS Coil System for Magneto Plasma Sail

6.1 Introduction

In the previous chapter, we clarified the configuration of the on-board HTS coil to improve the magnetic moment and thrust of the magneto plasma sail under the condition of the mass limitation of the coil. For the practical use of the magneto plasma sail, however, the total mass of the HTS coil system is strictly limited for space missions as the weight of the system directly affects the acceleration or performance of the propulsion system. The optimization of the HTS coil considering the total mass of the system, e.g., cooling structure according to the configuration of the HTS coil, is required to maximize the magnetic moment to mass ratio or acceleration, of the magneto plasma sail. If we use some refrigerants to cool down the on-board HTS coil, a large amount of the liquid helium or nitrogen are required to be loaded for a long-term space missions because the heat invasion from the sun light gradually evaporates such refrigerants. Thus, the cooling system using the refrigerants weighs too much and cannot be applied for deep space explorations. This study aims to develop a light-weight HTS coil system with the use of radiation and/or conduction cooling which utilizes 3 K background temperature in space. The temperature of the on-board coil, however, becomes higher than the background temperature 3 K due to the heat invasion from the sun light, coil support structures, and current leads under the radiation cooling condition. The radiation cooling system must be also optimized to keep the HTS coil at the desired operational temperature and, at the same time, minimize the weight of the cooling system. In this chapter, we optimize the HTS coil system including the radiation cooling structure to obtain the maximum magnetic moment to mass ratio for the magneto plasma sail.

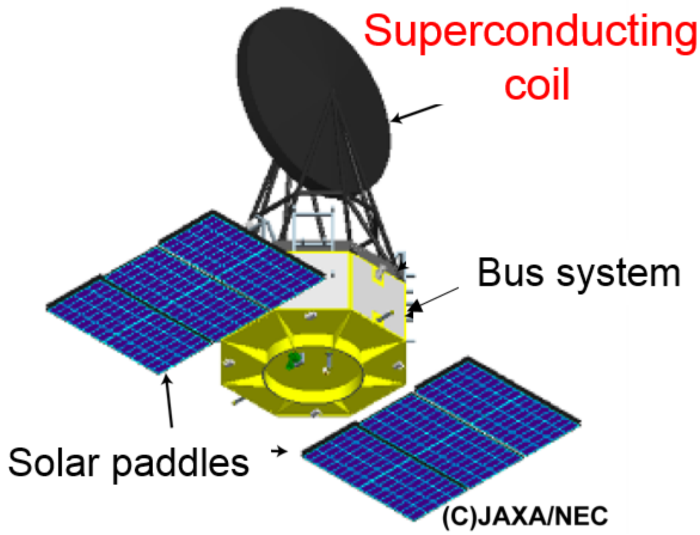

Figure 6.1: Illustration of the magneto plasma sail proposed by JAXA/NEC.

Table 6.1: Weight distribution of the subsystems of the magneto plasma sail.

Mass Limit		860 kg
Mission	Plasma Sources	30.8 kg
Bus System	Structure	210 kg
	Communication	16.6 kg
	Data Handling	10.6 kg
	Attitude Control	23.5 kg
	Reaction Control	22.2 kg
	Wire Harness	30.0 kg
	Magnetic Shielding	10.0 kg
Fuel	N2H4	15.0 kg
	Xe	5 kg-50.0 kg
Total Weight	Dry	376 kg
Except for HTS Coil System	Wet	396 kg - 441 kg
HTS Coil System	HTS coil, Cooling System, and Power Supply System	419 kg - 464 kg

6.2 Overview of HTS coil system

An illustration of the system configuration of the magneto plasma sail proposed by JAXA/NEC is shown in Fig. 6.1. The solar paddles generate the electric power to use for the excitation of the HTS coil as well as the operation of subsystems in the bus module. The spacecraft bus module contains a power supply system as well as an attitude control and telecommunication system. Table 6.1 shows the weight distribution of the subsystems of the magneto plasma sail for the exploration to the planet Jupiter. The magneto plasma sail is considered to be launched by H-IIA202 and the total weight of the spacecraft should be less than 860 kg considering the launch capacity of the rocket. The magneto plasma sail requires plasma sources and some fuel (Xe : 5 kg -50 kg, the required amount depends on the way of the operation of the plasma sources) to inject plasma from the spacecraft and expand the coil magnetic field while a pure magnetic sail does not require any fuels. The electric power generated by solar paddles is inversely proportional to the square of the distance from the Sun. The basic configuration of the solar paddles for the magneto plasma sail consists of five layers which can be deployed in two stages and produce the electric power of 850 W at 2.5 AU used to mainly excite the HTS coil and 370 W at 5 AU around the Jupiter used for the operation of the bus system. A magnetic shielding system is also installed to protect instruments (and crews) in the spacecraft from the strong magnetic filed produced by the on-board HTS coil itself. One of the methods of the magnetic shielding for the magneto plasma sail using Meissner effect of superconductors is discussed in Appendix A. To use ferromagnetic materials such as a Permalloy for the magnetic shielding can also be considered for the magneto plasma sail. The direction of the magnetic axis of the on-board coil is, in this study, set to the perpendicular as well as parallel direction to the sun direction (or solar wind) as shown in Fig. 6.2, on the other hand, some study reported that the direction of the magnetic axis should be perpendicular direction to the solar wind in terms of the attitude stability [40]. Figure 6.3 indicates the boundary conditions of the developed thermal analysis for the perpendicular or parallel direction of the magnetic axis, respectively. In the perpendicular direction, the thermal input due to the thermal invasion from the sunlight and current leads is applied to the side surface of the coil. The coil is cooled down via the top and bottom surface of the coil (Dirichlet condition) by radiation to the outer space. On the other hand, in the parallel direction, the thermal input is applied to the bottom surface of the coil, and the coil is cooled down from the top and side surface of the coil by radiation.

To reduce the total weight of the system and obtain the maximum magnetic moment to mass ratio of the magneto plasma sail, we considered the dependency of the weight of the HTS coil system on the configuration of the HTS coil and operational coil temperature. The

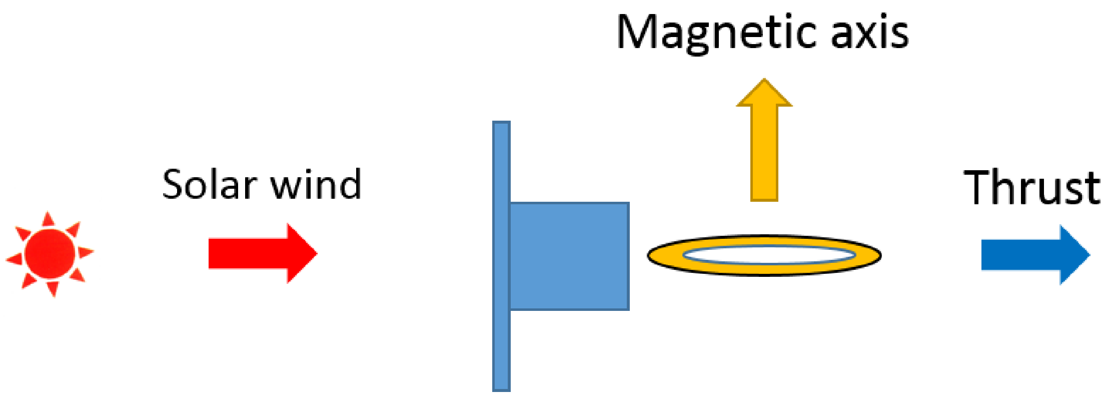

(a) Perpendicular direction to the sun direction

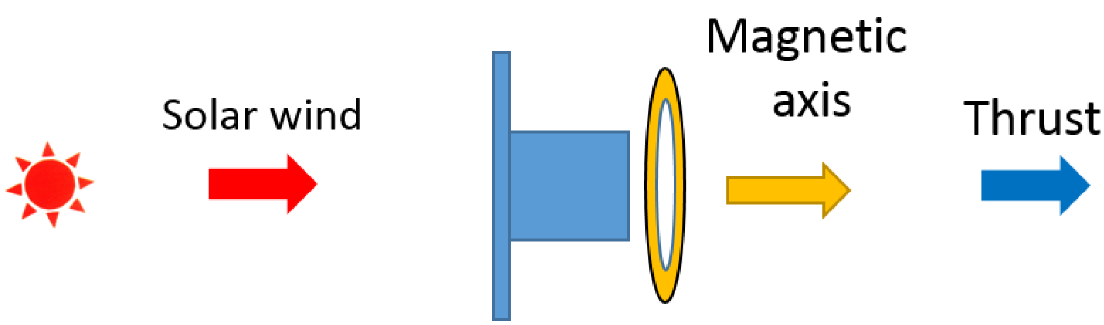

(b) Parallel direction to the sun direction

Figure 6.2: Direction of the magnetic axis of the coil to the sun direction.

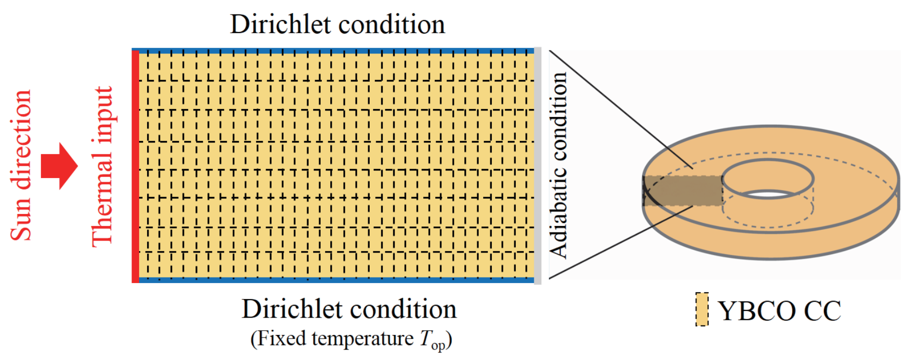

(a) Perpendicular direction to the sun direction

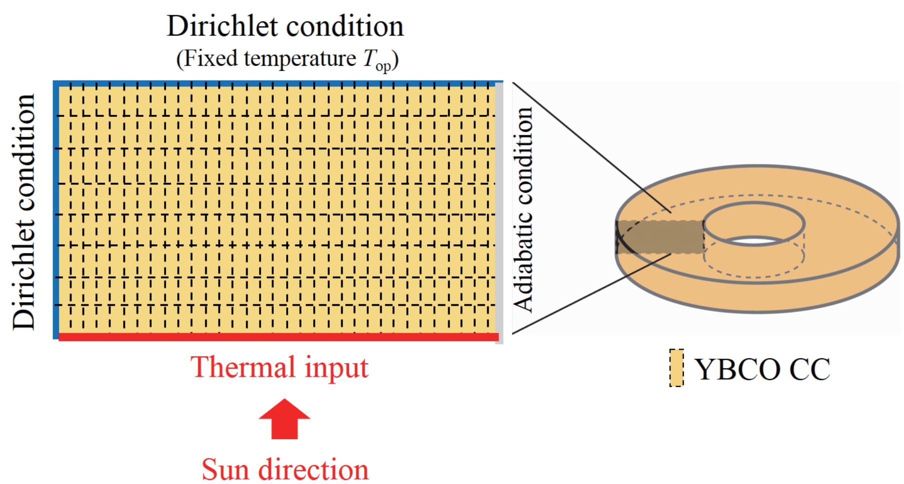

(b) Parallel direction to the sun direction

Figure 6.3: The boundary conditions of the thermal analysis for the perpendicular and parallel direction.

total weight of the system for the magneto plasma sail can be described as follows:

$$M_{\mathrm{system}} = M_{\mathrm{coil}} + M_{\mathrm{cool}} + M_{\mathrm{power}} + M_{\mathrm{others}} \tag{6.2.1}$$

where M_{system}, M_{coil}, M_{cool}, M_{power}, and M_{others}denote the weight of the system, HTS coil, cooling system, power system, and other subsystems of the magneto plasma sail, respectively. M_{others} in this study is set to 396 kg according to Table 6.1. The required mass of the power system has been also obtained as shown in Fig. 6.4 [75]. In fact, the mass of the structure depends on the coil configuration and weight, such dependency was ignored in this study for the simplicity.

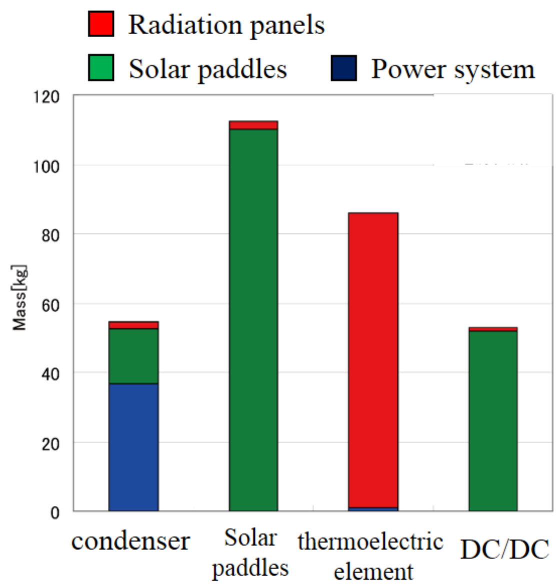

Figure 6.4: The mass of the system for a variety of the power system [75].

6.3 Thermal Design of Cooling System

As mentioned in section 5.3, the on-board HTS coil of the magneto plasma sail should be cooled down to less than 30 K to realize the minimum requirements of the magnetic moment for space missions. Figure 6.5 shows a schematic diagram and CAD model of the HTS coil system of the magneto plasma sail in the case of the parallel direction of the magnetic axis. The cooling system for the HTS coil consists of multi-layer of radiation panels, Multi-Layer Insulation (MLI), and coil cooling case for the HTS coil, that prevent the heat invasion which cannot be blocked only by the sun shield. Only the side surface of the panels was used for the radiation cooling to the outer space. Due to the mass limitation, any refrigerants will not be used for the magneto plasma sail. The HTS coil is installed at the opposite side from the sun light, surrounded by the radiation panels and coil cooling case as shown in Fig. 6.5. The coil is thermally connected with the bus module via current leads and coil support materials which will be cooled down by thermal anchors to the radiation panels. The heat invasions to the HTS coil are also came from the heat generation in the current leads as well as the sun light which is not prevented by the radiation panels. The configuration of the radiation panels and coil case were designed according to the configuration of the coil in order to cool the coil down to the desired operational temperature of around 10-50 K. The cooling system also depends on the operational current of the HTS coil because the heat generation and heat invasion to the HTS coil from the current leads depend on the operational current. We assumed the following condition for the thermal design of the cooling system.

1. Thermal input of the solar heat to the surface of the spacecraft is 1350 W/m^2.
2. The temperature of the bus module is 300 K.
3. The coil is cooled down to 10-50 K by radiation cooling using radiation panels.
4. The background temperature of space is 3 K.
5. The radiation factor of the radiation panels are 0.82.
6. The spacecraft is at thermal equilibrium in interplanetary space.

The factors of the heat transfers in the spacecraft are described in Fig. 6.6. The amount of the radiation heat between two materials (material with the temperature,T_2, surface area, A_2, radiation factor ε_2 to material with the temperature,T_1, surface area, A_1, radiation factor ε_1) was calculated as

$$Q = \frac{\sigma_{SB}}{\frac{1}{\varepsilon_2} + \frac{1}{\varepsilon_1} - 1} A_2 (T_2^4 - T_1^4) \tag{6.3.1}$$

ε_1=1 was used for the radiation factor of deep space as a perfectly black body. The weight of the radiation panels (Aluminum alloy 2.70 g/cm^3, thickness: 0.2 mm) can be obtained by evaluating the required surface area, A_2, of the panels to cool down the coil to the desired operational temperature. The heat invasion by the heat transfer from the support materials were calculated by the Fourier law as

$$Q = \frac{A}{L} \int_{T_1}^{T_2} \kappa dT \tag{6.3.2}$$

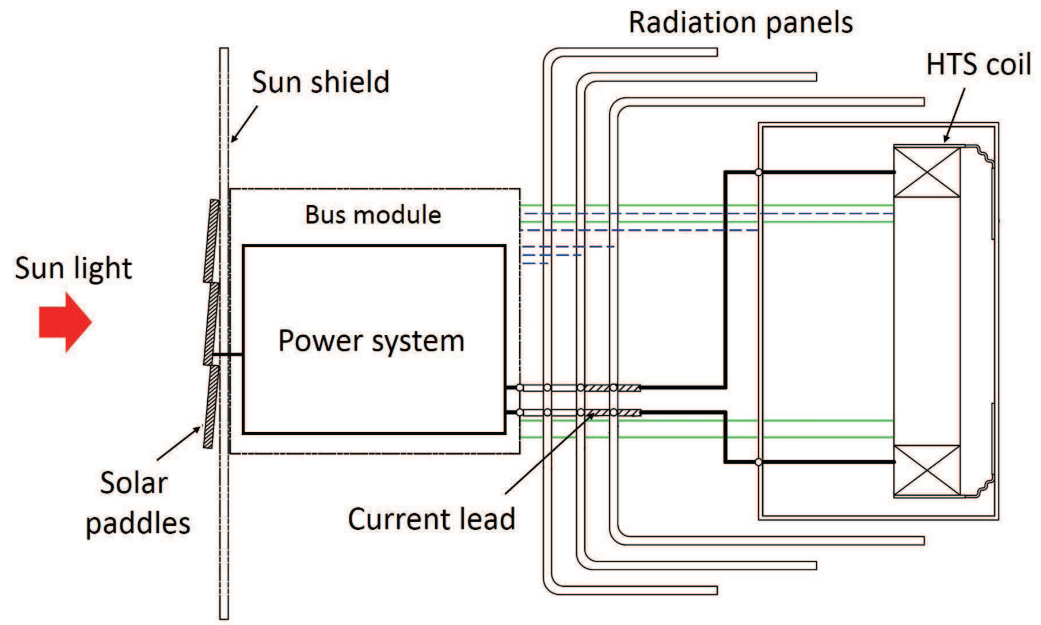

(a)

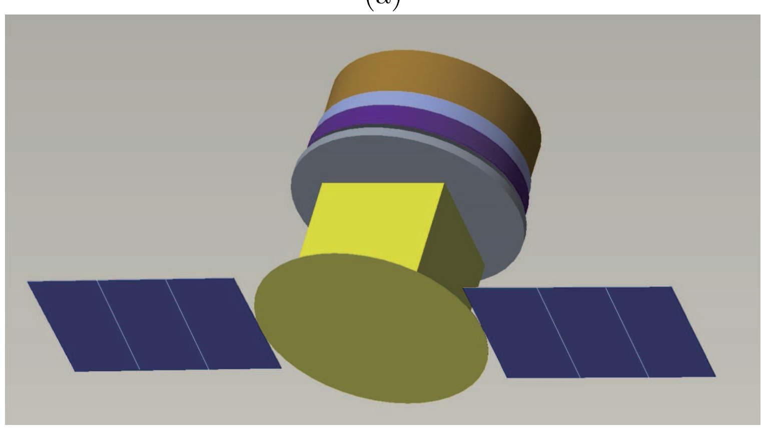

(b)

Figure 6.5: (a) Schematic diagram and (b) CAD model of the HTS coil system of the magneto plasma sail.

where A is the area of the cross section of the materials, κ is the thermal conductivity of the materials. The thermal conductivity, κ, of the Carbon-Fiber-Reinforced Polymer (CFRP) was used for the support structure of the HTS coil. The thermal invasion from the current leads can be calculated as

$$Q_{\min} = I\left(2\int_{T_c}^{T_h} \rho\kappa dT\right)^{\frac{1}{2}} \tag{6.3.3}$$

where I is the operational current and V is the voltage between both ends of the current lead. The thermal invasion, Q, from the current lead to the HTS coil corresponds to the heat generation in the current lead. We also assumed to use an HTS lead as the current lead between the two panels at the temperature below 77 K to reduce the heat invasion from the current lead to the HTS coil.

Figure 6.7 shows an example of the thermal block diagram of the HTS coil system, calculated by the above-mentioned equations. The temperature decrease by the effect of the cooling system is also shown in Fig. 6.8. The horizontal axis of Fig. 6.8 shows the distance from the Bus-module and HTS coil is located at 1.6 m from the bus-module. The cooling system was composed of four radiation panels. The operational current was 200 A and a YBCO circular coil with a diameter of 4 m and a weight of 200 kg was used. The coil can be cooled down to 20 K with such multi-layer of the radiation cooling structure although 0.0387 W was applied to a coil surface as the thermal invasion. In this case, the total surface area of the radiation panels was 106.5 m^2 and total mass of the cooling system was $M_{\text{cool}} = 108.7$ kg.

Figures 6.9 and 6.10 shows an example of the temperature distribution as well as the heat generation distribution at cross section of the coil in the both cases of the magnetic axis direction. Only a lower half of the coil is described because of the symmetry of the electromagnetic field and the side where the word 8 layer or 15 layer is written is the bottom surface of the coil. As can be seen in these figures, the coil temperature is increased mainly at the left side facing the sun direction due to the thermal invasion from the sunlight which is not prevented by the radiation panels. Also, in the case of the parallel direction, the temperature rise in the coil is larger than the perpendicular direction as shown in these figures. It can be explained by the local joule heat generation in the coil also described in Fig. 6.10. The joule heat is mainly generated around the bottom surface of the coil due to the magnetic field dependency of the superconducting property. And in the case of the parallel direction, the bottom surface of the coil is facing to the sun direction. This result suggests that the

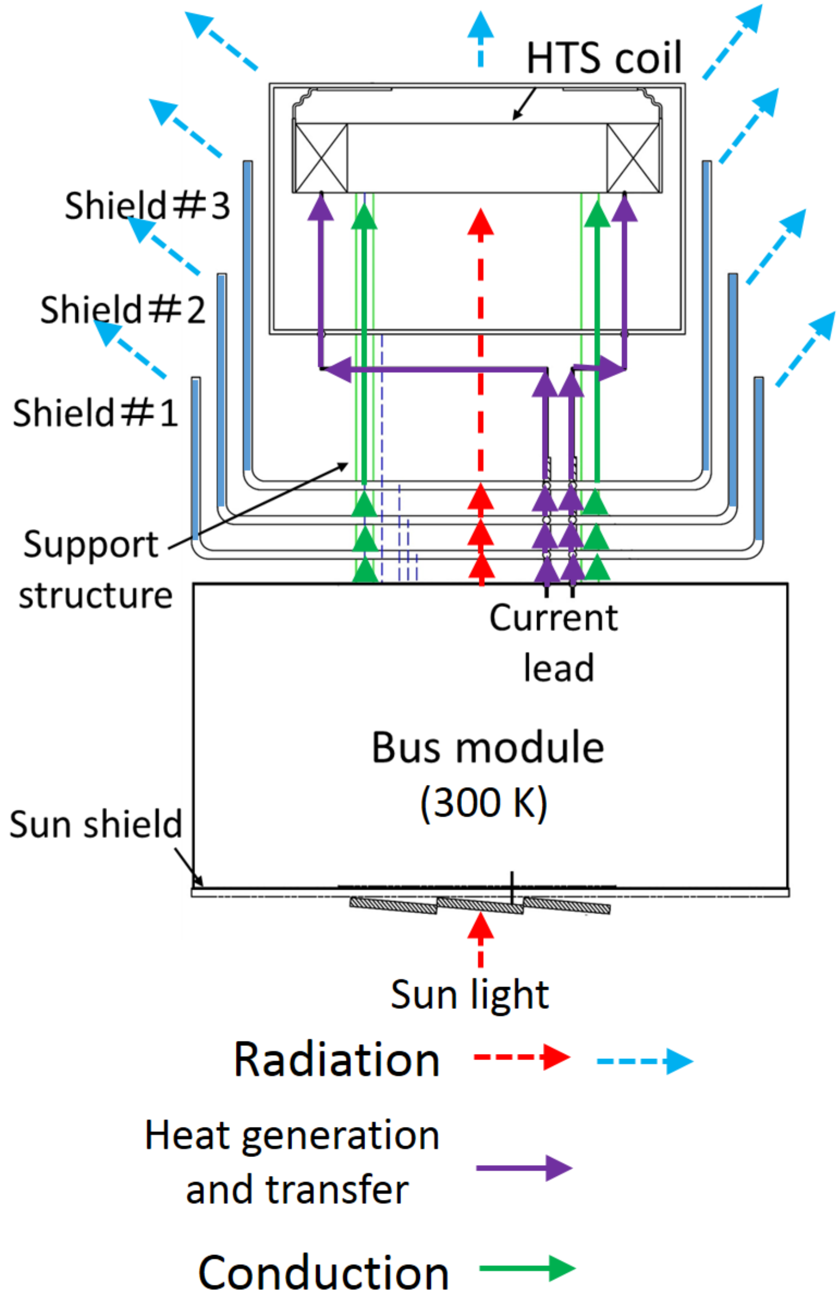

Figure 6.6: Thermal flow in the system of the magneto plasma sail.

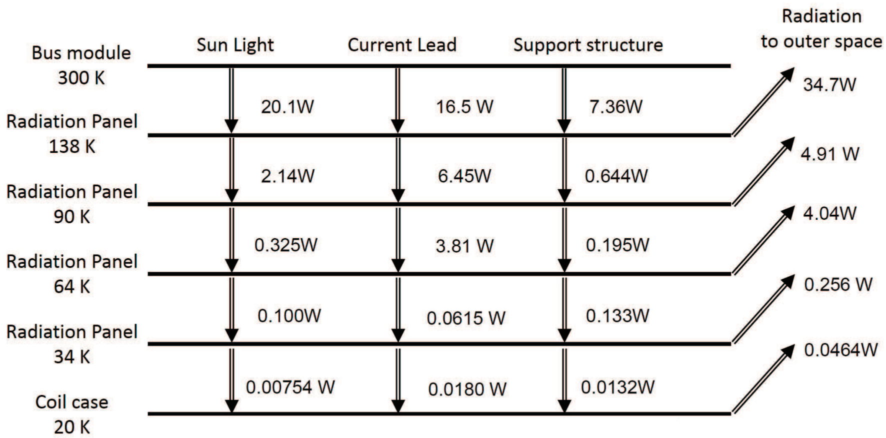

Figure 6.7: An example of the thermal block diagram of the HTS coil system.

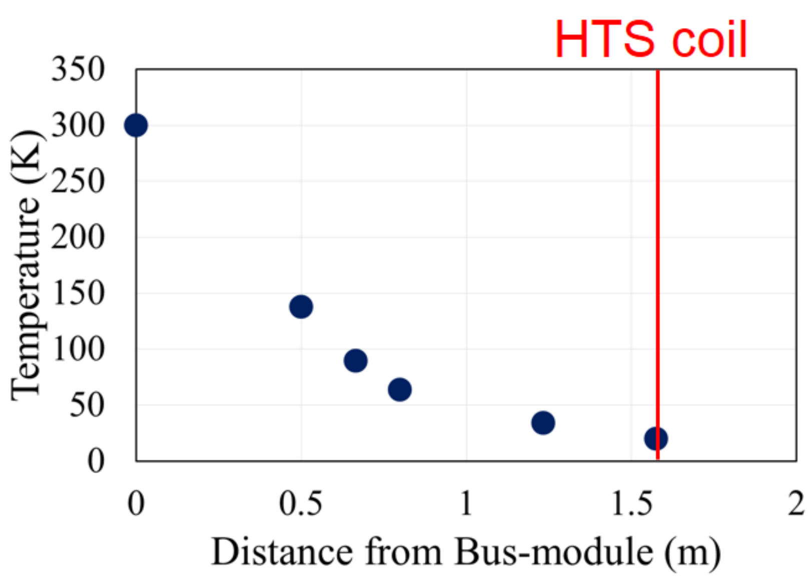

Figure 6.8: Cooling effect of the cooling system.

magnetic axis should be perpendicular direction to the sun direction considering the cooling condition to release the heat generated in the coil.

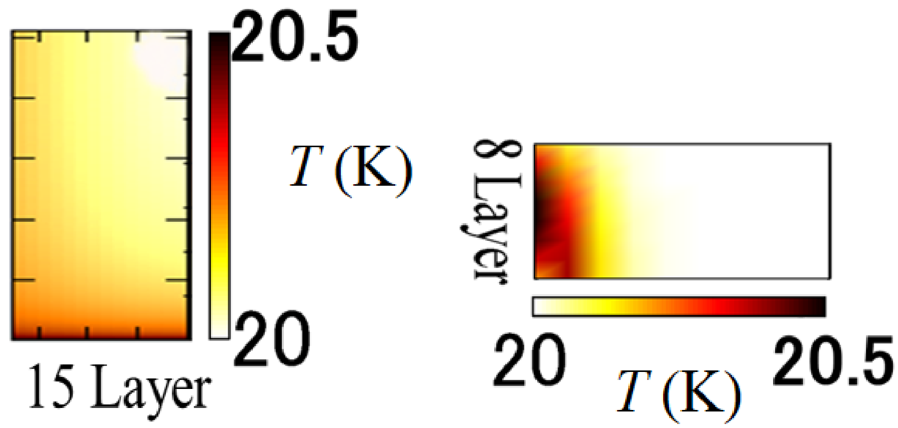

(a) Perpendicular direction (b) Parallel direction

Figure 6.9: Temperature, T, distribution in the coils at $T_{\mathrm{op}} = 20$ K, $I = I_{\mathrm{cmin}}$.

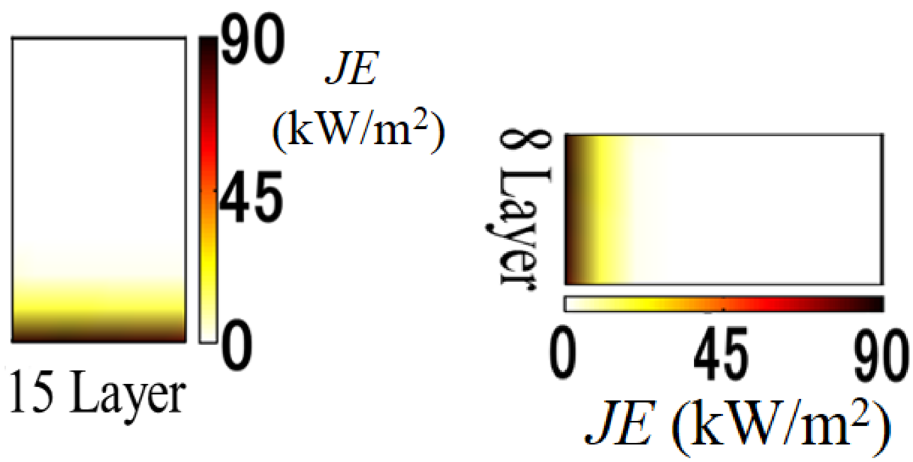

(a) Perpendicular direction (b) Parallel direction

Figure 6.10: Heat generation density, $J \cdot E$, distribution in the coils at $T_{\mathrm{op}} = 20$ K, $I = I_{\mathrm{cmin}}$

6.4 Optimization of HTS Coil System for Magneto Plasma Sail

By using the developed analysis method in this study, the configuration of the coil is optimized to maximize the magnetic moment to mass ratio of the system, i.e. the acceleration of the magneto plasma sail. We analyzed with three kinds of the coil configurations; circular, multi-pole, and racetrack coil shown in Fig. 5.9. The coil parameters, i.e., outside radius, r_{o}, the number of layers, m, and stack, n, of the coils as well as the major and minor radius of the race track coil and coil number of the multi-pole coil were optimized in order to maximize the magnetic moment to mass ratio of the magneto plasma sail in the case of the perpendicular or parallel magnetic axis. We used the genetic algorithm as the optimization method of the HTS coil system with the constraint conditions described below;

1. YBCO coated-conductor with 3.0 mm in width and 0.1 mm in thickness, which is additionally reinforced with Hastelloy® substrates (0.05 mm in thickness), was used.
2. Direction of the magnetic axis is set to the perpendicular or parallel direction to the sun direction (solar wind).
3. Operational temperature T_{op} is set to 10K, 20 K, 30 K, 40 K or 50 K.
4. Total weight of the HTS system is less than 464 kg, because of the mass limit for the spacecraft.
5. For circular coil, coil diameter $2r_o$= 4 m. The height of the coil is limited to 7 m.
6. For multi-pole coil, each coil diameter $2r_o$= 4 m. The height of each coil is limited to 1.75 m.
7. For racetrack coil, the coil size is limited to 4 m $\times$ 7 m (minor (shorter) diameter $\times$ major (longer) diameter).

In the present analysis, the maximum magnetic moment was defined if one of the constraint conditions described below is satisfied:

1. The temperature of the coil diverges and coil quench occurs according to the developed thermal analysis.
2. Hoop stress or transverse compressive stress applied to the coil exceeds 1 GPa or 150 MPa, respectively [97]-[99].

The optimal configuration of the coil was searched using the genetic algorithm to maximize the magnetic moment to mass ratio of the magneto plasma sail, in the case of circular, multi-pole and racetrack coil on the condition of the perpendicular and parallel direction of the magnetic axis.

Figures 6.11 shows the result of the circular coil system optimization for a variety of the operational temperatures from 10 K to 50 K in the both cases of the magnetic axis. The magnetic moment to mass ratio is normalized by 1.1×10^5 A · m^{-1}, which is the minimum requirement for the magneto plasma sail (10^6 A-turns with an outside radius r_o of 2 m with the system weight of 314 kg)As shown in the figure, the magnetic moment to mass ratio reaches the highest value at the operational temperature around 20 K. Also, in the case of the perpendicular magnetic axis, the magnetic moment to mass ratio becomes larger. This is because the cooling characteristics of the coil can be improved on the perpendicular direction as mentioned in the previous section, and also the mass of the cooling system is smaller as shown in Fig. 6.14 as the diameter of the system can be smaller. A previous study reported that, in terms of the attitude stability of the spacecraft, the direction of the magnetic axis should be the perpendicular direction to the solar wind. This study also revealed that the thermal stability and cooling characteristics can be improved when the magnetic axis of the coil is perpendicular to the sun direction.

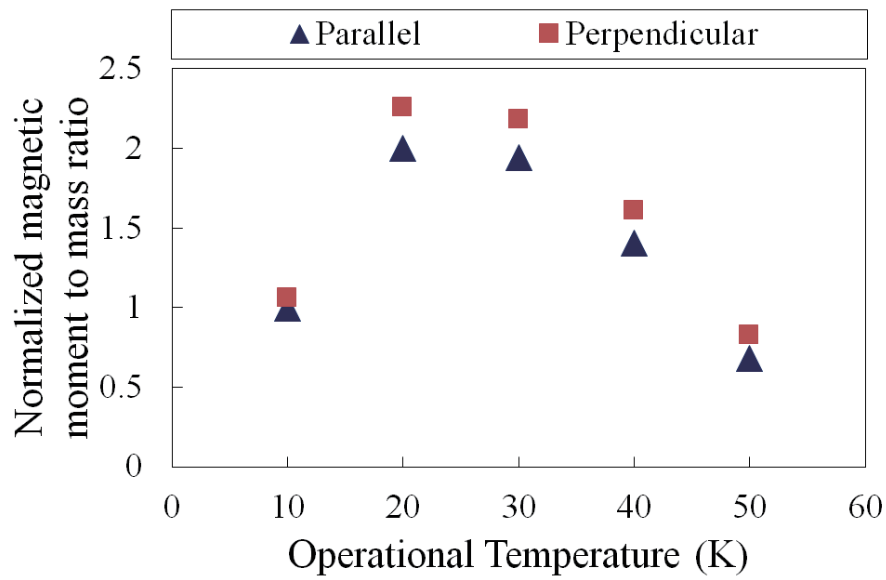

Figure 6.11: Dependence of the magnetic moment to mass ratio of the magneto plasma sail on the operational temperature of the HTS coils.

Figure 6.13 indicates the dependence of the magnetic moment to mass ratio of the magneto plasma sail on the operational temperature of the HTS coil for three kinds of the above-mentioned coils. The magnetic moment to mass ratio is normalized by the minimum requirement for the magneto plasma sail. As can be seen in Fig. 6.13, for all kinds of the coils, the magnetic moment to mass ratio is the highest at the operational temperature of around 20 K and 30 K. On the other hand, in the case of using the HTS coil at less than 20 K, the magnetic moment to mass ratio rapidly decreases because the weight of the radiation cooling system becomes larger as shown in Fig. 6.14. As can be seen in Figs. 6.13 and 6.14,

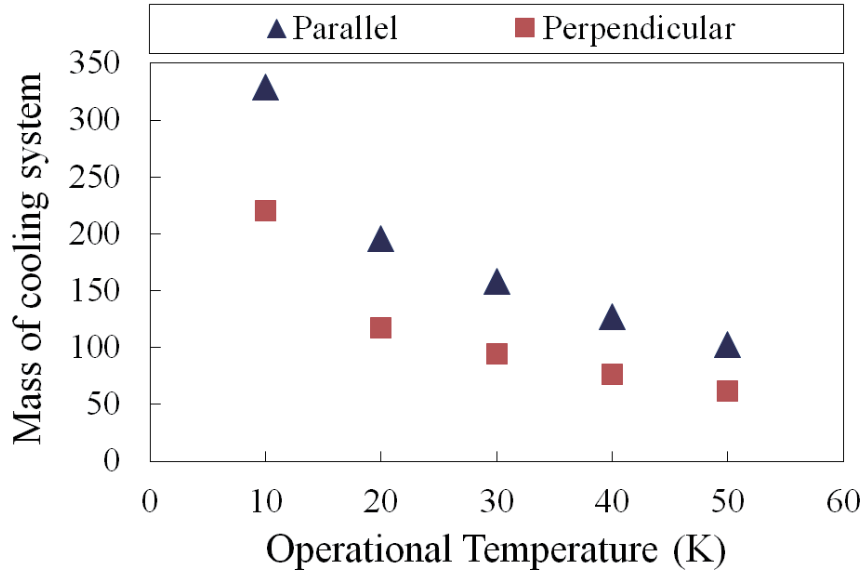

Figure 6.12: Dependence of the weight of the cooling system on the operational temperature of the HTS coils.

the magnetic moment to mass ratio of the multi-pole coil is lower than that of the circular coil and racetrack coil as the mass of the cooling system is much larger. This is because, for the multi-pole coil, more than one coil must be cooled down to the operational temperature, and the cooling structure becomes larger. Considering the cooling system, the multi-pole coil is not promising for the use in space. Table. 6.2 shows the optimal configurations of each coil type for obtaining the maximum magnetic moment to mass ratio under the constraint conditions described above and Fig. 6.15 shows illustrations of the optimal system of the magneto plasma sail with racetrack coil and multi-pole coil. This study reveals that the system with the racetrack coil can maximize the magnetic moment to mass ratio which is 2.8 times larger than that of the minimum requirement for the magneto plasma sail, because both of the critical current and the area of the racetrack coil can be larger than those of the circular coil despite the cooling mass is slightly larger than that of the circular coil.

6.5 Summary

The HTS coil system was optimized to maximize the magnetic moment to mass ratio of the magneto plasma sail using YBCO coated conductors. For the coil design, we analyzed the thermal stability and applied stresses of the HTS coils, and also the weight of the cooling system for each coil configuration. We optimized the configuration of the coil using the genetic algorithm in the case of circular, multi-pole and racetrack coil at from 10 K to 50 K

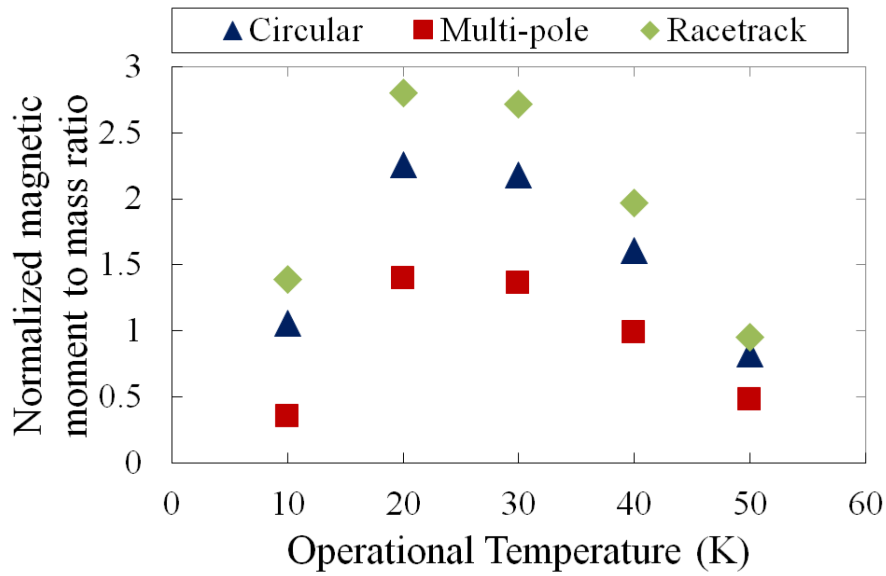

Figure 6.13: Dependence of the magnetic moment to mass ratio of the magneto plasma sail on the operational temperature of the HTS coils (Magnetic axis is the perpendicular direction to the sun direction).

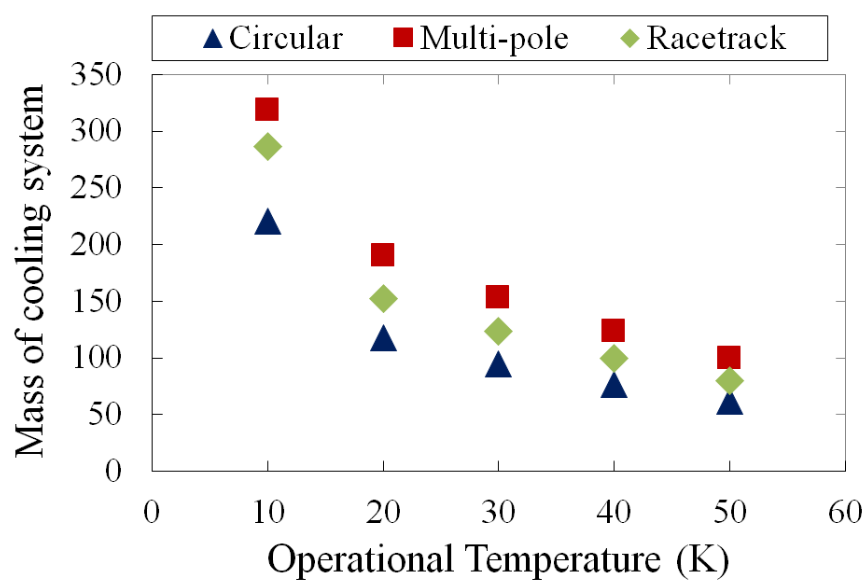

Figure 6.14: Dependence of the weight of the cooling system on the operational temperature of the HTS coils (Magnetic axis is the perpendicular direction to the sun direction).

Table 6.2: Optimal HTS coil to obtain the maximum magnetic moment for three kinds of the coil configuration.

	YBCO circular	YBCO racetrack	YBCO multi-pole (coil number: 2)
Operational Temperature	20 K	20 K	20 K
Outside radius r_o	1.9 m	1.85 m×3.5 m	1.9 m × 2
Stack number n	306	453	284
Layer number m	15	6	7
Operational current	523 A	612 A	523 A
Magnetomotive force NI_op (A-turns)	2.4×10^6	1.7×10^6	2.1×10^6
Normalized magnetic moment	2.4	2.8	1.4
Cooling Mass M_cool	117 kg	153 kg	192 kg

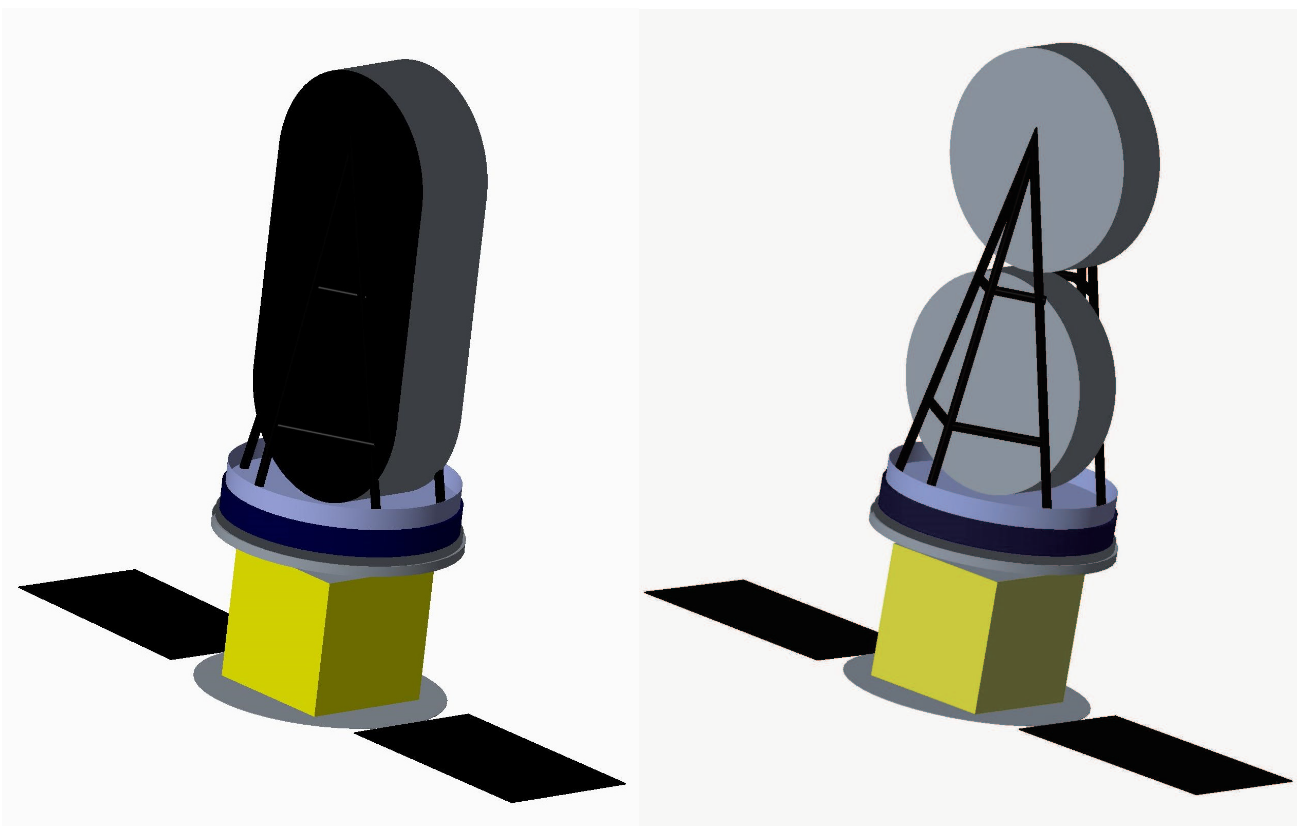

(a) Racetrack coil

(b) Multi-pole coil

Figure 6.15: CAD model of the optimal system of the magneto plasma sail with (a) racetrack coil and (b) multi-pole coil.

on the condition of the perpendicular or parallel direction of the magnetic axis. For all kinds of the coils, the maximum magnetic moment to mass ratio can be obtained at the operational temperature of around 20 K. On the other hand, in the case of using the HTS coil at less that 20 K, the magnetic moment to mass ratio rapidly decreases because the weight of the radiation cooling system becomes huge. It was also shown that the magnetic moment to mass ratio of the multi-pole coil is lower than that of the circular coil and racetrack coil as the cooling structure becomes larger to cool down more than one coil. From a point of view of maximizing the magnetic moment to mass ratio for the spacecraft, the racetrack coil is the optimal configuration and the magnetic moment to mass ratio, i.e., acceleration obtained from the magneto plasma sail, can be increased to 2.8 times larger than the minimum requirement for space missions.

Chapter 7

Concluding Remarks

7.1 Summary and Conclusions

In the present thesis, a study on a High Temperature Superconducting (HTS) coil system for one of the next-generation propulsion system, Magneto Plasma Sail, was reported. To maximize the acceleration obtained by the magneto plasma sail, the HTS coil system for the magneto plasma sail was characterized by a developed analysis model in this study and optimized for maximizing the magnetic moment to mass ratio of the spacecraft.

In chapter 1, an overview of the existing and future space propulsion systems was explained. The concept of the magnetic sail and magneto plasma sail as well as previous researches about these propulsion systems are introduced. Basic characteristics of HTS and an outline of the HTS coil system were also described. The objective of this study was then explained.

In chapter 2, thermal diffusivities of Bi-2223/Ag tape and YBCO coated-conductor were measured to design a conduction-cooled HTS coil for the magneto plasma sail with taking into account the thermal behavior of the coil. Temperature traces of the bundled conductors were measured for the heater disturbance at conduction cooling conditions. Obtained experimental results were reproduced using one-dimensional as well as two-dimensional heat balance equations. It was shown that the analysis results successfully reproduced the experimental results at a wide temperature range. According to the modeling results, it was clarified that the thermal diffusivity of the YBCO coated-conductors in the perpendicular direction to the tape surface was five orders of magnitude lower than that of the Bi-2223/Ag tape. In addition, it was also shown that, even for the Bi-2223/Ag coil, the thermal stability of the coil will be a serious constraint because the thermal diffusivity of the coils or bundled conductors become lower than that of the tape itself. Our results indicated that to design a conduction-cooled coil for use in space, such a low thermal diffusivity of HTS must be taken into account.

In chapter 3, we developed an analysis method to evaluate the current transport performances and thermal stabilities of HTS coils, for the design of the optimal coil system of the magneto plasma sail. Our analysis can evaluate the quench current which causes a coil quench by estimating a heat generation and solving the three-dimensional heat balance equation. The analysis showed that this quench current of the coil was not consistent with the critical current based on the electric field criterion, 1.0×10^{-4} Vm^{-1}. In the analysis, longitudinal inhomogeneity of the critical current of the HTS tape was considered, and it was confirmed that the characteristics inhomogeneity deteriorated the current transport performance and thermal stability of the coil. A Bi-2223/Ag scale-down model coil and a conduction-cooed experimental system were also established. It was shown that the current transport performance and thermal behavior of the coil obtained by the analysis with taking into account the cooling condition quantitatively agreed with the experimental ones at various operational temperatures. These results proved the validity of the analysis method and the conduction-cooling experimental system for the magneto plasma sail drive coil.

In chapter 4, in order to characterize and design optimal HTS coils for space missions, we developed a numerical analysis method based on the percolation depinning and the flux creep models, considering screening currents, induced in the coil. In this study, screening currents induced in a Bi-2223/Ag double pancake coil was investigated and modeled. We measured the decay behavior of the magnetic field due to screening currents, and then modeled the results assuming an equivalent loop length for screening currents in the coil. The experimental and analytical results suggest that the decay behavior of screening currents in the Bi-2223/Ag tape was dominated by the silver sheath resistance and the flux creep, especially at a lower load factor. In addition, the experimental results under varying conditions could be quantitatively modeled assuming an equivalent loop length of approximately 9 mm for screening currents in the coil. To use DC/DC converters as a power supply and design a light-weight HTS coil system for space missions, we also investigated the effects on the conduction-cooled coil performance of the transport AC losses under various ripple currents with DC offsets. The developed analysis method can estimate the effective AC loss in HTS coils. Our analysis results implied that the AC loss with the ripple current deteriorated the thermal stability of a conduction-cooled coil when HTS tapes in the coil are in the flux-flow state, e.g., the load factor (operational current/critical current) of 80%. However, at a lower load factor, most of the AC power were consumed as a reactive power and the ripple current cannot be a serious problem for the thermal stability of the conduction-cooled coil. These results suggest that, if the operational load factor is properly selected by the developed analysis code, the light-weight power supply system including an AC ripple current can be used for the HTS coil spacecraft system.

In chapter 5, an HTS coil with a large magnetic moment using YBCO coated conductors and Bi-2223/Ag tape was designed for a magneto plasma sail. For the coil design, we analyzed the current transport properties, thermal behavior, and applied stresses of the HTS coils, and compared these characteristics for each coil configuration. As a sensitivity analysis, it was revealed that a thin-walled coil with a large diameter can generate a larger magnetic moment with higher thermal stability and lower hoop stress. However, transverse compressive stress becomes a serious constraint factor for such a thin-walled coil design. We also analyzed with the racetrack and multi-pole coil configurations as well as a Bi-2223/Ag circular coil to obtain a larger magnetic moment. From a point of view of maximizing the magnetic moment for the spacecraft, the racetrack and multi-pole coil is more suitable configuration than a circular coil and the magnetic moment can be increased to approximate three times larger than the minimum requirement for the magneto plasma sail. The present study also investigated the required weight of the coil to obtain the minimum requirement of the magnetic moment at a variety of operational temperature in the case of the racetrack coil using the YBCO CCs. According to the analysis result, the operational temperature of the magnetic sail drive coil should be less than 30 K to meet the requirement of the magnetic moment for the magneto plasma sail, considering the mass limit of the spacecraft.

In chapter 6, the HTS coil system using YBCO coated conductors for the magneto plasma sail is optimized to maximize the magnetic moment to mass ratio by using the genetic algorithm. We also analyzed the weight of the cooling system for each coil configuration. The configuration of the coil using the genetic algorithm in the case of circular, multi-pole and racetrack coil at from 10 K to 50 K. The coil configuration is optimized in the case the direction of the magnetic axis is the perpendicular or parallel direction to the sun direction. For all kinds of the coils, the maximum magnetic moment to mass ratio can be obtained at the operational temperature of around 20 K. On the other hand, in the case of using the HTS coil at less that 20 K, the magnetic moment to mass ratio rapidly decreases because the weight of the radiation cooling system becomes huge. It was also shown that the magnetic moment to mass ratio of the multi-pole coil is lower than that of the circular coil and racetrack coil as the cooling structure becomes larger to cool down more than one coil. From a point of view of maximizing the magnetic moment to mass ratio for the spacecraft, the racetrack coil is the optimal configuration and the magnetic moment to mass ratio, i.e., acceleration obtained from the magneto plasma sail can be increased to 2.8 times larger than the minimum requirement for space missions.

In conclusion, to maximize the acceleration of the magneto plasma sail, the HTS coil system for the magneto plasma sail was successfully characterized by the developed analysis model based on the current transport characteristics of HTS. Using the developed model, the HTS coil system was optimized to maximize the magnetic moment to mass ratio of the spacecraft. The magnetic moment to mass ratio was successfully improved approximate three times and, at the same time, the weight of the HTS coil system can be within the mass limit of the spacecraft. This study proved the possibility to increase the thrust to mass ratio of the sail system greatly, and leads to realizing a space propulsion system using an HTS coil.

Acknowledgment

I would like to express my sincere and special appreciation to my research supervisor Professor Hiroshi Yamakawa at Research Institute for Sustainable Humanosphere (RISH) of Kyoto University for giving me an opportunity to pursue this study and for his useful advice, comments, and helpful suggestions in the satellite meeting every week in spite of his busy schedule. His advice has helped me to set a direction of my research. I am also grateful to his support to my research for five and a half years from my bachelor's course. I have been always inspired by his way of innovative thinking. He has been a role model for me as a scientist, and made me decide to be a researcher. I would like to express the deepest appreciation to him.

I deeply thank Associate Professor Taketsune Nakamura at Kyoto University for his valuable suggestions and advice as a specialist of the superconductivity. I am also grateful to his careful reading of most part of this thesis and my research papers, and helpful suggestions for revisions. I would also like to offer special thanks to his careful support and advice for the experiments of this study at Yamakawa laboratory as well as at his laboratory. Without his guidance and help, the present thesis has not been completed. I am particularly grateful for the assistance given by him.

I am deeply grateful to Associate Professor Ikkoh Funaki at the Institute of Space and Astronautical Science (ISAS) of Japan Aerospace Exploration Agency (JAXA) for his helpful advice and comments in the magsail meeting. I have greatly benefited from his advice as a group leader of the magneto plasma sail research group at ISAS/JAXA. I owe a very important debt to him for providing me with an opportunity to study the magneto plasma sail, which has been a really attractive research theme for me. I would like to show my greatest appreciation to him.

I owe my gratitude to Professor Tetsuji Matsuo at Kyoto University for our regular discussions and giving me useful comments as a specialist of the electromagnetic phenomena. I also sincerely appreciate his many helpful advice and suggestions to revise the present thesis.

I want to thank Associate Professor Hirotsugu Kojima and Dr. Yoshikatsu Ueda for their thoughtful suggestions and support in the satellite meeting.

I am indebt to Professor Yoshiharu Omura, Professor Naoki Shinohara, Associate Professor Yusuke Ebihara, and Associate Professor Tomohiko Mitani for their helpful suggestions and advice at the monthly space group seminar. I deeply thank Dr. Masafumi Shoji, Dr. Hajime Fukuhara, and Dr. Yasumasa Ashida for their warm advice, guidance and dedicated help as my seniors. Their advice greatly promoted my study. I also appreciate the previous work for the HTS coil for the magneto plasma sail conducted by Mr. Tomokazu Koyama. I wish to thank Dr. Keiichiro Kashimura, Dr. Masaki Nakamiya, Dr. Yao Yao, Dr. Yong Huang and the whole students in the space group laboratory for their help to my research. I would like to express my gratitude to Ms. Megumi Ogawa, secretary of Professor Hiroshi Yamakawa, for her careful support to my paperwork.

I would like to express my acknowledgments to Professor Hideyuki Usui of Kobe University, Associate Professor Iku Shinohara of ISAS/JAXA, Associate Professor Hiroyuki Nishida of Tokyo University of Agriculture and Technology, Associate Professor Masao Nakamura of Osaka Prefecture University, Dr. Yoshihiro Kajimura of Akashi National College of Technology, Dr, Kazuma Ueno of ISAS/JAXA and Dr. Yuya Oshio of ISAS/JAXA as one of the members of the magneto plasma sail research group at ISAS/JAXA.

I gratefully appreciate the financial support from Japan Society for the Promotion of Science (JSPS) that could make me devote most of my time to this research as a Ph. D. candidate. This work has also been financially supported by the engineering committee of the Institute of Space and Astronautical Science of the Japan Aerospace Exploration Agency and by a Grant-in-Aid for JSPS Fellows. Some analyses in the present study were performed using the Kyoto-daigaku Denpa-kagaku Keisanki-jikken (KDK) system of Research Institute for Sustainable Humanosphere at Kyoto University.

Finally, I would like to show my greatest appreciation to my parents, Mitsutaka and Keiko, and my dear wife, Keika, for their kind support and warm encouragement for my student life.

Bibliography

[1] NASA homepage, “http;//www.nasa.gov.”

[2] R. A. Kerr, “It’s Official - Voyager Has Left the Solar System,” Science, vol. 13, no. 6151, pp.1158-1159, 2013.

[3] Y. Tsuda, O. Mori, R. Funase, H. Sawada, T. Yamamoto, T. Saiki, et al., “Flight status of IKAROS deep space solar sail demonstrator,” Acta Astronautica, vol. 69, pp. 833-840, 2011.

[4] JAXA homepage, “http://www.jaxa.jp.”

[5] P. Janhunen, “Electric Sail for Spacecraft Propulsion,” Journal of Propulsion and Power, vol. 20, pp. 763-764, 2004/07/01 2004.

[6] E-sail, “http://www.electric-sailing.fi/”

[7] J. Envall, P. Janhunen, P. Toivanen, M. Pajusalu, E. Ilbis, J. Kalde, et al., “E-sail test payload of ESTCube-1 nanosatellite,” arXiv preprint arXiv:1404.6961, 2014.

[8] R. M. Zubrin and D. G. Andrews, “Magnetic sails and interplanetary travel,” Journal of Spacecraft and Rockets, vol. 28, pp. 197-203, Mar-Apr 1991.

[9] I. Funaki, H. Yamakawa, K. Fujita, H. Ogawa, S. Nonaka, S. Sawai, H. Kuninaka, and H. Otsu, “Study of a Plasma Sail for Future Deep Space Missions,” Proceedings of 28th International Electric Propulsion Conference, IEPC2003-089, Mar 2003.

[10] H. Yamakawa, I. Funaki, Y. Nakayama, K. Fujita, H. Ogawa, S. Nonaka, et al., “Magneto-plasma sail: An engineering satellite concept and its application for outer planet missions,” Acta Astronautica, vol. 59, pp. 777-784, Oct-Dec 2006.

[11] D. G. Andrews and R. M. Zubrin, “Magnetic Sails and Interstellar Travel,” Journal of the British Interplanetary Society, vol. 43, pp. 265–272, 1990.

[12] R. M. Zubrin, “The Use of Magnetic Sails to Escape from Low Earth Orbit,” Journal of the British Interplanetary Society, vol. 46, pp. 3–10, 1993.

[13] R. M. Winglee, J. Slough, T. Ziemba, and A. Goodson, “Mini-magnetospheric plasma propulsion: Tapping the energy of the solar wind for spacecraft propulsion,” Journal of Geophysical Research, vol. 105, pp. 21067-21077, Sep 1 2000.

[14] R. M. Winglee, T. Ziemba, P. Euripides, and J. Slough, “Magnetic inflation produced by the Mini-Magnetospheric Plasma Propulsion (M2P2) prototype,” AIP Conference Proceedings, vol. 608, pp. 433-440, 2002.

[15] G. Vulpetti, “A critical-review on the viability of a space propulsion based on the solar-wind momentum flux,” Acta Astronautica, vol. 32, pp. 641-644, Sep 1994.

[16] C. Bruno and S. Giucci, “Cryogenic technology to improve electric thrusters,” Acta Astronautica, vol. 51, pp. 855-863, Dec 2002.

[17] C. Bruno and D. Casali, “Superconducting materials applied to electric propulsion systems,” Journal of Spacecraft and Rockets, vol. 41, pp. 671-676, Jul-Aug 2004.

[18] C. M. Rey, W. C. Hoffman, F. R. Chang-Diaz, A. V. Ilin, A. J. Petro, D. S. Winter, et al., “Design and fabrication of an HTS magnet for the VASIMR experiment,” IEEE Transactions on Applied Superconductivity, vol. 12, pp. 993-996, Mar 2002.

[19] Y. Wang, B. Li, P. Zhang, and S. Wang, “Magnet configuration and experimental analysis of helicon source for space magnetoplasma propulsion,” IEEE Transactions on Applied Superconductivity, vol. 20, pp. 993-996, 2010.

[20] I. Funaki, H. Sugita, K. Ishimura, H. Yamakawa, and T. Nakamura, Symp. on Flight Mechanics and Astrodynamics, 2009 (in Japanese).

[21] K. Ueno, T. Kimura, T. Ayabe, I. Funaki, H. Horisawa, and H. Yamakawa, “Laboratory Experiment of Magneto Plasma Sail, Part 1: Pure Magnetic Sail,” 30th International Electric Propulsion Conference, Florence, Italy, IEPC 2007-61, Sept. 2007.

[22] K. Ueno, T, Kimura, T. Ayabe, I. Funaki, H. Yamakawa, and H. Horisawa, “Thrust Measurement of Pure Magnetic Sail”, ISTS, Hamamatsu, Japan, 2008-b-05, 2008.

[23] K. Ueno, I. Funaki, and H. Yamakawa, “Thrust Measurement of a Pure Magnetic Sail Using the Parallelogram-Pendulum Method, ” Journal of Propulsion and Power, vol. 25, no. 2, pp. 536-539, 2009.

[24] I. Funaki, T. Kimura, K, Ueno, H. Horisawa, H. Yamakawa, Y. Kajimura, H. Nakashima, and Y. Shimizu, "Laboratory Experiment of Magneto Plasma Sail, Part 2: Magnetic Field Inflation," 30th International Electric Propulsion Conference, Florence, Italy, IEPC-2007-94, Sept. 2007.

[25] T. Koyama, "Study on High Temeperature Superconducting coil for magnetic sail," Master Thesis, Kyoto University, 2011.

[26] J. R. Spreiter, and B. R. Briggs, "Theoretical Determination of the Form of the Boundary of the Solar Corpuscular Stream Produced by Interaction with the Magnetic Dipole Field of the Earth," Journal of Geophysical Research, vol. 67, no.1, pp. 37-51, 1962.

[27] Cattell, C., Catto, P., Funsten, H., Garnier, D., Hershkwitz, N., Myers, R., Petschek, H., and Winske, D., "Physics and Technology of the Feasibility of Plasma Sails," Plasma Science and Fusion Center website: http://www.psfc.mit.edu/library1/catalog/reports/2000/05ja/05ja026/05ja026_full.pdf.

[28] H. Yamakawa, "Dynamics of Radially Accelerated Trajectories," Transactions of the Japan Society for Aeronautical and Space Sciences, vol. 49, no. 164, pp. 77-80, 2006.

[29] H. Yamakawa, "Optimal Radially Accelerated Interplanetary Trajectories," Journal of Spacecraft and Rockets, vol. 43, no. 1, pp. 116-120, 2006.

[30] A. A. Quarta, G. Mangali, and G. Aliasi, "Optimal control law for heliocentric transfers with a magnetic sail," Acta Astronautica, vol. 89, pp. 216-225, 2013.

[31] J. Slough, "Plasma Sail Propulsion Based on the Plasma Magnet," 30th International Electric Propulsion Conference, Florence, Italy, IEPC-2007-15, Sep, 2007.

[32] I. Funaki, Y. Kajimura, Y. Ashida, H. Nishida, Y. Oshio, I. Shinohara, and H. Yamakawa, "The Use of Dipole Plasma Equilibrium for Magnetic Sail Spacecraft", Transactions of Fusion Science and Technology, vol. 63, no. 1T, pp. 168-171, 2013.

[33] D. Akita, and K. Suzuki, "Preliminary Study on Magnetic Sail for Escape Mission from the Solar System," ISTS, Miyazaki, Japan, 2004-b-47, 2004.

[34] S. Saha, N. Singh, P. Craven, D. Gallagher, and J. Jones, "Development of 3D Hybrid Code and Its Application to M2P2," Space Technology and Applications International Forum-STAIF 2002, Albuquerque, NM, pp. 441-446, 2002.

[35] G. Khazanov, P. Delamere, K. Kabin, and T. J. Linde, "Fundamentals of the Plasma Sail Concept: Magnetohydrodynamic and Kinetic Studies," Journal of Propulsion and Power, vol. 21, no. 5, pp. 853-861, 2005.

[36] N. Omidi, and H. Karimabadi, "Kinetic Simulation/Modeling of Plasma Sail," 39th AIAA/ASME/SAE/ASEE Joint Propulsion Conference and Exhibit, Huntsville, Alabama, Paper 2003-5226, Jul, 2003.

[37] Y. Kajimura, I. Funaki, I. Shinohara, H. Usui, and H. Yamakawa, "Thrust Evaluation of Magneto Plasma Sail by Using Three-Dimensional Hybrid PIC Code," 46th AIAA/ASME/SAE/ASEE Joint Propulsion Conference and Exhibit, Nashville, Tennessee, AIAA-2010-6686, Jul, 2010.

[38] M. Pfeiffer, D. Petkow, G. Herdich, and S. Fasoulas, "Assessment of a Numerical Approach Suitable for the M2P2 Problem," The Open Plasma Physics Journal, vol. 4, pp. 24-33, 2011.

[39] H. Nishida, H. Ogawa, I. Funaki, K. Fujita, H. Yamakawa, and Y. Inatani, "Verification of Momentum Transfer Process on Magnetic Sail Using MHD Model," 41st AIAA/ASME/SAE/ASEE Joint Propulsion Conference and Exhibit, Tucson, Arizona, Paper 2005-4463, Jul, 2005.

[40] H. Nishida, and Y. Nakayama, "Two-dimensional Magnetohydrodynamic Simulation of a Magnetic Sail," Journal of Spacecraft and Rockets, vol. 43, no. 3, pp. 667-672, 2006.

[41] K. Fujita, "Particle Simulation of Moderately Sized Magnetic Sails," Journal of Space Technology and Science, vol. 20, no. 2, pp. 26-31, 2005.

[42] Y. Kajimura, H. Usui, I. Funaki, K. Ueno, M. Nunami, I. Sinohara, N. Nakamura, and H. Yamakawa, "Hybrid Particle-in-Cell Simulations of Magnetic Sail in Laboratory Experiment," Journal of Propulsion and Power, vol. 26, no. 1, pp. 159-166, 2010.

[43] D. Akita, and K. Suzuki, "Kinetic Analysis on Plasma Flow of Solar Wind around Magnetic Sail," AIAA paper 2005-4791, June 2005.

[44] T. Moritaka, Y. Kajimura, H. Usui, M. Matsumoto, T. Matsui, and I. Shinohara, "Momentum transfer of solar wind plasma in a kinetic scale magnetosphere," Physics of Plasmas, vol. 19, pp. 032111-1-13, 2012.

[45] H. Nishida, and I. Funaki, "Analysis of Thrust Characteristics of a Magnetic Sail in Magnetized Solar Wind," Journal of Propulsion and Power, vol. 28, no. 3, pp. 336-342, 2012.

[46] R. Asahi, I. Funaki, K. Fujita, H. Yamakawa, H. Ogawa, S. Nonaka, S. Sawai, H. Nishida, Y. Nakayama, and H. Otsu, “Numerical Study on Thrust Production Mechanism of a Magneto Plasma Sail,” AIAA paper 2004-3502, June 2004.

[47] H. Nishida, I. Funaki, H. Ogawa, and Y. Inatani, “MHD Analysis on Propulsive characteristics of Magneto Plasma Sail,” 30th International Electric Propulsion Conference, Florence, Italy, IEPC-2007-195, Sep, 2007.

[48] Y. Kajimura, K. Noda, H. Nakashima, and I. Funaki, “Feasibility Study of Magneto Plasma Sail by Using Numerical Simulation and Experiment,” Aiaa-2007-587, Jan. 2007.

[49] Y. Kajimura, I. Funaki, M. Matsumoto, I. Shinohara, H. Usui, and H. Yamakawa, “Thrust and Attitude Evaluation of Magnetic Sail by Three-dimensional Hybrid Particle-in-Cell Code,” Journal of Propulsion and Power, vol. 28, no. 3, pp. 652-663, 2012.

[50] Y. Ashida, I. Funaki, H. Yamakawa, Y. Kajimura, and H. Kojima, “Numerical Model for Thrust Evaluation of a Magnetic Sail,” Japan Society for Aeronautical and Space Sciences, vol. 59, no. 688, pp. 126-131, 2011.

[51] Y. Ashida, I. Funaki, H. Yamakawa, Y. Kajimura, and H. Kojima, “Thrust Evaluation of a Magnetic sail by Flux-Tube Model,” Journal of Propulsion and Power, vol. 28, no. 3, pp. 642-651, 2012.

[52] Y. Ashida, I. Funaki, H. Yamakawa, H. Usui, Y. Kajimura, and H. Kojima, “Two-Dimensional Particle-in-Cell Simulation of Magnetic Sail,” Journal of Propulsion and Power, vol. 30, no. 1, pp. 233-245, 2014.

[53] Y. Ashida, H. Yamakawa, I. Funaki, H. Usui, Y. Kajimura, and H. Kojima, “Thrust Evaluation of Small-scale Magnetic Sail Spacecraft by Three-Dimensional Particle-in-Cell Simulation,” Journal of Propulsion and Power, vol. 30, no. 1, pp. 186-196, 2014.

[54] M. A. Green, and G. F. Smoot: “The ASTROMAG superconducting magnet facility configured for a free-flying satellite,” Cryogenics, vol. 32, pp.91-97, 1992.

[55] T. Manabe, T. Nakamura, K. Higashikawa, K. Shikimachi, N. Hirano, and S. Nagaya: “Study on heat loss characteristic of bundled MOCVD-YBCO coated conductors,” Abstracts of CSJ Conference, vol.77 p. 126, 2007.

[56] H. Sugita, T. Nakagawa, H. Murakami, A. Okamoto, H. Nagai, M. Murakami, et al., "Cryogenic infrared mission "JAXA/SPICA" with advanced cryocoolers," Cryogenics, vol. 46, pp. 149-157, 2006.

[57] K. Yamafuji and T. Kiss, "Current-voltage characteristics near the glass-liquid transition in high-T-c superconductors," Physica C, vol. 290, pp. 9-22, Oct 15 1997.

[58] A. I. Kosse, A. Y. Prokhorov, V. A. Khokhlov, G. G. Levchenko, A. V. Semenov, D. G. Kovalchuk, et al., "Measurements of the magnetic field and temperature dependences of the critical current in YBCO films and procedures for an appropriate theoretical model selection," Superconductor Science and Technology, vol. 21, p. 075015, 2008.

[59] M. Inoue, T. Kiss, K. Motoyama, S. Awaji, K. Watanabe, M. Yoshizumi, et al., "Critical current property in YBCO coated conductor fabricated by improved TFA–MOD process," Physica C: Superconductivity and its applications, vol. 469, pp. 1443-1445, 2009.

[60] P. Sunwong, J. S. Higgins, and D. P. Hampshire, "Angular, Temperature, and Strain Dependencies of the Critical Current of DI-BSCCO Tapes in High Magnetic Fields," IEEE Transactions on Applied Superconductivity, vol. 21, pp. 2840-2844, Jun 2011.

[61] H. Yamasaki, I. Yamaguchi, M. Sohma, W. Kondo, H. Matsui, T. Manabe, et al., "Temperature dependence of magnetic-field angle dependent critical current density and the flux pinning in YBa2Cu3O7 thin films," Physica C: Superconductivity and its applications, vol. 478, pp. 19-28, 2012.

[62] K. Higashikawa, T. Nakamura, and T. Hoshino, "Anisotropic distributions of current density and electric field in Bi-2223/Ag coil with consideration of multifilamentary structure," Physica C: Superconductivity and its applications, vol. 419, pp. 129-140, 2005.

[63] K. Higashikawa, T. Nakamura, and H. Okamoto, "Analysis of discharging characteristics in a Bi-2223/Ag coil for SMES with consideration of cooling capacity of a cryocooler," IEEE Transactions on Applied Superconductivity, vol. 16, pp. 578-581, Jun 2006.

[64] K. Higashikawa, T. Nakamura, M. Sugano, K. Shikimachi, N. Hirano, and S. Nagaya, "Performance improvement of YBCO coil for high-field HTS-SMES based on homogenized distribution of magnetically-mechanically influenced critical current," IEEE Transactions on Applied Superconductivity, vol. 18, pp. 758-761, Jun 2008.

[65] K. Higashikawa, T. Kiss, M. Inoue, S. Awaji, K. Watanabe, H. Fukushima, et al., “Significant reduction in volume, stored energy and magnetization loss of high-field magnet coil based on the improvement of critical current characteristics in GdBCO coated conductor,” Physica C: Superconductivity and its applications, vol. 469, pp. 1776-1780, 2009.

[66] T. Kiss, T. Nakamura, M. Inoue, M. Takeo, F. Irie and K. Yamafuji “Transport Characteristics in High Tc Superconductors”, Proceedings of 15th International Conference on Magnet Technology, no. 2, pp. 1052-1055, 1998.

[67] T. Kiss, S. Noda, S. Nishimura, K. Ohya, D. Utsunomiya, Y. A. Ilyn, et al., “Analysis of quench development in a cryocooler cooled Bi-2223 pancake coil based on the anisotropic transport E-J characteristics in a short tape sample,” Physica C: Superconductivity and its applications, vol. 357, pp. 1165-1168, Aug 2001.

[68] H. Okamoto, T. Kiss, S. Nishimura, M. Inoue, K. Imamura, M. Takeo, et al., “Prediction of E-J characteristics in Bi-2223/Ag tapes at low temperature and high magnetic field,” IEEE Transactions on Applied Superconductivity, vol. 13, pp. 3683-3686, Jun 2003.s

[69] T. Nakamura, S. Tsuchiya, A. Fujio, T. Hoshino, I. Muta, and M. Yamaguchi, “Angular dependence of E-J characteristics and dissipative properties in Bi-2223/Ag tape,” Superconductor Science & Technology, vol. 15, pp. 230-235, Feb 2002.

[70] N. Cheggour, J.W. Ekin, and C. L. H. Thieme, “Magnetic-field dependence of the reversible axial-strain effect in Y-Ba-Cu-O coated conductors,” IEEE Transactions on Applied Superconductivity, vol. 15, no. 2, pp. 3577-3560, 2005.

[71] D. Uglietti, B. Seeber, V. Abacherli, W. L. Carter, and R. Flukiger, “Critical currents versus applied strain for industrial Y-123 coated conductors at various temperatures and magnetic fields up to 19 T,” Superconductor Science and Technology, vol. 19, pp. 869-872, 2006.

[72] T. Nakamura, Y. Takamura, N. Amemiya, K. Nakao, T. Izumi, “ Longitudinal Inhomogeneity of DC Current Transport Properties in Gd-system HTS Tapes - Statistical Approach for System Design -,” J. Cryo. Super. Soc. Jpn., vol. 48, no. 178, 2013. (in Japanese)

[73] J. Pitel, P. Kovac, A. Kasztler, and H. Kirchmayr, “Optimization of winding geometry of Bi(2223)Ag coils with respect to external magnetic field,” IEEE Transactions on Applied Superconductivity, vol. 11, pp. 2324-2327, Mar 2001.

[74] T. Z. Dai, Y. J. Tang, J. D. Li, Y. S. Zhou, S. J. Cheng, and Y. Pan, “Study on ac losses of HTS coil carrying ac transport current,” Physica C: Superconductivity and its applications, vol. 426, pp. 1339-1342, Oct 2005.

[75] T. Koyama, I. Funaki, T. Nakamura, H. Kojima, and H. Yamakawa, “Thrust control system for magnetic sail spacecraft under variable solar wind environment,” 61st International Astronautical Congress, pp. 11061-11068, 2010.

[76] J. Ogawa, S. Fukui, T. Oka, T. Sato, H. Kojima, M. Shibayama, et al., “Influence of DC offset transport current on AC loss characteristics in HTS tapes,” IEEE Transactions on Applied Superconductivity, vol. 21, pp. 3325-3328, Jun 2011.

[77] J. Ogawa, S. Fukui, T. Oka, T. Sato, M. Shibayama, M. Egawa, et al., “Experimental investigation of loss characteristics with AC and DC offset transport current in HTS double pancake coil,” IEEE Transactions on Applied Superconductivity, vol. 22, p. 4, Jun 2012.

[78] J.-H. Kim and S. Pamidi, “Electrical characteristics of 2G HTS tapes under DC current with AC ripple,” IEEE Transactions on Applied Superconductivity, vol. 22, Jun 2012.

[79] T. Hemmi, N. Yanagi, K. Seo, G. Bansal, K. Takahata, and T. Mito, “Improvements of current decay behavior of HTS coils in persistent current operations,” IEEE Transactions on Applied Superconductivity, vol. 17, pp. 2422-2425, Jun 2007.

[80] S. Y. Hahn, J. Bascunan, W. S. Kim, E. S. Bobrov, H. Lee, and Y. Iwasa, “Field mapping, NMR lineshape, and screening currents induced field analyses for homogeneity improvement in LTS/HTS NMR magnets,” IEEE Transactions on Applied Superconductivity, vol. 18, pp. 856-859, Jun 2008.

[81] Y. Yanagisawa, H. Nakagome, D. Uglietti, T. Kiyoshi, R. Hu, T. Takematsu, et al., “Effect of YBCO-Coil Shape on the Screening Current-Induced Magnetic Field Intensity,” IEEE Transactions on Applied Superconductivity, vol. 20, pp. 744-747, Jun 2010.

[82] N. Amemiya and K. Akachi, “Magnetic field generated by shielding current in high T c superconducting coils for NMR magnets,” Superconductor Science and Technology, vol. 21, p. 095001, 2008.

[83] S. P. Ashworth, B. A. Glowacki, M. Ciszek, E. C. L. Chesneau, and P. Haldar, “Connectivity between filaments in BSCCO-2223 multi-filamentary tape,” IEEE Transactions on Applied Superconductivity, vol. 7, pp. 1662-1665, Jun 1997.

[84] M. Polak, M. Majoros, A. Kasztler, and H. Kirchmayr, “Filament bridging and critical current density variation in the cross-section of multifilamentary Bi-2223/Ag tapes,” IEEE Transactions on Applied Superconductivity, vol. 9, pp. 2151-2154, Jun 1999.

[85] A. V. Bobyl, D. V. Shantsev, T. H. Johansen, M. Basiljevich, Y. M. Galperin, and M. E. Gaevski, “Temperature dependence of filament-coupling in Bi-2223 tapes: magnets-optical study,” Superconductor Science & Technology, vol. 13, pp. 183-186, Feb 2000.

[86] Y. Bugoslavsky, G. K. Perkins, P. Buscemi, and A. D. Caplin, “Inhomogeneity of current distribution in multifilamentary BiSCCO-2223 tapes,” Superconductor Science & Technology, vol. 14, pp. 245-251, May 2001.

[87] J. Kvitkovic and M. Polak, “Remanent magnetisation in multifilamentary Bi-2223 tapes with filament bridging,” Physica C: Superconductivity and its applications, vol. 372, pp. 1012-1015, Aug 1 2002.

[88] E. Demencik, P. Usak, M. Polak, H. Piel, and M. Dhalle, “Lateral critical current distribution and self-field profile of Bi-2223/Ag conductors: measurements and calculations,” Superconductor Science and Technology, vol. 19, pp. 848-853, 2006.

[89] Y. Koyama, T. Takao, Y. Yanagisawa, H. Nakagome, M. Hamada, T. Kiyoshi, et al., “Towards beyond 1GHz NMR: Mechanism of the long-term drift of screening current-induced magnetic field in a Bi-2223 coil,” Physica C: Superconductivity and its applications, vol. 469, pp. 694-701, 7/1/ 2009.

[90] M. Inoue, T. Kiss, T. Kuga, M. Ishimaru, M. Takeo, T. Matsushita, et al., “Estimation of E–J characteristics in a YBCO coated conductor at low temperature and very high magnetic field,” Physica C: Superconductivity and its applications, vol. 392-396, pp. 1078-1082, 2003.

[91] T. Kiss, M. Inoue, T. Kuga, M. Ishimaru, S. Egashira, S. Irie, et al., “Critical current properties in HTS tapes,” Physica C: Superconductivity and its applications, vol. 392-396, pp. 1053-1062, 2003.

[92] K. Yamafuji, T. Fujiyoshi, and T. Kiss, “A theory of the thermal depinning transition in type-2 superconductors,” Physica C: Superconductivity and its applications, vol. 397, pp. 132-150, 10/15/ 2003.

[93] L. Y. Xiao, T. Kiyoshi, O. Ozaki, and H. Wada, “Case study on quench evolution and passive protection of high T-c superconducting pancake coil,” Cryogenics, vol. 39, pp. 293-298, Apr 1999.

[94] L. Pust, "Comparison between conventional flux creep in constant magnetic-field and the effect of creep on the shape of magnetic hysteresis loops in high-Tc superconductors," Superconductor Science & Technology, vol. 3, pp. 598-601, Dec 1990.

[95] A. Korpela, T. Kalliohaka, J. Lehtonen, R. Mikkonen, J. Pitel, and P. Kovac, "Relation between different critical current criteria and quench current in HTS magnets," Physica C: Superconductivity and its applications, vol. 372, pp. 1360-1363, 2002.

[96] A. Otsuka and T. Kiyoshi, "High-field magnet design under constant hoop stress," IEEE Transactions on Applied Superconductivity, vol. 18, no. 2, pp. 1529–1532, 2008.

[97] M. Sugano, T. Nakamura, K. Shikimachi, N. Hirano, and S. Nagaya, "Stress tolerance and fracture mechanism of solder joint of YBCO coated conductor," IEEE Transactions on Applied Superconductivity, vol. 17, no. 2, pp. 3067–3070, 2007.

[98] M. Sugano, Y. Yoshida, M. Hojo, K. Shikimachi, N Hirano, and S. Nagaya, "Two different mechanisms of fatigue damage due to cyclic stress loading at 77 K for MOCVD-YBCO-coated conductors," Superconductor Science & Technology, vol. 21, 054006, 2008.

[99] N. Cheggour, J. W. Ekin, C. L. H. Thieme, and Y.Y. XIe, "Effect of fatigue under transverse compressive stress on slit Y-Ba-Cu-O coated conductors," IEEE Transactions on Applied Superconductivity, vol. 17, no. 2, pp. 3063–3066, 2007.

[100] T. Nakashima, K. Yamazaki, S. Kobayashi, T. Kagiyama, M. Kikuchi, S. Takeda, et al., "Drastic Improvement in Mechanical Properties of DI-BSCCO Wire With Novel Lamination Material," IEEE Transactions on Applied Superconductivity, vol. 25, pp. 1-5, 2015.

[101] F. London and H. London, The Electromagnetic Equations of the Supraconductor, Proceedings of the Royal Society of London. Series A, Mathematical and Physical Sciences, vol. 149, no. 866, pp. 71-88, 1935.

[102] B. Cabrera, "The use of superconducting shields for generating ultra-low magnetic field regions and several related experiments," 7521850 Ph.D., Stanford University, Ann Arbor, 1975.

[103] J. W. Thomasson and D. M. Ginsberg, "Magnetic field shielding by a superconducting cylindrical tube of finite length," Review of Scientific Instruments, vol. 47, p. 387, 1976.

[104] S. Denis, L. Dusoulier, M. Dirickx, V. Ph, R. Cloots, M. Ausloos, et al., "Magnetic shielding properties of high-temperature superconducting tubes subjected to axial fields," Superconductor Science and Technology, vol. 20, p. 192, 2007.

[105] M. Masuzawa, K. Tsuchiya, and A. Terashima, "Study of Magnetic Shielding Materials and Fabrication of Magnetic Shield for Superconducting Cavities," IEEE Transactions on Applied Superconductivity, vol. 24, pp. 1-4, 2014.

[106] G. V. Gettliffe, "High-Temperature Superconductors as Electromagnetic Deployment and Support Structures in Spacecraft," Mater thesis, Massachusetts Institute of Technology, 2013.

Publication List

Major Publications

1. (Selected as Highlights of 2014) Y. Nagasaki, T. Nakamura, I. Funaki, Y. Ashida, and H. Yamakawa, "Experimental and Numerical Investigation on Screening Currents Induced in Bi-2223/Ag Double-pancake Coil for Space Applications," Superconductor Science and Technology, vol. 27, p. 115005, 2014.

2. Y. Nagasaki, T. Nakamura, I. Funaki, Y. Ashida, and H. Yamakawa, "Numerical Investigation on Thermal Stability of Conduction-cooled Bi-2223/Ag Coil Under AC Ripple Current for Space Applications," IEEE Transactions on Applied Superconductivity, vol. 24, no. 3, p. 4700305, 2014.

3. Y. Nagasaki, T. Nakamura, I. Funaki, Y. Ashida, and H. Yamakawa, "Conceptual Design of YBCO Coil With Large Magnetic Moment for Magnetic Sail Spacecraft," IEEE Transactions on Applied Superconductivity, vol. 23, no. 3, p. 4603405, 2013.

4. Y. Nagasaki, T. Nakamura, I. Funaki, Y. Ashida, and H. Yamakawa, "Coupled-analysis of Current Transport Performance and Thermal Behavior of Conduction-cooled Bi-2223/Ag Double-pancake Coil for Magnetic Sail Spacecraft," Physica C, vol. 492, pp. 96-102, 2013.

5. Y. Nagasaki, T. Nakamura, I. Funaki, Y. Ashida, and H. Yamakawa, "Thermal Conduction Characteristics of Bi- and Y-system Tape Conductors Aiming at Conduction-cooled Magnet," J. Cryo. Super. Soc. Jpn., vol. 47, pp. 597-604 (in Japanese), 2012.

Presentations in International Meeting (Invited Talk)

1. Y. Nagasaki, T. Nakamura, I. Funaki, Y. Ashida, H. Kojima and H. Yamakawa, "Cooling Characteristics of Conduction-cooled HTS Coil Aiming at Magnetic Sail for Space

Mission," International Cryogenic Engineering Conference 24-International Cryogenic Materials Conference 2012, 17B-OR4-01, Fukuoka, Japan, May, 2012.

Presentations in International Meeting

1. Y. Nagasaki, I. Funaki, T. Nakamura, and H. Yamakawa, "Increase in Thrust of Magneto Plasma Sail using Solid or Deployable Superconducting Coil," The 30th International Symposium on Space Technology and Science, the 34th International Electric Propulsion Conference & the 6th Nano-Satellite Symposium, 2015-b/IEPC-328, Kobe, Japan, July, 2015.

2. Y. Nagasaki, T. Nakamura, I. Funaki, Y. Ashida and H. Yamakawa, "Experimental and Numerical Investigation of Screening Currents Induced in Conduction-cooled Bi-2223/Ag Coil for Space Applications," Electronic Materials and Applications 2015, A2-2118801, Florida, USA, Jan., 2015.

3. Y. Nagasaki, T. Nakamura, I. Funaki, Y. Ashida and H. Yamakawa, "Optimal Design of Conduction-cooled Superconducting Magnet for Magneto Plasma Sail," 65th International Astronautical Congress, C.4.8, Toronto, Canada, Sep., 2014.

4. Y. Nagasaki, T. Nakamura, I. Funaki, Y. Ashida and H. Yamakawa, "Experimental and Numerical Investigation on Thermal Stability of Conduction-cooled Superconducting Magnet for Space Applications," International Conference on Magnet Technology 23, 3PoAK-05, MA., USA, July, 2013.

5. Y. Nagasaki, T. Nakamura, I. Funaki, H. Kojima and H. Yamakawa, "Conceptual Design of Conduction-cooled Superconducting Magnets for Space Application," Applied Superconductivity Conference 2012, 1LA-07, Oregon, USA, Oct., 2012.

6. Y. Nagasaki, T. Nakamura, I. Funaki, T. Koyama, H. Kojima and H. Yamakawa, "Numerical Investigation on Conduction-cooled Superconducting Magnets in Space," 63rd International Astronautical Congress, C.2.4.20, Naples, Italy, Oct., 2012.

7. Y. Nagasaki, T. Nakamura, T. Koyama, I. Funaki, Y. Ashida, H. Kojima and H. Yamakawa, "Characteristic Comparison Between Bi-2223/Ag and YBCO System Superconducting Magnets for Magnetic Sail Spacecraft," Asian Conference on Applied Superconductivity and Cryogenics 2011, P-122, New Delhi, India, Nov., 2011.

Awards

1. Highlights of 2014 (Best paper), Superconductor Science and Technology, Feb. 2015.
2. Mazume Research Award for Young Scientists, Jun. 2013.
3. Student Award, 56th Space Technology and Science Conference, Nov. 2012.
4. Grant from Society for Promotion of Space Science for Applied Superconductivity Conference 2012, Oct. 2012.

Appendix A

Superconducting Shileding

This study designed a scale-down model superconducting tube to attenuate a magnetic field of the magneto plasma sail to protect crews and instrument in the spacecraft by using Meissner effect of the superconductor. The design parameters are superconducting materials, thickness, d, diameter, Φ, length, l, and layer numbers of tubes. We designed a scale-down model superconducting tube for preliminary experiments. We firstly evaluated the effect of the field penetration on the shielding factor of the tube. We also considered the field penetration from both ends of the tube, and identified superconducting materials to attenuate magnetic fields most effectively (including AC fields).

A.1 Theoretical Analysis

The first important aspect of the magnetic shielding is the amount of EM fields penetration into superconductors. The magnetic field is greatly attenuated in the superconductor but also slightly penetrates into the superconductors. The next aspect is the amount of EM fields penetration into the tube from both ends. We evaluated the effect of open areas on the shielding factors.

A.1.1 EM field penetration into superconductors

While the external magnetic field is below the critical magnetic field, the field still penetrates into the superconductor with a depth of London length, λ. The effect of the field penetration on the attenuation ratio of superconducting tubes can be theoretically calculated with assuming an infinite length of a superconductor, which is an ideal condition for the magnetic shielding without the effect of the penetration from both ends. When the axial magnetic field, B_{ax}, is applied to the infinite superconductor, the electromagnetic phenomena in the superconductor can be expressed by solving the London equations [101] (eqs. A.1.1and A.1.2) and Ampere's law (eq. A.1.3) as described below:

$$E = \mu_0 \lambda^2 \frac{\partial J}{\partial t} \tag{A.1.1}$$

$$\nabla \times J = \frac{B}{\mu_{0\lambda^2}} \tag{A.1.2}$$

$$\nabla \times B = \mu_0 J \tag{A.1.3}$$

where E is the electric field, μ_0 is the magnetic permeability, λ is the London penetration depth, J is the current density. By solving the London equations with a boundary condition, the magnetic field inside of the tube, B_{in}, can be calculated when external magnetic field, B_{ax}, is applied for each superconducting material. In this calculation, the attenuation ratio was defined as $\Delta B_{\mathrm{in}}/\Delta B_{\mathrm{ex}}$. By solving the London equations and Ampere's law with a boundary condition of superconductors, the attenuation ratio $\Delta B_{\mathrm{in}}/\Delta B_{\mathrm{ex}}$ of the magnetic field can be described as a function of the thickness of the superconductors, d, and outer diameter of the tube,φ_{out} as shown in Fig. A.1. In this calculation, we assumed the EM field was continuous and had the same value at the edge of the superconductor and superconducting tubes with the outer diameter of 50 mm. Each line shows the attenuation ratio for each superconductor. As can be seen in Fig. A.1, the magnetic field can be effectively attenuated with the increasing thickness of the superconductors. As also shown in the figure, the attenuation ratio depends on the superconducting materials, and Low Temperature Superconducting (LTS) tubes such as Pb and Nb attenuate the magnetic field most effectively. Nevertheless, most of the superconductors can greatly attenuate the magnetic field with a sufficient thickness.

A.1.2 EM field penetration from both ends of the tube

In practical applications, a superconducting tube has a finite length, and has open ends. The effect of the field penetration from the ends of the tube on the attenuation ratio must be evaluated. The penetration from the ends of the superconducting tube can be simply obtained from the following equations [102, 103].

$$\frac{B_{\mathrm{in}}}{B_{\mathrm{ex}}} = -\exp(-\frac{Cz}{\phi_{\mathrm{in}}}) \tag{A.1.4}$$

$$\frac{B_{\mathrm{in}}}{B_{\mathrm{ex}}} = 1.13 \times 10^{-5l/3\phi_{\mathrm{in}}} \tag{A.1.5}$$

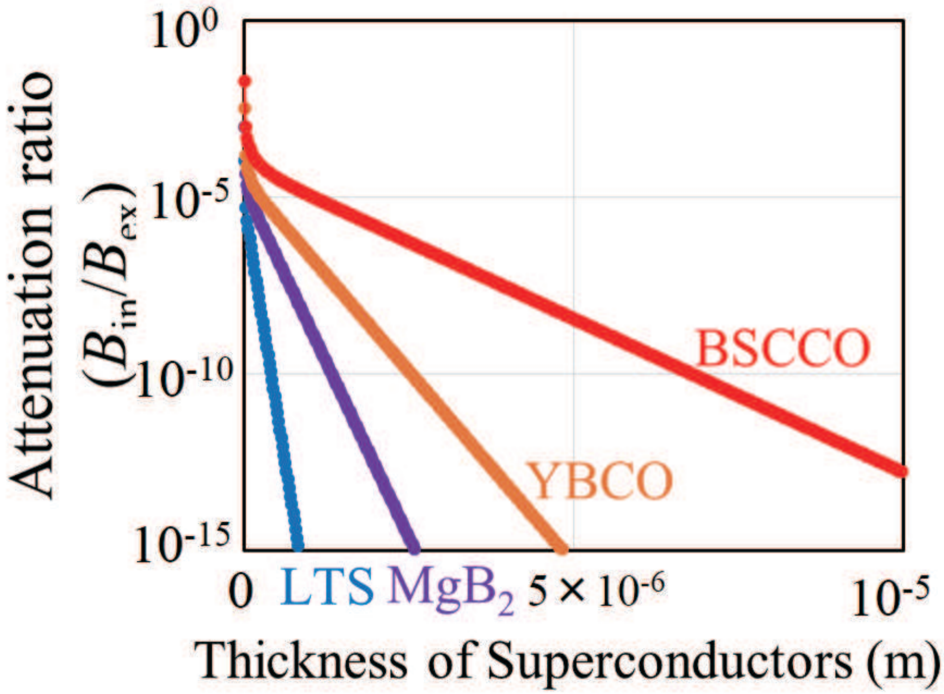

Figure A.1: Attenuation ratios as a function of the thickness of the superconducting materials (outer diameter = 50 mm).

C is decay coefficient from the open end. The attenuation ratio of the tube was defined as the ratio of B_{in} to B_{ex}, at the center of the tube. Numerical simulation results were compared with these theoretical analyses in order to verify the validity of the calculation.

A.2 Numerical Analysis Results

In order to consider a more realistic condition and simulate the shielding factor of high temperature superconducting tubes, whose superconducting characteristics are more complicated to analyze, We analyzed the induced shielding currents, I_{s}, were analyzed using the Faraday's law, Biot-Savart law, percolation depinning model, flux creep model, and inductance of shielding currents.

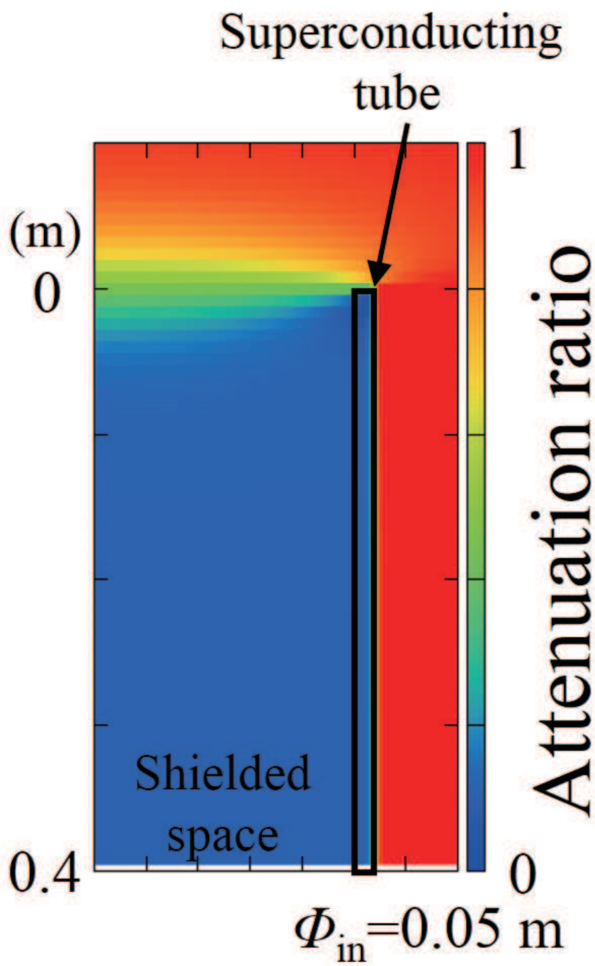

Figure A.2: An example of simulating the field attenuation inside of the tube (thickness = 2 mm).

We simulated the field penetration from open ends of superconducting tubes with a finite length. Figure A.2 shows an example of the simulation result (Nb superconducting tube: length l = 800 mm, inner diameter Φ_{in} = 50 mm, thickness d = 2 mm), and the color map indicates the attenuation ratio of the magnetic field. Because of the symmetry of the electromagnetic field, only a part of the cross section of a superconducting tube is depicted. We only consider the axial magnetic field in this study. As can be seen in this figure, the magnetic field is greatly attenuated in the superconducting tube (shielded space). The field penetration from the open end can also be seen in the figure (0 m point at y-axis). The simulation result also indicates that the magnetic field decays exponentially from the open end of the tube.

Figure A.3 shows the field attenuation ratio as a function of the distance from the open end. The theoretical results with two kinds of the different models (eqs. A.1.4and A.1.5) are also shown in this figure. The radial and axial in the graph legends mean the direction of the applied magnetic field. As can be seen in Fig. A.3, the simulation result agrees well with a theoretical analysis (Cabrera model) in the range of 0 to 0.16 m. The difference in the distance of over 0.16 m is caused because the theoretical analysis simplifies the superconducting property and assumes the infinite length of superconductors. The saturation of the attenuation ratio along with the distance from the open end was also obtained in previous studies [104, 105]. Considering the simulation result, it can be said that the length of the superconducting tube should be over 0.32 m in order to obtain a higher attenuation ratio in this case, although a tube with much longer length than 0.32 m has almost the same performance.

The attenuation ratio of radial magnetic fields is more difficult to be simulated because more complicated shielding current will flow in the superconducting tube. To simulate the shielding currents induced by radial fields, and compare the results with the theoretical analyses is one of our future study.

By using the developed method, we also calculated the attenuation ratio of AC magnetic fields in the case of both LTS (Nb) and HTS (BSCCO) tubes (length: 400 mm, diameter: 50 mm, thickness:2 mm). Figure A.4 shows the attenuation ratio as a function of the frequency of the AC magnetic fields. As shown in Fig. A.4, the attenuation ratio of the HTS tube depends on the frequency of the field, while the LTS tube does not. This is because the shielding currents in the HTS tube are induced following the nonlinear current transport characteristics of the HTS. From this result, LTS is superior to HTS to attenuate magnetic fields with a variety of frequencies. However, in terms of the cooling cost, HTS has an advantage because it can be used in liquid nitrogen instead of liquid helium. We will consider if the attenuation ratio of HTS tubes can be improved by increasing the layer number of HTS

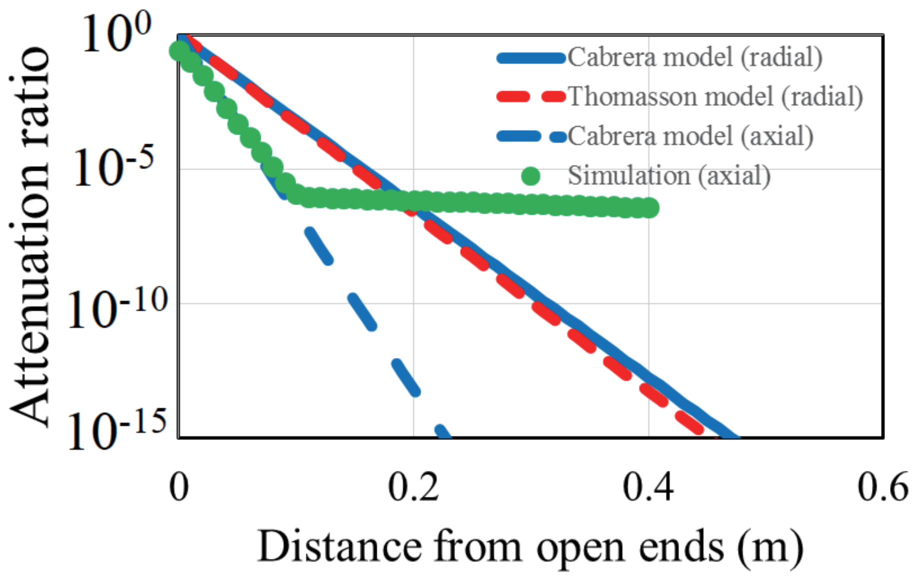

Figure A.3: Attenuation ratio as a function of the distance from the open ends of the tube (length = 800 mm, inner diameter = 50 mm, thickness = 2 mm).

tubes or incorporate with a ferromagnetic tube.

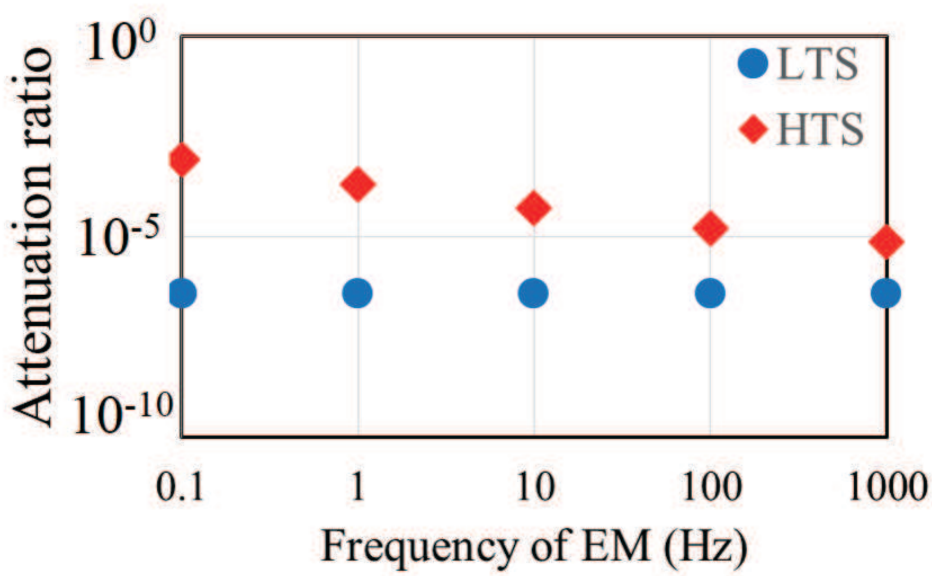

Figure A.4: Attenuation ratio of the tube as a function of the frequency of ambient AC magnetic field (length = 400 mm, inner diameter = 50 mm, thickness = 2 mm).

Appendix B

Deployable HTS coil for Magneto Plasma Sail

We investigated the feasibility of a deployable coil to drastically increase the magnetic moment of the coil. A coil with a diameter of more than 4 m folded in the radial or axial direction (as shown in Fig. B.1) and stored in the rocket is deployed in space after the launch to increase the area enclosed by the coil and magnetic moment. We firstly optimized circular HTS coils with a diameter of from 2 m to 110 m in order to investigate the dependence of the magnetic moment on the coil diameter. Figure B.2 shows the relationship between the coil diameter and magnetic moment to mass ratio of the coil obtained from the optimization of the YBCO coil. As shown in the figure, the magnetic moment to mass ratio drastically increases with the coil diameter. This is because with the increasing coil diameter, the coil surface area, that is cooling surface area, increases and, as a result, thermal stability improves. Due to the increasing coil area and thermal stability, the magnetic moment can be greatly improved with the increasing coil diameter. Figure B.2 also indicates that the deployable coil with a diameter of 20 m can achieve the magnetic moment which is ten times larger than that of the previous study.

As a method for the coil deployment, using an extensible beam or some support structure might be applied. However, to obtain an enough thrust from the magneto plasma sail for space missions, large scale structure such as a diameter of more than 20 m is required. Figure B.3 shows that the relationship between the coil diameter and the total weight of the deployment system using an extensible beam. We assumed the extensible beam made of Aluminum (Density: 2.7 g/cm3). As shown in Fig. B.3, a deployable coil with a diameter of 20 m needs a deployment structure weighing up to 200 kg. As can also be seen in Fig. B.3, as the coil diameter increases, the weight of the required system greatly increases to more than 1000 kg since the coil with a larger diameter needs a larger number of the extensible

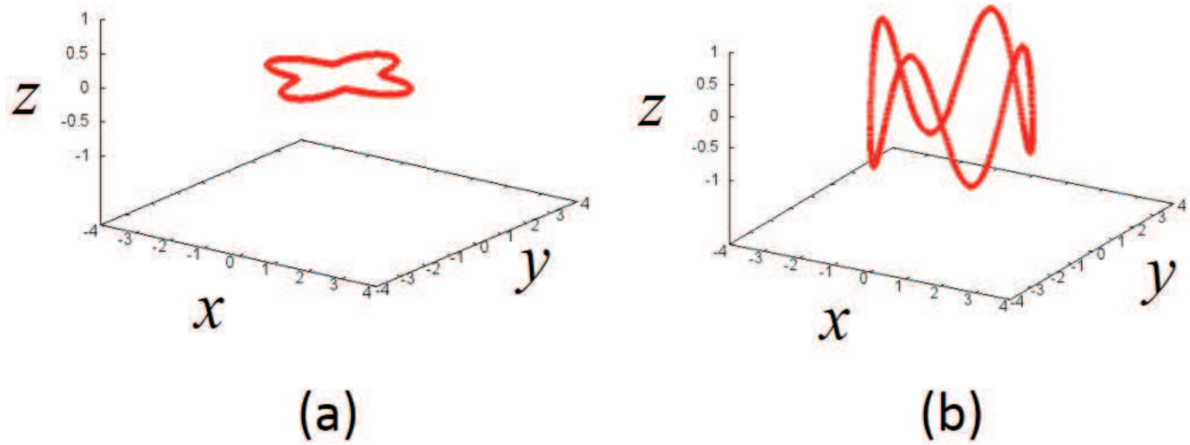

Figure B.1: Coil (a) folded in the radial direction, and (b) folded in the axial direction.

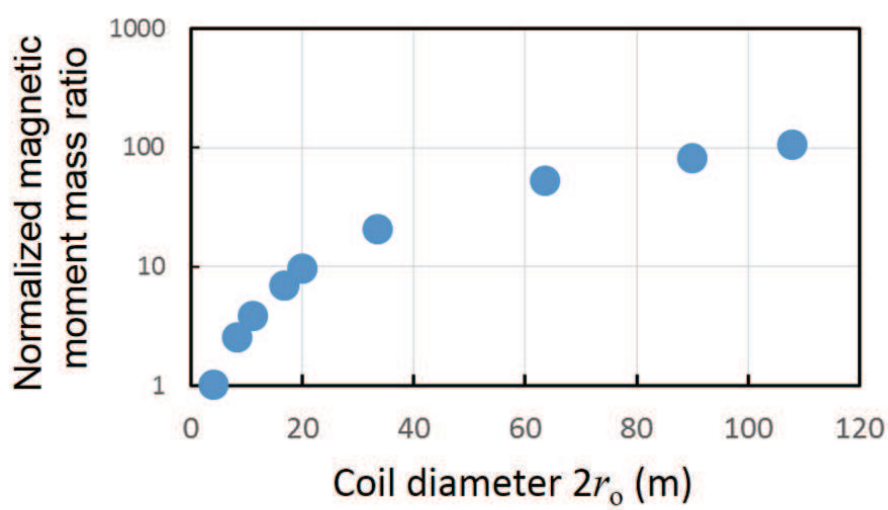

Figure B.2: Normalized magnetic moment to mass ratio of circular coils with a variety of coil diameter. The total length of the YBCO CCs is constant.

beams.

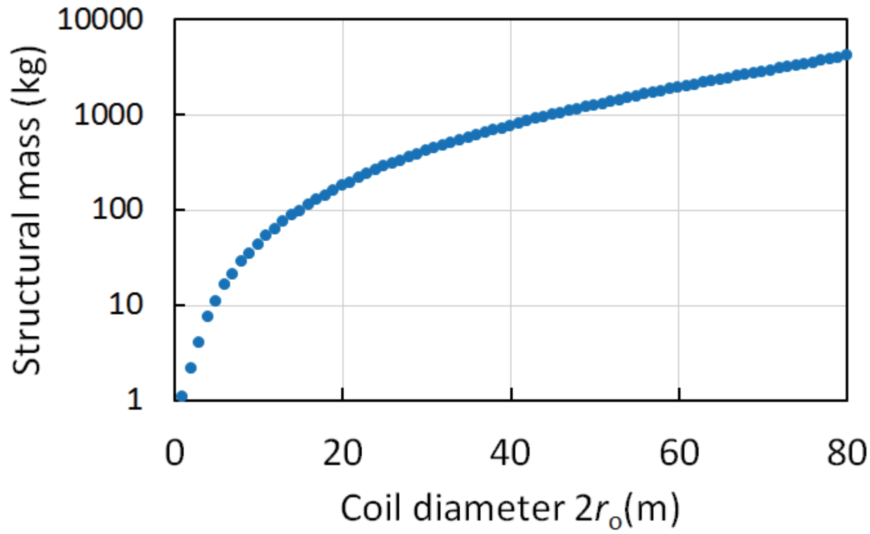

Figure B.3: Total weight of the deployment structure for a variety of coil diameter after the deployment.

In this study, we investigated one possible method for a coil deployment in space using an electromagnetic force to reduce the weight of the system and increase the magnetic moment to mass ratio. During the coil excitation, an electromagnetic force between the coil current and coil magnetic field, which is so-called hoop stress, acts on the coil in radial direction. Figure B.4 describes the distribution of the electromagnetic force acting on a coil folded in the axial direction during the excitation. As can be seen in Fig. B.4, the electromagnetic force acts to the outer direction to which the coil expands. The coil deployment using the electromagnetic force has been also proposed for a deployment of a space telescope [106]. The coil is folded and stored during launch and can be deployed in space without any deployment structure by using such electromagnetic force. We simulated the coil deployment using the electromagnetic force by solving the equation of motion described below:

$$\rho \frac{\partial^2 \boldsymbol{r}}{\partial t^2} = \frac{\partial}{\partial s}\left(\sigma \frac{\partial \boldsymbol{r}}{\partial s}\right) + \boldsymbol{F} \tag{B.0.1}$$

$$\frac{\partial \boldsymbol{r}}{\partial s} \cdot \frac{\partial \boldsymbol{r}}{\partial s} = 1 \tag{B.0.2}$$

(3) where $\boldsymbol{r}$ denotes the position vector for each coil element s, $\boldsymbol{F}$ electromagnetic force, t time, ρ line density, σ local tensile force, respectively. For the simplicity, the motion of one

turn coil was analyzed in a free space. Figure B.5 describes the time transient of the coil deployment as a simulation result. The inner line shows the initial coil shape, and outer line shows the shape after the deployment. As shown in the figure, we confirmed that the folded coil were successfully deployed with the electromagnetic force.

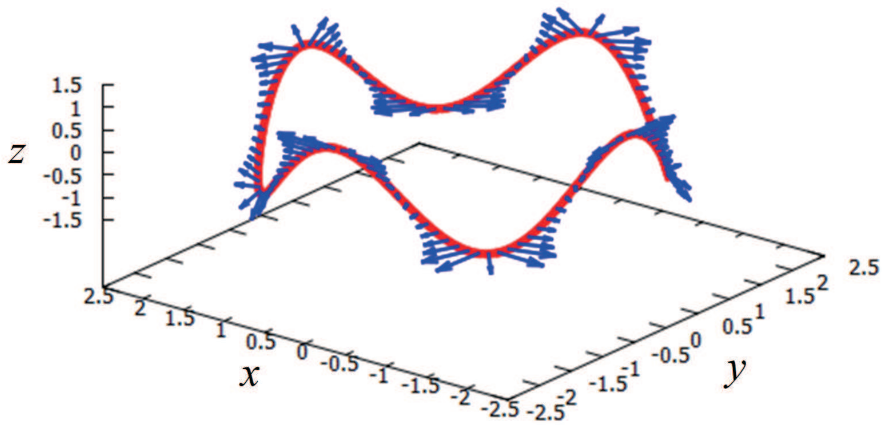

Figure B.4: Electromagnetic force distribution. (red line: a folded coil, blue arrows: electromagnetic force vectors)

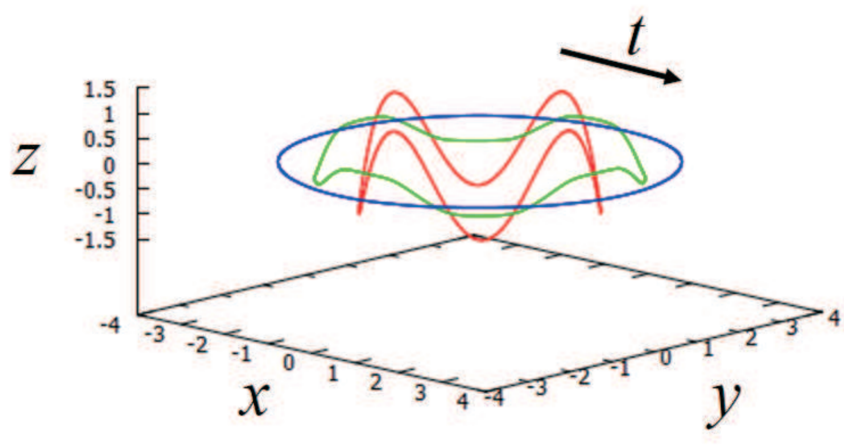

Figure B.5: Simulation result of a coil deployment with an electromagnetic force. (red line: initial position, blue line: after deployment)